Ticking near the Zero-Point Energy: towards 1×10^{-18} Accuracy in Al^+ Optical Clocks

by

Jwo-Sy Chen

M.S., Physics, National Tsing Hua University, Taiwan, 2007.

B.S., Physics, National Tsing Hua University, Taiwan, 2005.

A thesis submitted to the

Faculty of the Graduate School of the

University of Colorado in partial fulfillment

of the requirements for the degree of

Doctor of Philosophy

Department of Physics

2017

This thesis entitled:
Ticking near the Zero-Point Energy:
towards 1×10^{-18} Accuracy in Al^{+} Optical Clocks
written by Jwo-Sy Chen
has been approved for the Department of Physics

_____

Dr. David Leibrandt

_____

Dr. David Wineland

Date _____

The final copy of this thesis has been examined by the signatories, and we find that both the content and the form meet acceptable presentation standards of scholarly work in the above mentioned discipline.

Chen, Jwo-Sy (Ph.D., Physics)

Ticking near the Zero-Point Energy:

towards 1×10^{-18} Accuracy in Al^+ Optical Clocks

Thesis directed by Dr. David Leibrandt and Dr. David Wineland.

The advancement of optical atomic clocks in the past two decades has motivated many potential applications in navigation, communication, and science. Accurate optical clocks that outperform the current cesium time standard also trigger a discussion about a possible redefinition of the SI second. The $^{27}Al^+$ quantum logic clocks developed at the National Institute of Standards and Technology (NIST) were the first to achieve the clock fractional frequency uncertainty below 10^{-17} in 2010. To date, a few research groups around the world have demonstrated optical clocks based on various atomic transitions with fractional frequency uncertainty in the 10^{-18} range. The accuracy of the previous $^{27}Al^+$ clocks was limited by the second order Doppler (time dilation) shift and the blackbody shift. Since 2010, the third $^{27}Al^+$ optical clock is being developed at NIST to achieve a higher accuracy. The frequency uncertainties dominant in the previous clocks are controlled and reduced in the current optical clock. The new design of the ion trap system has reduced significantly both the blackbody radiation shift uncertainty and the time dilation shift uncertainty due to micromotion, while the time dilation shift uncertainty due to the secular motion has been reduced by more than an order of magnitude by operating the optical clock near the three dimensional zero-point energy. Despite those previously dominant uncertainties, several other systematic effects are being evaluated and some other efforts are being made to achieve a total uncertainty towards 1.0×10^{-18}. In this thesis, I will document the detail of the construction and evaluation of the current $^{27}Al^+$ optical clock developed at NIST.

Dedication

My family, old and new.

Acknowledgements

All the work described in this thesis can only become possible with supports from many people in the Ion Storage group of the NIST. At first, I would like to thank my advisers, Till Rosenband, David Leibrandt, and David Wineland, who all provided the great scientific research environment and the guidance of the experiment. Their technical expertise and scientific knowledge show me how to work on a challenging project from the scratch towards the success. I am great indebted to Sam Brewer, whom I worked with in the past five years and learned a great deal about science from. We constructed two ion traps together and tackled down so many scientific and technical difficulties to make the "clock tick! I am sure our new system will become again the most accurate clock in a very near future! I also want to express my appreciation to Jim Bergquist, James Chou, Aaron Hankin, and David Hume, Christoph Kurz and all former/current members within the clock team of Ion Storage group for sharing all your wonderful knowledge and experience with me. Many people in the Ion Storage group also contributed to various stages of the experiment. I would like to thank all the people in the group collectively for the experimental support as well as the cheerful working environment that we created together over the years. I may probably forget mentioning some people here but all you play important roles in my time in the graduate school. The graduate study has been a long journey to me, both geologically and mentally. I would like to thank my family and old friends, C.C.C. and S.C.L., who stand behind me over years and support me through the tough ups and downs across the ocean. Thanks!

Contents

Chapter

1 Introduction **1**

1.1 Optical Frequency Standards 3

1.2 Optical Clock Applications 6

1.3 $^{27}Al^{+}$ Optical Clocks 7

1.4 Thesis Organization 9

2 Experimental Setup **10**

2.1 The Trap 11

2.2 Trap System 18

2.2.1 Vacuum Chamber 18

2.2.2 Imaging and Photon Collection System 21

2.2.3 RF Resonator and RF Power Control 24

2.2.4 Magnetic Field Control 25

2.3 Ion Loading 25

2.4 $^{27}Al^{+}$ Laser System 28

2.4.1 Energy Levels and Lasers 30

2.4.2 Frequency Stabilization of the $^{3}P_{1}$ Laser 31

2.4.3 Frequency Stabilization of the $^{3}P_{0}$ Laser 32

2.5 $^{25}Mg^{+}$ Laser System 34

2.5.1 Qubit . . . 34
2.5.2 Atomic State Preparation and Doppler Laser Cooling . . . 37
2.5.3 Repumping . . . 38
2.5.4 Motion-Sensitive Raman Spectroscopy . . . 39
2.6 Other Techniques . . . 40
2.6.1 Maximum-Likelihood Probability Estimation . . . 40
2.6.2 UV Fibers and Pulse Area Control . . . 42
2.6.3 AOM Double-pass Configuration . . . 43
2.7 Quantum Logic Spectroscopy . . . 45
2.8 Clock Operation Pulse Sequence . . . 47
2.8.1 State Preparation . . . 47
2.8.2 Clock Interrogation . . . 48
2.8.3 Atomic State Detection . . . 49

3 Time Dilation Effect due to Secular Motion 50

3.1 Motion in RF Traps . . . 50
3.2 Sideband Thermometry . . . 52
3.3 Sympathetic Doppler Cooling and Energy Estimation . . . 54
3.4 Sympathetic Sideband Cooling and Energy Estimation . . . 57
3.4.1 Numerical Model . . . 59
3.4.2 Heating Mechanisms . . . 60
3.4.3 Summary . . . 67
3.5 Cooling Pulse Optimization . . . 70
3.5.1 Cooling Pulse Sequence at Drive Frequency $\Omega_T \simeq 2\pi \times 76$ MHz . . . 71
3.5.2 General Sideband Cooling Pulse Sequence . . . 74
3.6 Clock Frequency Shifts and Uncertainties due to Secular Motion . . . 78
3.6.1 Determination of the Energy after Sideband Cooling . . . 78

3.6.2 Time-dilation Shift due to Secular Motion 80

4 Other Systematic Effects and Concerns **86**

4.1 Linear Doppler Shift 86

4.2 Excess Micromotion Shift 87

4.2.1 Introduction 87

4.2.2 Characterization and Compensation 88

4.2.3 Residual EMM due to Phase Imbalances 90

4.2.4 Evaluation of the Time Dilation Shift due to EMM 91

4.3 Blackbody Radiation Shift 94

4.3.1 Polarizability of the Clock Transition 96

4.3.2 BBR Environment 96

4.3.3 Estimate of Clock Shift due to BBR 97

4.4 Zeeman Shift 99

4.5 Background Gas Collisions 100

4.6 Stark Shift due to the RF Drive Field 102

4.7 Formation of AlH^+ 103

5 Conclusion **105**

Bibliography **108**

Tables

Table

1.1 Secondary representations of the second in the optical frequency domain 3

1.2 Error budgets of the previous $^{27}Al^{+}$ optical clocks 8

2.1 Iterations of wheel traps 17

2.2 Comparison of clock operation protocols 47

3.1 Energy determination of sympathetic Doppler cooling 55

3.2 Parameters of secular modes of motion at 76 MHz drive frequency 71

3.3 Parameters of secular modes of motion at 40 MHz drive frequency 76

3.4 Number of sideband cooling pulses of each sideband order for the drive frequency $\Omega_T \simeq 2\pi \times 40$ MHz 78

3.5 Summary of heating sources at 40 MHz drive frequency 83

3.6 Summary of heating sources at 76 MHz drive frequency 83

4.1 The field strength that causes EMM and the resulting time dilation shift measured by the $^3P_1$ transitions 95

5.1 Clock uncertainty budget 107

Figures

Figure

1.1 Frequency standards recommended by the BIPM 4

1.2 Clock history 5

2.1 Typical linear Paul trap schematic 13

2.2 Ion traps used in previous Al^+ optical clock experiments. 14

2.3 Wheel trap schematic 15

2.4 Wheel trap pictures 16

2.5 Dipole and quadrupole field generated by two rf resonators 17

2.6 Vacuum chamber drawing 19

2.7 Trap mounting scheme 20

2.8 Laser beam geometry 22

2.9 Illustration of the imaging system 23

2.10 The schematic of meander line resonators 24

2.11 Ablation target 26

2.12 Energy level diagrams of Mg and Al 27

2.13 Ion loading flowchart 29

2.14 Energy level diagram of $^{27}Al^+$. 31

2.15 $^{27}Al^+$ laser beamlines 32

2.16 $^{27}Al^+$ $^3P_1$ laser frequency stabilization scheme 33

2.17 $^{27}Al^{+}$ $^{3}P_0$ laser frequency stabilization scheme 35
2.18 Relevant energy level diagram of $^{25}Mg^{+}$ 36
2.19 $^{25}Mg^{+}$ laser beam setup 37
2.20 Raman transition spectrum of a two-ion pair 39
2.21 Photon-count histogram of $|\uparrow (\downarrow)\rangle$ 41
2.22 Effect of UV fibers 42
2.23 Double-pass AOM Configuration 44
2.24 Quantum logic spectroscopy pulse sequence 46
2.25 State preparation pulse sequence 48
2.26 Clock interrogation pulse 49

3.1 Secular modes of motion of $^{25}Mg^{+}$-$^{27}Al^{+}$ ion pair. 51
3.2 The relation between the $\bar{n}$ and the first-order BSB-to-RSB ratio β. 53
3.3 The sympathetic Doppler cooling limit versus the mass ratio of two-ion pair. 54
3.4 Thermal distribution fit to a single $^{25}Mg^{+}$ 57
3.5 Repump heating rates 62
3.6 Illustration of a heating mechanism involving a coherent process 63
3.7 Simulation of the motional excitation due to an off-resonant carrier transition followed by a first-order RSB cooling pulse 65
3.8 Simulation of the motional excitation due to spontaneous emission from the Raman intermediate states followed by a first-order RSB cooling pulse 66
3.9 Sideband cooling pulse-by-pulse comparison 69
3.10 Motional sideband Rabi rate 70
3.11 Energy evolution of secular modes during sideband cooling at $\Omega_T \simeq 2\pi \times 76$ MHz . . 73
3.12 Motional sideband Rabi rate 75
3.13 Energy evolution of secular modes during sideband cooling at $\Omega_T \simeq 2\pi \times 40$ MHz . . 77

3.14 Fock state distribution of the z-COM mode after sideband cooling at $\Omega_T \simeq 2\pi \times 76$ MHz 80

3.15 RSB Rabi oscillation of the residual motional excitation after sideband cooling at $\Omega_T \simeq 2\pi \times 40$ MHz 81

3.16 RSB Rabi oscillation of the residual motional excitation after sideband cooling at $\Omega_T \simeq 2\pi \times 76$ MHz 82

3.17 Secular motion time-dilation shift 85

4.1 Electrodes fabricated on the trap wafer. 89

4.2 Time dilation shift due to EMM and secular motion as a function of the drive frequency Ω_T 92

4.3 Time dilation shift due to the a-EMM 93

4.4 Trap temperature increase versus rf drive power at $\Omega_T \simeq 2\pi \times 76\,\mathrm{MHz}$ 97

4.5 The fractional clock frequency shift due to BBR versus the radiation temperature . . 98

4.6 Contribution of BBR shift uncertainty at T= 300 K 98

4.7 Magnetic field variance about the mean versus the trap drive rf power 101

4.8 Ion pair reordering rate after loading 102

4.9 Optical clock up time 104

Chapter 1

Introduction

The development of quantum mechanics since the late nineteenth century significantly changes our view of nature and affects our daily life. One of the essential influences is the redefinition of the International System of Units (SI) proposed by the International Bureau of Weights and Measures (BIPM) [Taylor 08]. Except for the unit of mass, SI units are now defined by fundamental properties of atoms, molecules, or photons [1] . In 1967, the unit of time, the second, was defined in terms of an atomic transition frequency to replace the previous standard, which was based upon astronomical observations, as follows [Taylor 08]:

> The second is the duration of 9 192 631 770 periods of the radiation corresponding to the transition between the two hyperfine levels of the ground state of the cesium 133 atom[2] .

Since then, microwave cesium atomic clocks have been built around the world and have formed the basis of international atomic time (TAI) for half a century to date. The invention and application of TAI play an important role in global navigation satellite systems (GNSS), an example of which is the global positioning system (GPS) that many people use daily [Major 07].

Current atomic clocks all operate in essentially the same manner. They consist of a continuous electromagnetic radiation source which is frequency locked to an atomic transition frequency. The performances of atomic clocks are characterized by two quantities, accuracy and stability.

[1] The unit of mass in SI is defined by the international prototype of the kilogram, an artificial object made of platinum-iridium stored at the BIPM, but research is ongoing to establish a quantum-based mass reference as well [de Mirandés 16, Richard 16]

[2] This definition was later refined in 1997 to refer to the transition frequency at a temperature of 0 K.

While the former indicates the deviation from the unperturbed frequency of the atomic transition, i.e., systematic shifts of frequency measurements, the later represents the amount of noise of the measurements. The accuracy of atomic clocks depends on knowledge of the atomic transition properties, and the ability to control both the atoms' environment and atoms' motion. Therefore, each type of atomic clock has its own difficulties in terms of the accuracy. On the other hand, the stability has a more general fundamental limit that applies to all atomic clock systems. A widely used measure of the stability is the Allan variance, σ_y^2, which is given by [Allan 66, Riley 08]

$$\sigma_y^2(\tau) = \frac{1}{2(M-1)} \sum_{i=1}^{M-1} \left(\langle y(\tau) \rangle_{i+1} - \langle y(\tau) \rangle_i \right)^2 , \tag{1.1}$$

where $\langle y(\tau) \rangle_i$ denotes the i^{th} fractional frequency measurement averaged over an interrogation duration τ, and M is the number of measurements. The quantity $\sigma_y(\tau)$ is called the Allan deviation, which is used frequently to characterize the stability[3] of the clocks in the frequency metrology community. For an ideal atomic system without any systematic effects, the noise of frequency measurements is dominated by the statistical uncertainties, and hence $\sigma_y(\tau)$ decreases when τ increases. However if there is any systematic frequency shift existing in an atomic transition which can change in time, the Allan deviation $\sigma_y(\tau)$ will level off or even increase with large τ.

The frequency determination of atomic clocks is conducted in such a way that the total interrogation duration τ consists of many repeated measurements of duration T_{int}. For an ideal system, the fundamental limit to the measurement noise results from the nature of measurements in quantum mechanics, and is called quantum projection noise [Itano 93]. In such cases, the Allan deviation can be written in a simple form if an atomic transition is probed using Ramsey spectroscopy [Ramsey 85, Itano 93]:

$$\sigma_y(\tau) = \frac{1}{2\pi f_0 \sqrt{N T_{int} \tau}}, \tag{1.2}$$

where f_0 is the atomic transition frequency, and N is the number of atoms. From this expression, it is obvious that atomic clocks benefit from a larger transition frequency f_0. Therefore, if we

[3] In fact, it denotes the instability of the clocks. The smaller the Allan deviation $\sigma_y(\tau)$, the better the stability of the clock.

Table 1.1: Secondary representations of the second in the optical frequency domain recommanded by the BIPM as of 11 May, 2016 [Taylor 08]. The values are the weighted mean of measurements from various laboratories.

Atomic species	Transition	Wavelength [nm]	Frequency [Hz]
$^{27}Al^+$	$3s^2\,{}^1S_0$ - $3s3p\,{}^3P_0$	267	1 121 015 393 207 857.3
$^{199}Hg^+$	$5d^{10}6s^2\,{}^2S_{1/2}$ - $5d^96s^2\,{}^2D_{5/2}$	282	1 064 721 609 899 145.3
$^{171}Yb^+$	$6s\,{}^2S_{1/2}$ - $5d\,{}^2D_{3/2}$	436	688 358 979 309 308.3
$^{171}Yb^+$	${}^2S_{1/2}$ - ${}^2F_{7/2}$	467	642 121 496 772 645.0
^{171}Yb	$6s^2\,{}^1S_0$ - $6s6p\,{}^3P_0$	578	518 295 836 590 864.0
$^{88}Sr^+$	$5s\,{}^2S_{1/2}$ - $4d\,{}^2D_{5/2}$	674	444 779 044 095 486.6
^{87}Sr	$5s^2\,{}^1S_0$ - $5s5p\,{}^3P_0$	698	429 228 004 229 873.2

can stabilize an electromagnetic radiation to an atomic transition in the optical frequency domain instead of a microwave transition such as the cesium frequency standard, the stability will benefit from the larger transition frequency f_0. This is the strongest motivation for developing atomic clocks based upon optical transitions. This thesis discusses the development and advancement of one such optical clock based upon the "forbidden" transition $|^1S_0\rangle \leftrightarrow |^3P_0\rangle$ of $^{27}Al^+$.

1.1 Optical Frequency Standards

In 1983, the International Committee for Weights and Measures (CIPM) started to provide recommended values of optical transition frequencies [Quinn 84]. To date, many atomic and molecular transition frequencies in the optical frequency domain are given by the BIPM as shown in Fig. 1.1. Among them, a few atomic transitions have been chosen as secondary representations of the SI second [Taylor 08], which are summarized in Table 1.1. These optical atomic clocks are based on either trapped ions, such as $^{27}Al^+$, $^{199}Hg^+$, $^{171}Yb^+$, and $^{88}Sr^+$, or neutral atoms in optical lattices, such as ^{171}Yb and ^{87}Sr. The proposed atomic transitions with natural linewidth $\lesssim 1$ Hz are forbidden transitions between two $J = 0$ electronic states, quadrupole transitions, or octupole transitions [Taylor 08, Ludlow 15].

The invention of the optical frequency comb in 1999 simplified absolute measurements of optical frequencies [Ye 05] and sped up the development of optical atomic clocks. After almost

Figure 1.1: Frequency standards recommended by the BIPM. The image is taken from Ref. [Taylor 08] (`http://www.bipm.org/en/publications/mises-en-pratique/standard-frequencies.html`).

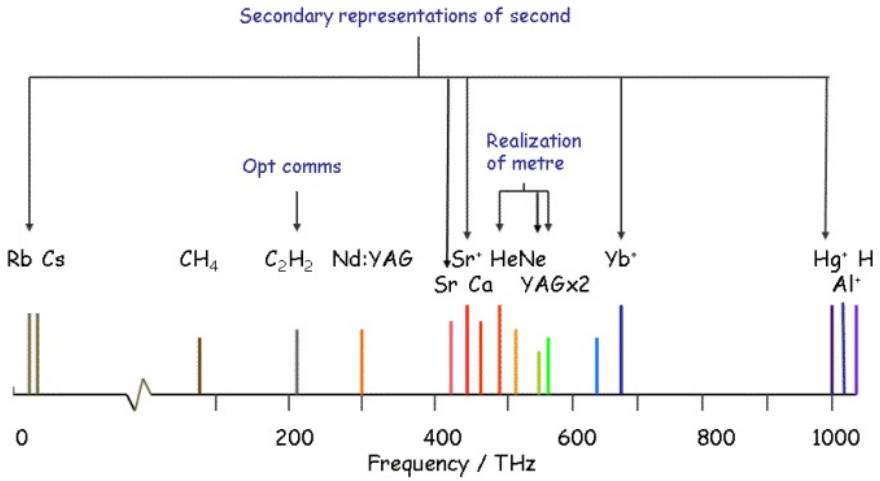

two decades of improvements of optical atomic clocks, current state-of-the-art optical frequency standards outperform the best cesium microwave standards in both accuracy[4] and stability. In fact, the uncertainties of the frequency measurements shown in Table 1.1 are stringently limited by the performance of the cesium atomic clocks, which has triggered a discussion about a possible redefinition of the SI second [Gill 11, Le Targat 13]. The improvement of atomic clock accuracy since the development of cesium atomic clocks back in the 1950s is shown in Fig. 1.2.

Trapped ion and neutral atom optical clocks both have advantages and disadvantages with respect to systematic uncertainty. One of the main sources of systematic uncertainty in optical lattice clocks is due to the optical lattice trapping field that introduces a light shift associated with the differential polarizability between electronic states in the clock transition [Lemke 09, Yamanaka 15, Nicholson 15, Nemitz 16]. On the other hand, one of the main frequency uncertainties in the ion-based optical clocks is the second order Doppler shift, which relates to the design of ion traps and laser cooling [Chou 10a, Huntemann 16]. Both types of optical clocks suffer from a systematic shift due to the environmental blackbody radiation, which can be mitigated by choosing atomic

[4] The accuracy, or inaccuracy, refers to the systematic shift of the atomic clocks, as is normally used in the clock community.

transitions less sensitive to the blackbody radiation, better characterizing the ambient environment [Beloy 14, Nicholson 15], or operating the clocks in a cryogenic environment [Ushijima 15]. To date, optical frequency standards based on either one trapped ion or many neutral atoms have both reached a fractional frequency uncertainty of (2-3) $\times 10^{-18}$ [Nicholson 15, Huntemann 16], which is almost two orders of magnitude more accurate than cesium standards.

Figure 1.2: Clock history. Cesium microwave clock: [Lombardi 07, Jefferts 07, Heavner 14]. Hydrogen atom: [Niering 00]; Calcium atom: [Sterr 04]. Strontium atom: [Boyd 07, Ludlow 08, Bloom 14, Nicholson 15]. Mercury ion: [Udem 01, Oskay 06, Rosenband 08]. Ytterbium ion: [Stenger 01, Huntemann 16]. Strontium ion: [Margolis 04]. Aluminum ion: [Rosenband 08, Chou 10a].

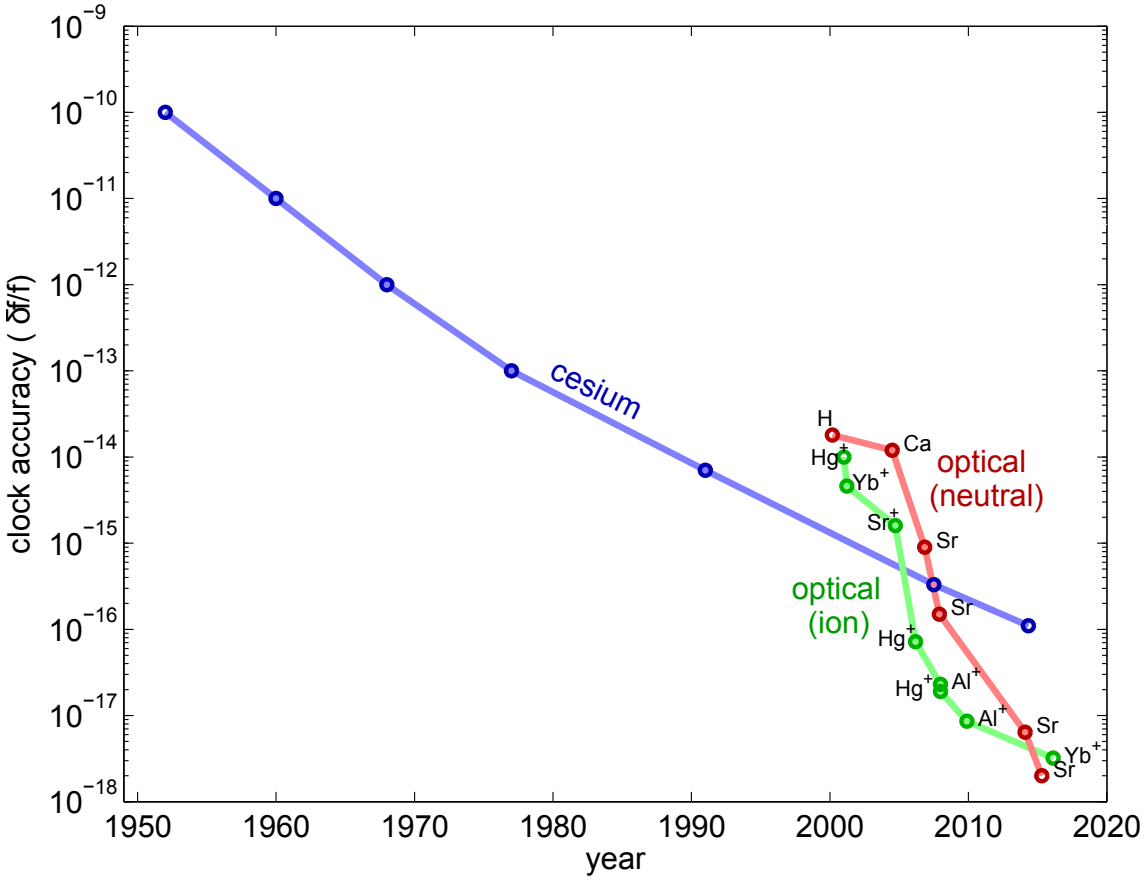

With regards to the clock stability, neutral atom optical clocks typically perform better due to the ability to interrogate multiple atoms simultaneously in the optical lattice in contrast to ion-based atomic clocks [Hinkley 13, Bloom 14, Schioppo 17]. A frequency stability of $6 \times 10^{-17}/\sqrt{\tau}$ in the neutral atom optical clock has been reported recently [Schioppo 17]. On the other hand,

interrogating multiple ions simultaneously in an ion-based atomic clock to improve the stability generally leads to a degradation of the clock accuracy because of the finite size of trapping volume and accompanying micromotion shift. The stability of trapped ion optical clocks only reaches about $2 \times 10^{-15}/\sqrt{\tau}$, limited by the quantum projection noise [Chou 10a, Dubé 15]. Therefore, carefully designed trapping potentials for multiple ions [Pyka 13, Keller 15] and clock operation protocols for a single trapped ion [Chou 11b, Hume 16] were both introduced to improve the stability issue for ion-based atomic clocks.

1.2 Optical Clock Applications

As optical atomic clocks have improved, applications in several fields have been proposed [Maleki 05, Ludlow 15]. For example, the long-term stability will benefit local time-keeping [Weiss 10, Riehle 17] and navigation in deep space missions [Major 07, Prestage 09]. Stable and accurate optical clocks may simplify communication algorithms by making it possible to implement a downlink-only operation instead of a two-way configuration [Prestage 09]. In addition, optical clocks can be used in conjunction with the optical frequency division technique to generate ultra-low phase noise radio frequency signals that can improve radar systems [Fortier 11].

Another potential application is in the field of geophysics. Current advanced optical clocks can detect centimeter-level changes of the gravitational potential [Chou 10b], which may help us understand the dynamics of the interior structure of the Earth and improve earthquake prediction and volcanology [Bondarescu 15]. Moreover, two separated optical clocks linked by an optical fiber can monitor the relative geopotential change on a short-term basis, which will benefit the study of periodic effects such as the solid Earth tide [Bondarescu 15, Takano 16].

In addition, the higher accuracy and better stability of optical clocks also serve as a test bed for fundamental physics, such as searches for deviations from the predictions of the theory of relativity [Wolf 09, Flambaum 16, Delva 17], searches for various forms of dark matter [Derevianko 14], and searches for physics beyond the standard model [Dzuba 99]. These potential applications all motivate further development of better optical atomic clocks.

1.3 $^{27}Al^+$ Optical Clocks

While an optical frequency standard utilizing the forbidden $|^1S_0\rangle \leftrightarrow |^3P_0\rangle$ transition of $^{27}Al^+$ as well as other Group IIIA elements was proposed in the early 1980s [Dehmelt 82], high precision spectroscopy of $^{27}Al^+$ was not achieved until the proposal of the quantum logic spectroscopy in 2001 [Wineland 02] and later the realization in 2005 [Schmidt 05]. The lack of light sources for the lowest dipole-allowed transition $|^1S_0\rangle \leftrightarrow |^1P_1\rangle$ and the narrower linewidth of the intercombination transition $|^1S_0\rangle \leftrightarrow |^3P_1\rangle$ make direct atomic state discrimination through state-dependent fluorescence and laser cooling challenging. To overcome this, a "logic ion" co-trapped together with the $^{27}Al^+$ serves as the coolant and atomic state discriminator. The $|^1S_0\rangle \leftrightarrow |^3P_0\rangle$ clock transition was observed and its absolute frequency was measured at National Institute of Standards and Technology (NIST) in 2007 [Rosenband 07]. Since then, two $^{27}Al^+$ optical clocks were constructed and evaluated before the work described in this thesis commenced [Rosenband 08, Chou 10a]. The systematic shifts and uncertainties reported in the literature are summarized in Table 1.2. The effect of the ion's motion contributes significantly to the total systematic uncertainty. In contrast to other atomic species in Table 1.1, given the same amount of kinetic energy, the relatively smaller mass of $^{27}Al^+$ gives rise to a larger frequency shift due to the second-order Doppler (time dilation) effect. Hence, controlling ions' motion is more challenging in $^{27}Al^+$ optical clocks compared to other trapped-ion optical frequency standards. The biggest advantage of the clock transition $|^1S_0\rangle \leftrightarrow |^3P_0\rangle$ in $^{27}Al^+$ is its extremely low sensitivity to the ambient temperature. Characterization of the blackbody radiation environment in which the atoms are immersed is difficult because all surrounding surfaces contribute. Therefore, it usually requires a significant experimental and theoretical effort to evaluate the frequency shift due to blackbody radation in optical atomic clocks [Beloy 14, Nicholson 15, Dolezăl 15, Zhang 17]. However, $^{27}Al^+$ has the smallest temperature dependence among known atomic electronic transitions proposed for optical frequency standards in neutral atoms and singly-charged ions. This is due to two fortuitous properties of $^{27}Al^+$.

(1) All dipole-allowed transitions connecting to the $^1S_0$ and $^3P_0$ states are in the deep ultraviolet

Table 1.2: Systematic shifts and uncertainties in previous $^{27}Al^{+}$ optical clocks. Values are from Ref. [Rosenband 08] and Ref. [Chou 10a].

Contributor	Fractional frequency $\times 10^{18}$	
	Clock 1	Clock 2
Excess micromotion	$-(20.0 \pm 20.0)$	$-(9.0 \pm 6.0)$
Secular motion	$-(16 \pm 8)$	$-(16.3 \pm 5.0)$
Blackbody radiation shift	$-(12.0 \pm 5.0)$	$-(9.0 \pm 3.0)$
Cooling laser Stark shift	$-(7.0 \pm 2.0)$	$-(3.6 \pm 1.5)$
Quadratic Zeeman shift	$-(453.0 \pm 1.1)$	$-(1079.9 \pm 0.7)$
Electric quadrupole	(0.0 ± 0.5)	–
Linear Doppler shift	(0.0 ± 1.0)	(0.0 ± 0.3)
Clock laser shift	–	(0.0 ± 0.2)
Background-gas collisions	(0.0 ± 0.5)	(0.0 ± 0.5)
AOM phase chirp	(0.0 ± 0.1)	(0.0 ± 0.2)
Total	$-(508 \pm 23)$	$-(1117.8 \pm 8.6)$

region. Therefore the clock transition is less disturbed by the blackbody radiation, which has a wavelength of about $10\,\mu m$ at room temperature.

(2) The polarizabilities of the $^{1}S_0$ and $^{3}P_0$ states partially cancel each other.

Therefore we only require control of the thermal environment to within 10 K near room temperature to achieve a fractional frequency uncertainty $< 1.0 \times 10^{-18}$. This property is particularly advantageous for building transportable optical frequency standards.

The first two $^{27}Al^{+}$ optical clocks built at NIST were used to demonstrate some of the applications of optical clocks in fundamental physics. The first example set a constraint on the temporal variation of the fine structure constant, α [Rosenband 08]. Repeated measurements of the frequency ratio of the clock transitions of $^{27}Al^{+}$ and $^{199}Hg^{+}$ optical clocks over the course of a year were used to place a stringent limit on the temporal variation of α of $(-1.6 \pm 2.3) \times 10^{-19}$ per year, which is still one of the tightest constraints given by laboratory tests [Huntemann 14, Godun 14]. Another example was the examination of the gravitational red shift by comparing the transition frequencies of two $^{27}Al^{+}$ optical clocks, one of which was raised by $33\,cm$ relative to each other [Chou 10b]. The measurement agreed with the prediction of the theory of relativity

for gravitational time dilation. These two experiments demonstrated the potential applications of $^{27}Al^+$ optical clocks, and future work will explore further possibilities with $^{27}Al^+$ clocks.

1.4 Thesis Organization

This thesis discusses the construction and evaluation of the third $^{27}Al^+$ optical clock at NIST. The thesis is organized as follows. In Chapter 2, the experimental apparatus will be described. Some technical aspects implemented in the current $^{27}Al^+$ optical clock to improve its performance will also be discussed in this chapter. In Chapter 3, the details of a protocol to operate the $^{27}Al^+$ clocks near the three-dimensional (3D) motional ground state will be presented. This protocol helps reduce the time dilation shift and uncertainty due to the secular motion by more than an order of magnitude. Other important systematic uncertainties and considerations will be discussed in Chapter 4. Finally, a preliminary uncertainty evaluation of the current $^{27}Al^+$ optical clocks will be presented at the end of the thesis.

Chapter 2

Experimental Setup

When I joined the Al^+ optical clock project in 2011, former members had shown a very promising accuracy [Chou 10a] and demonstrated impressive possible applications [Rosenband 08, Chou 10b]. To use it as a frequency standard, the questions arising from previous experiences are clear,

> *How can we improve the $^{27}Al^+$ optical clock setup to make the clock more accurate and reliable?*

The $^{27}Al^+$ optical clock is a complicated system that involves ultimate control of both laser fields and electric signals to manipulate the atomic states in a vacuum enclosure. Therefore, simplifying the system to meet the minimum requirements for the clock operation seems like a reasonable route to take for reliability reasons. On the other hand, the accuracy of previous clocks was mainly limited by the second order Doppler shifts. One of the sources is from the excess micromotion due to the trap imperfections, which basically sets the hard limit of the clock accuracy once the trap is sealed into the vacuum. Combining all these thoughts, designing a new system specifically for clock applications is a natural approach, and this was the starting point in my graduate study. In this chapter, I will describe the techniques implemented in the new $^{27}Al^+$ optical clock systems to improve their accuracies and reliabilities.

2.1 The Trap

Unlike other single-ion optical clock systems utilizing spherical Paul traps to achieve an ultimate frequency accuracy of quadrupole transitions [Huntemann 16, Nisbet-Jones 16], the $^{27}Al^{+}$ optical clock requires a linear Paul trap to trap more than one ion simultaneously for sympathetic cooling and atomic state determination [Raizen 92, Schmidt 05]. In addition, the existence of the static electric field gradient in a linear Paul trap will not lead to a significant quadrupole shift because the $^{27}Al^{+}$ clock transition connects two $J = 0$ states, in which the electronic charge distribution cannot have multipole moments [Beloy 17][1] . A typical linear Paul trap is a quadrupole mass filter with an additional electrostatic potential applied at both ends to provide the axial confinement as shown in Fig. 2.1. This configuration has an axis in which the radio frequency (rf) electric field is ideally zero, which enables trapping multiple ions with minimum exposure to the rf field. Here, I briefly explain the motion of a single ion inside a linear Paul trap as the theoretical background. For an ideal case, the ion experiences zero rf force at any position along the trap axis; therefore the ion's axial (z) motion, independent of the rf potential, can to a good approximation be expressed as a one-dimensional oscillator and its Hamiltonian H_z is given by

$$\begin{aligned} \mathrm{H}_z &= \frac{p_z^2}{2m} + \frac{m\omega_z^2}{2} z^2, \\ \omega_z &= (2\kappa Q U_z/m)^{1/2}, \end{aligned} \tag{2.1}$$

where (z, p_z) are canonical position and momentum variables and ω_z is the characteristic angular frequency of the trapping potential U_z in the axial direction. Here m and Q are the mass and the charge of the ion. The geometric factor κ depends on the geometry of the trap electrodes. Therefore the motion in the z direction is a textbook harmonic oscillator. The transverse (x and y) motion of an ion is more complicated, which is confined by a harmonic pseudopotential resulting from the rf field; its equation of motion is described by the Mathieu equation. Following the coordinates and notations in the ion trapping literature [Ghosh 95, Wineland 98], the ion's transverse motion

[1] Linear Paul traps for multiple clock ions have also been designed and proposed to improve the clock stability [Pyka 13].

is approximately given by

$$u_i = A_i \left(\cos(\omega_i t + \phi_i) \left[1 + \frac{q_i}{2} \cos(\Omega_T t) + \frac{q_i^2}{32} \cos(2\Omega_T t) \right] + \beta_i \frac{q_i}{2} \sin(\omega_i t + \phi_i) \sin(\Omega_T t) \right), \quad i \in \{x, y\}, \tag{2.2}$$

where x and y are mutually orthogonal directions transverse to z, A_i and ϕ_i depend on the initial conditions, and $V_0 \cos(\Omega_T t)$ is the applied rf potential[2] . The characteristic angular motional frequency in the transverse direction ω_i is given by

$$\begin{aligned} \omega_i &= \beta_i \frac{\Omega_T}{2}, \\ \beta_i &\approx \left(a_i + \frac{q_i^2}{2} \right)^{1/2}, \\ & i \in \{x, y\}. \end{aligned} \tag{2.3}$$

Here the Mathieu parameters a_i and q_i depend on the trapping conditions and are defined by,

$$a_i \equiv \frac{4QU_i}{m\Omega_T^2 R^2}, \quad i \in \{x, y\}, \tag{2.4}$$

$$q_x = -q_y \equiv -\frac{2QV_0}{m\Omega_T^2 R^2}, \tag{2.5}$$

where U_i is the electrostatic potential in the transverse direction, and R is the distance between the ion and the electrode in the transverse direction. In general, we operate our system in the regime $a_i \ll q_i^2 \ll 1$; therefore, the ion's motion in the transverse directions becomes,

$$u_i \simeq A_i \left(\cos(\omega_i t + \phi_i) \left[1 + \frac{q_i}{2} \cos(\Omega_T t) \right] \right) = A_i \cos(\omega_i t + \phi_i) + A_i \frac{q_i}{2} cos(\omega_i t + \phi_i) \cos(\Omega_T t), \tag{2.6}$$

$$\omega_i \simeq \frac{QV_0}{\sqrt{2}\Omega_T m R^2}. \tag{2.7}$$

In Eq. (2.6), we call the first oscillation term with the smaller frequency and the larger amplitude the secular motion and the second term the micromotion. For the ideal linear Paul trap, there is no pure frequency component at the rf drive frequency Ω_T and no micromotion in the z direction. Unfortunately, we always find that the pure tone at Ω_T exists in the ion's motion in the real trap configurations [Berkeland 98]. We call the motion at Ω_T the excess micromotion, which arises from

[2] The phase of the rf field is omitted here.

the imperfections of trapping potential. Through the derivation above, we find that the potential of a linear Paul trap can be approximated to be a three dimensional (3D) harmonic well with the characteristic frequencies $\{\omega_x, \omega_y, \omega_z\}$, such that the ions' motion can be quantized and described by a Fock state distribution.

Figure 2.1: Linear Paul trap schematic.

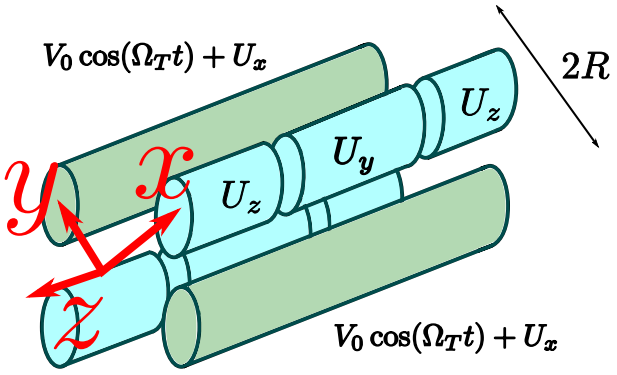

Two previous versions of ion traps used in Al^+ optical clock experiments are depicted in Fig. 2.2. The first trap was made of a stack of alumina wafers [Rowe 02] while the second one was made of blade-shaped beryllium-copper electrodes [Chou 10a]. In both traps, we found the tolerance of the machining and the assembly contributed significantly to the trap imperfection. Starting in 2011, we worked on the design of a new type of single-zone linear Paul trap to provide a tighter tolerance and simpler assembly process. We call this new design the "Wheel Trap." As mentioned above, the machining and the assembling tolerances are two of the main sources of imperfections. However, current state-of-the-art wafer fabrication technology can achieve an extremely tight tolerances. Therefore, we designed the wheel trap with all four-rod electrodes fabricated in a single diamond wafer and thereby eliminate imperfections due to assembly errors. In fact, this also simplified the assembly process considerably. We can usually assemble a trap and vacuum system in one day. All traps were designed in-house and fabricated by Diamond Material in Germany[3] .

[3] Diamond Materials, `http://www.diamond-materials.com`

Figure 2.2: Ions traps used in previous Al^+ optical clock experiments. Images are taken from [Hume 10]. (a)A photograph of the first Al^+ clock ion trap. (b)A drawing of the second Al^+ clock ion trap.

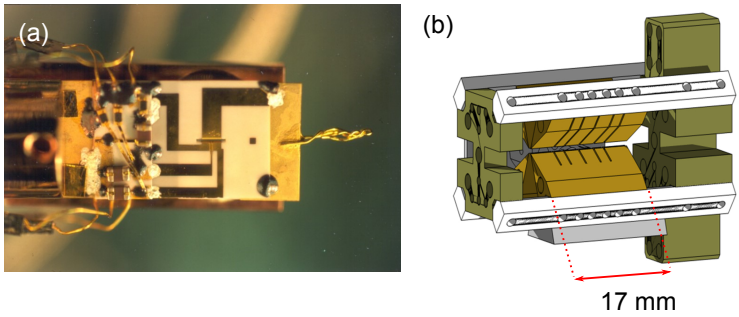

The wheel trap schematic and pictures are shown in Fig. 2.3 and Fig. 2.4. The traps were first laser-machined to the desired shape from CVD diamond wafers. Afterwards the traps were masked and gold-sputtered to define both the rf and dc electrodes. Four finger structures pointing towards the center act as the four rod electrodes in the conventional linear Paul trap design. Ions are trapped in the center of the four finger electrodes. This trap design not only provides a tight machining tolerance but also is capable of generating a strong trap potential with a few hundred micrometers ion-to-electrode spacing in comparison with the planar design. This benefits laser cooling and is crucial to minimize the heating due to ambient electric field noise [Turchette 00a, Brownnutt 15, Chen 17]. Moreover, using the diamond as the substrate material improves the heat dissipation, which is critical for characterizing the clock shift due to the blackbody radiation.

Since 2011, there were several iterations of wheel traps being designed and fabricated. Some of the key differences in these iterations are summarized in Table 2.1. To achieve stronger transverse confinement at a given rf power, the rf field is applied to all four electrodes with 180° phase difference between two neighboring electrodes [4] . For the versions A, B, and D, all four electrodes are electrically independent and two rf voltage built-up center-tap resonators are used to generated the rf potentials. The balance of the amplitude and the phase between the two resonators is the most difficult task for this type of design. Diagonal electrodes in the version C and E are hard-wired

[4] In fact, this trap would have strong axial rf confinement in comparison with the elongated design of other linear Paul traps, if it were driven single ended.

Figure 2.3: (a) The version A wheel trap schematic. Colored regions are gold sputtered and the same color indicates the same rf voltage and phase. The inner surfaces of four finger electrodes are used to trap ions. (b) A microscopic picture of the trap center. The distance between two diagonally opposed electrodes is $500\,\mu m$.

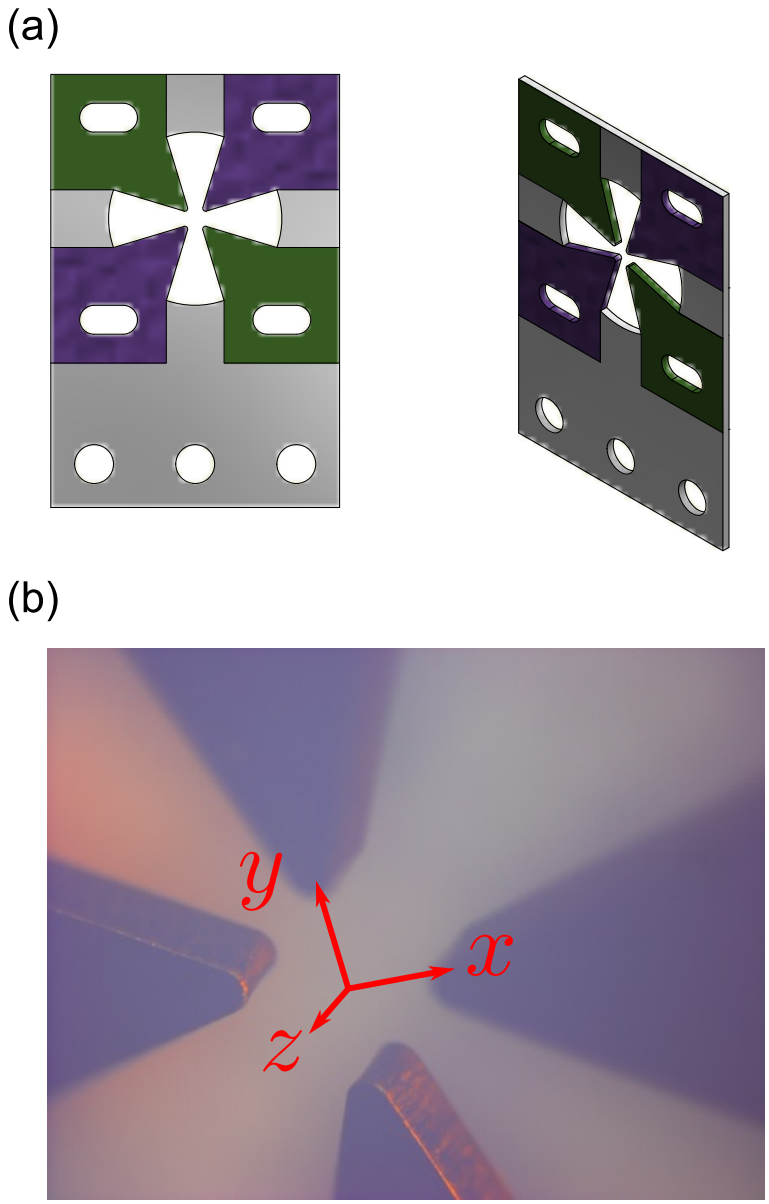

Figure 2.4: Photographs of five versions of wheel traps. The differences between them are summarized in Table 2.1.

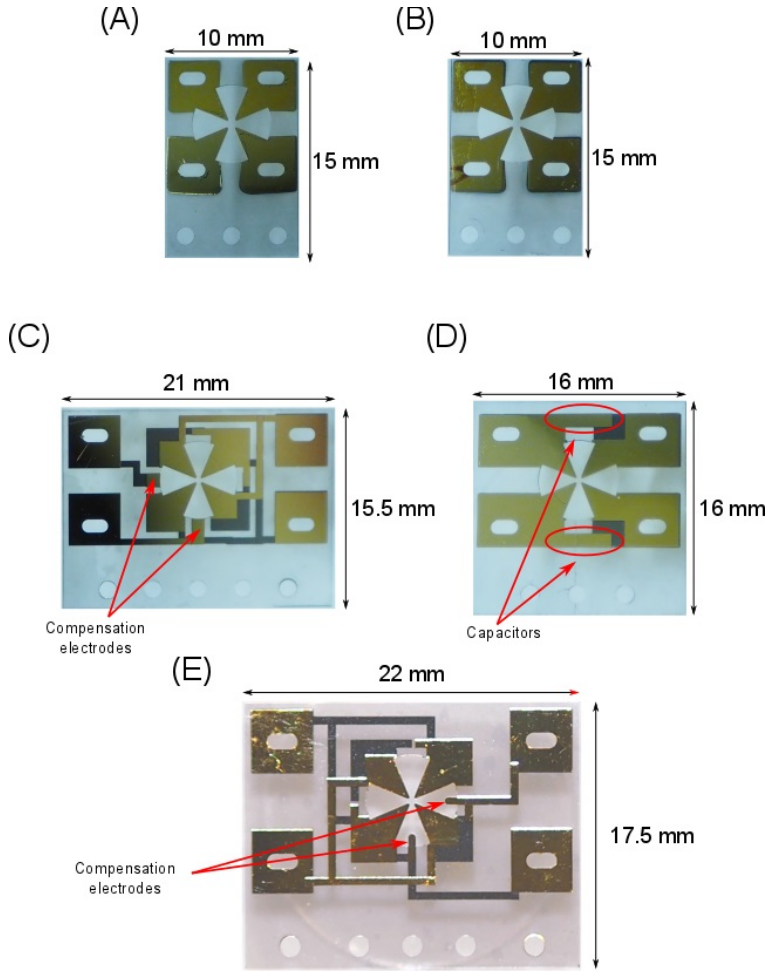

connected on the wafer and only one resonator is used. The detailed rf circuitry will be discussed in the next section.

The versions A and B attempt to maintain the symmetry as much as possible to minimize the excess micromotion along the trap axis. However, this symmetric design leads to a degeneracy of the dipole and quadrupole modes driven by the two rf resonators, as shown in Fig. 2.5. In fact, we observed the frequency differences between the dipole and the quadrupole modes was less than 1 MHz. Although we intended to drive the two resonators out of phase, very small phase imbalances excited the dipole mode and gave rise to the excess micromotion in the directions perpendicular

Table 2.1: Iterations of wheel traps developed at NIST since 2011.

Version	A	B	C	D	E
Ion-electrode spacing [μm]	250	400	250	250	250
Thickness [μm]	300	300	300	300	500
Electrode design	symmetric	symmetric	diagonally hard-wired	capacitively coupled	diagonally hard-wired
Status	retired	retired	on duty: Mg^+-Al^+	on duty: Ca^+-Al^+	under construction

to the trap axis. To resolve this problem, we designed two new versions of the trap. In version D, the symmetry is broken by adding about 1 pF capacitance in the top and bottom electrode pairs. The capacitor is fabricated by overlapping gold pads on two surfaces of the wafer and using the substrate as the dielectric material. The add-on capacitance separates the dipole mode and the quadrupole mode by about 5 MHz. Given the rf drive frequency $\Omega_T \simeq 2\pi \times 76$ MHz and the quality factor $\mathcal{Q} \simeq 100$ of our rf resonators, this reduces the dipole excitation significantly. A wheel trap C is currently installed in the Ca^+-Al^+ optical clock system.

Figure 2.5: The dipole (a) and the quadrupole (b) fields generated from two rf resonators. C: capacitor that breaks the frequency degeneracy of dipole and quadrupole fields.

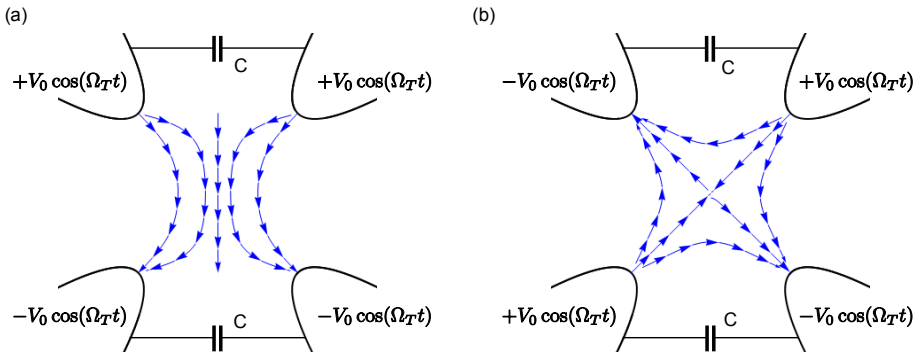

An alternative construction method is to connect the diagonal electrodes on the trap wafer and use a single rf resonator to drive the trap, which was implemented in the versions C and E. Using one resonator eliminates the effort of balancing the phase and amplitude of two resonators and

eliminates the dipole mode; however, losing the ability of individually controlling the dc voltages and rf phases of four rf electrodes leads to a requirement for two additional dc electrodes to compensate the excess micromotion in the transverse direction, which are shown in Fig. 2.4. In addition, these two compensation electrodes break the overall electrode symmetry, which requires a careful design of conductive traces on the wafer to cancel out the rf fields at the trap center as shown in Fig. 2.4. Another important advantage of the hard-wired trap designs is to eliminate the differential noise between two rf power lines, which is injected onto the trap and heats the ions. In our experience, we usually saw lower and more stable heating rates in the hard-wired trap designs. Currently a version C trap serves as the center of the Mg^+-Al^+ optical clock system. Most of the experiments throughout this thesis were conducted using version C. Version E is an upgrade of version C which is designed to provide less excess micromotion. A vacuum chamber with a version E trap is currently being built.

2.2 Trap System

In addition to the trap wafer itself, several hardware components need to be installed together for an ion trap. I will discuss them in this section.

2.2.1 Vacuum Chamber

A drawing of our vacuum system is shown in Fig. 2.6. An octagon (Kimball Physics, MCF275-SphOct-C2A8) provides all required optical accesses. Two cubes (Kimball Physics, MCF275-SphCube-C6) are connected and mounted to the bottom of the octagon. One thermocouple feedthrough, one BNC feedthrough, one ion gauge, one all-metal valve, and one vacuum pump are connected to these two cubes. The ion gauge was only turned on during the initial pumping-down process to monitor the pressure and is left off during normal operation to avoid heating the system. To reduce hydrogen outgassing, all stainless steel parts except the vacuum pump were baked at 400°C in vacuum for around a week before the trap assembly [Park 08]. A NEXTorr

D100-5 vacuum pump from SEAS Group[5] , consisting of a 100 l/s non-evaporable getter (NEG) pump and a 6 l/s ion pump, is used to maintain vacuum. After finishing the trap assembly, the system was baked at 150°C and pumped by a pumping station for about three days to reach 10^{-11} torr pressure level measured by the ion gauge attached to the chamber. The ion pump was flashed and the NEG pump was activated close to the end of the bake.

Figure 2.6: CAD drawing of the vacuum chamber. Red: vacuum pump; yellow: ion gauge; magenta: thermocouple feedthrough; green: all-metal valve; blue: optical viewport; pink: electrical feedthrough. Cage adapters next to six 1.33-inch viewports are used to attache optics close to the chamber.

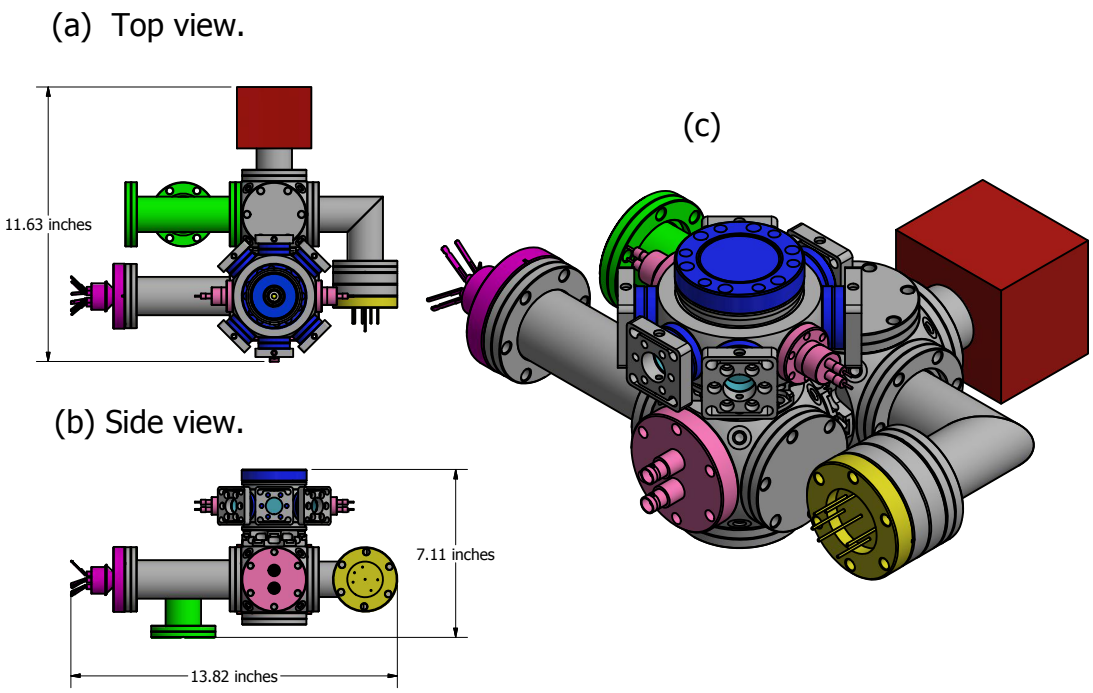

Inside the chamber, the trap wafer is mounted on the top of a copper post and sandwiched by the titanium beam pick-off as shown in Fig. 2.7. The top surface of the beam pick-off is mirror-polished and used to reflect the laser beam vertically towards the ion to provide the three-

[5] https://www.saesgetters.com/

dimensional characterization of the ion's motion. The post is silver-electroplated to improve the thermal contact conductance and acted as a heat sink to remove the heat deposited in the wafer [Li 00]. The post is screwed to a copper disk at the bottom of the chamber, which also served as a gasket to seal the bottom flange. Two titanium "endcap" electrodes are also mounted on the top of the post. Two 45° surfaces of each endcap electrode are also mirror-polished for laser beam path stabilization. Endcap electrodes are connected to the top flange of the octagon using the modified groove grabbers (Kimball Physics, MCF275-GrvGrb-C02) to minimize the cantilever motion of the post. A natural abundance magnesium wire and an aluminum wire were mounted on one of the endcap electrodes and served as the sources of neutral atoms. All trap mounting hardware made of stainless steel was heat-treated and carefully selected to minimize stray magnetic fields around the center of the trap.

Figure 2.7: (a) A drawing of the electrical connections to the trap wafer and the mounting scheme of the trap and the endcap electrodes. MM: micromotion. (b) A photograph taken during the trap assembly before the electrical connections were made. A thermocouple sensor hanging next the post was clamped against the trap wafer by the beam pick-off to monitor the trap temperature. Both endcap electrodes are isolated from the copper post by alumina washers, which can be seen in (b).

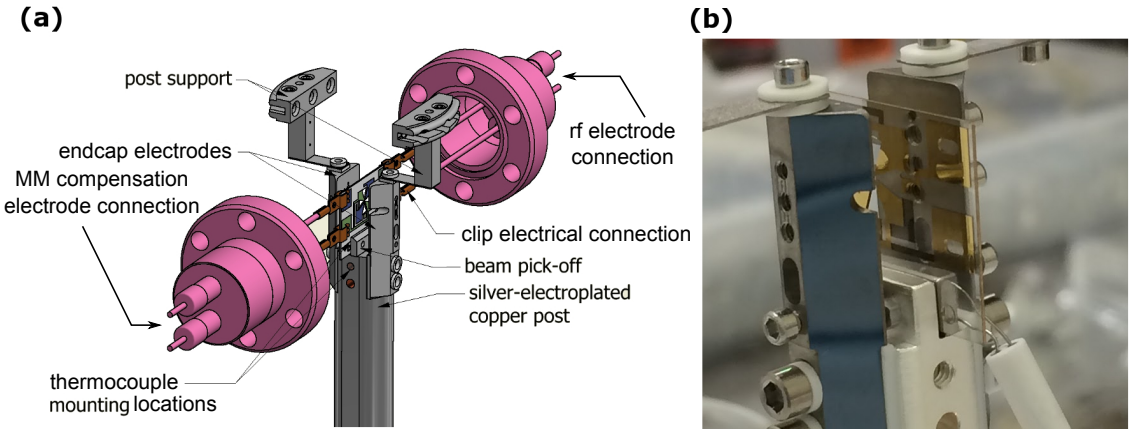

The purposes of the seven viewports are shown in Fig. 2.8. Six uncoated fused silica viewports are mounted to the octagon for access of laser beams. Home-made cage adapters were bolted down against these six viewports for easily attaching optics to the chamber. Two molybdenum

feedthroughs mounted on the octagon were mechanically connected to the trap wafer to apply the rf potential and the dc compensation voltages. The BNC feedthrough was connected to two end-cap electrodes for the axial confinement, which were held at different electrical potentials. The top flange of the octagon was used for the fluorescence collection where a fused silica viewport with a broadband anti-reflective coating was mounted (MPF, A8001-1-CF.) There were three thermocouple sensors inside the chamber to monitor the trap temperature. One is mounted between the wafer and the beam pick-off, as shown in Fig. 2.7, while the other two are mounted at the top and the bottom of the post, respectively.

2.2.2 Imaging and Photon Collection System

The imager was designed in-house using off-the-shelf components. Two aspheric lenses (Asphericon GmbH, A50-60FPX-S-X) next to the viewport act as a relay lens system to form an ion image outside the vacuum chamber. Afterwards, a 40X microscope objective lens (Thorlabs LMU-40X-UVB) in combination with an infinity-corrected lens magnifies the image and projects it onto an electron multiplying charge-coupled device (EMCCD) camera (Andor Technology, iXon DU885). A $200\,\mu m$ diameter pinhole is mounted in the focal plane of the objective lens to minimize the background photon counts. A flipper mirror is mounted right after the objective lens to send the ion fluorescence to either the camera or the photomultiplier tube (PMT). We use a PMT from Hamamatsu, part number R7600P-203, which has a 35% quantum efficiency at $280\,nm$. The overall photon collection efficiency is about 0.5%. This simple and economical design provides us with the necessary spatial resolution to resolve two ions in the camera, which are typically a few μm apart for our trap conditions.

Between the two aspheric lenses, a small aluminum mirror is installed to provide vertical laser beam access. The incoming laser is focused by the aspheric lens towards the ion at 10° with respect to vertical, and then is reflected off the beam pick-off mounted on the post, and finally exits the chamber.

Figure 2.8: Laser beam geometry in the horizontal plane of the trap axis and the quantization axis. Two vertical beams are not shown here. Ion loading beams: ablation and Al PI. $^{25}Mg^{+}$ beams: FD, D, R, RR, BR-a, BR-t, and BR-co. $^{27}Al^{+}$ beams: Clock, $^{3}P_1\,\pi$ and $^{3}P_1\,\sigma^{+/-}$. Refer to Sec. 2.3, Sec. 2.5, and Sec. 2.4 respectively for the detail.

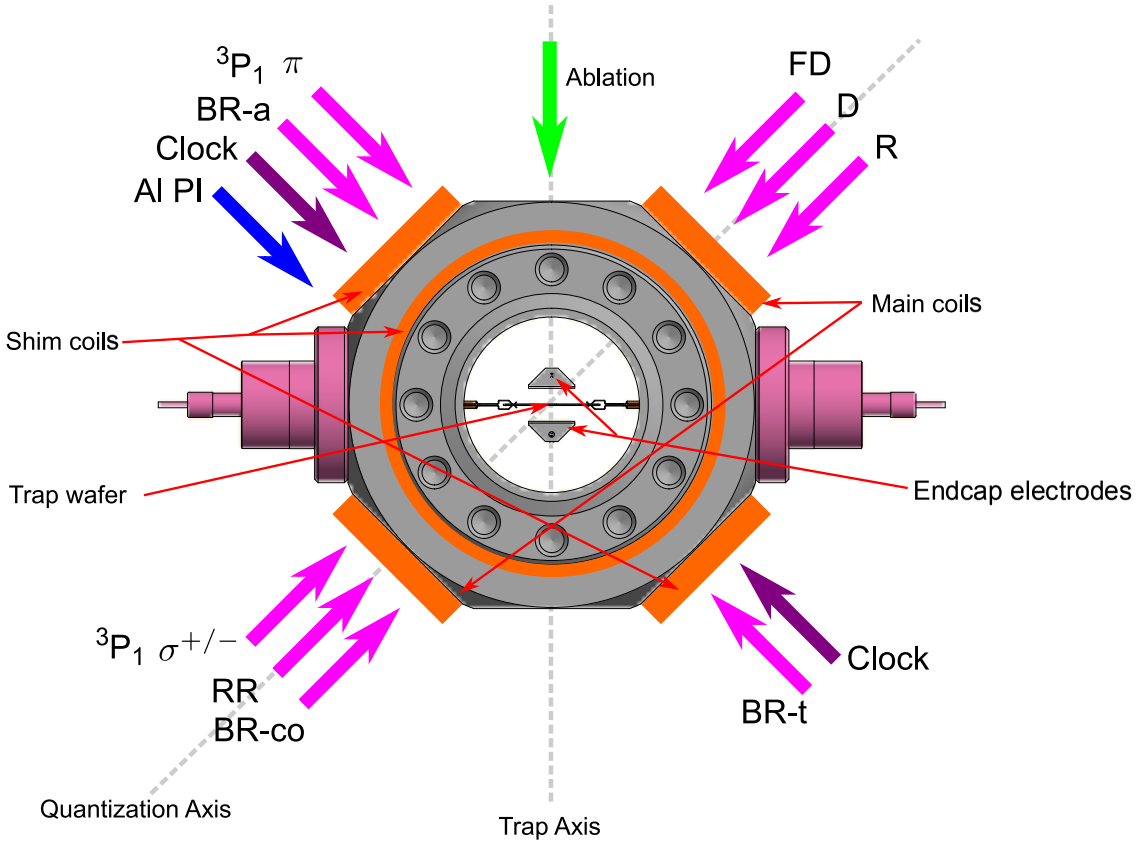

Figure 2.9: Section view of the imaging and photon collection system. WD: working distance. NA: numerical aperture. EMCCD: electron multiplying charge-coupled device. PMT: photomultiplier tube. Blue: optical viewport flanges. Cyan: optical viewports and lenses.

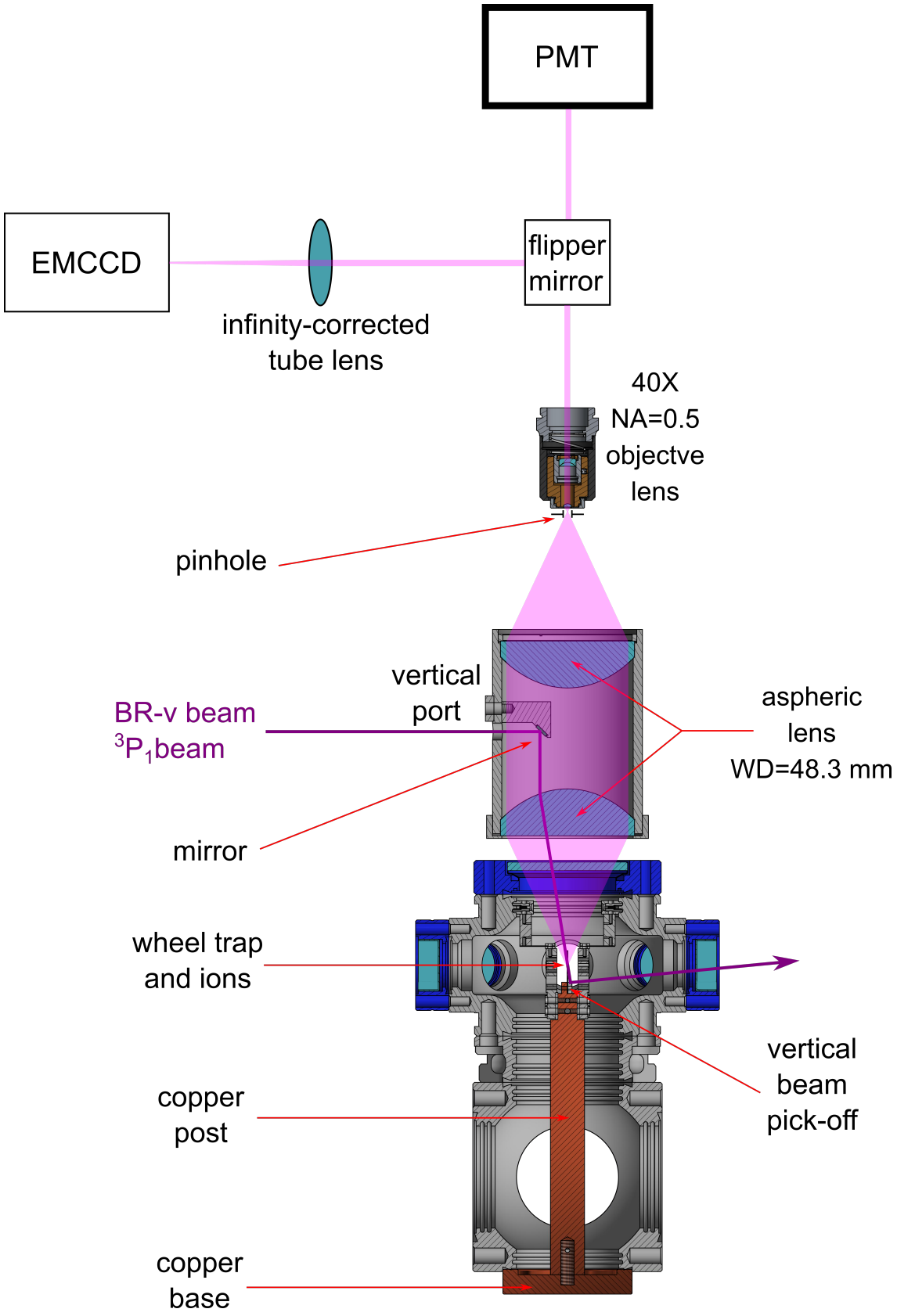

2.2.3 RF Resonator and RF Power Control

An rf resonator is usually used in macroscopic Paul traps. The idea is to generate the trap rf potential using the high-voltage end of the resonator. The resonators not only serve as step-up transformers but also spectral filters. Historically, coaxial resonators and helical resonators were installed in ion traps in our group, which generally have quality factors $\mathcal{Q} \gtrsim 100$ [Jefferts 95, Poitzsch 96]. These types of resonators are typically made of copper and constructed by conventional machining techniques, which tend to be heavy, expensive, and large. Therefore, we developed new resonators based on meander traces on both sides of printed circuit boards (PCB) as shown in Fig. 2.10. The resonant frequencies can be adjusted by changing the number of loops shown in Fig. 2.10. By moving the input small-loop antenna relative to the resonator, the rf input is impedance matched and coupled to the resonator. For this design, the dielectric loss of the PCB substrate is a limiting factor with regards to how efficient the voltage step-up can be. Benefiting from mature PCB manufacturing, we can easily achieve $\mathcal{Q} \simeq 100$ by choosing industrial standard Rogers material[6] as the substrate, and resonators for different rf drive frequencies can be made without too much difficulty. This gives us more flexibility to test different rf drive frequencies easily.

Figure 2.10: The schematic of meander line resonators. Red and blue meanders are conductive traces printed on different surfaces of the PCB. The left side of the board is connected to the rf feedthrough, which is in pink in Fig. 2.6.

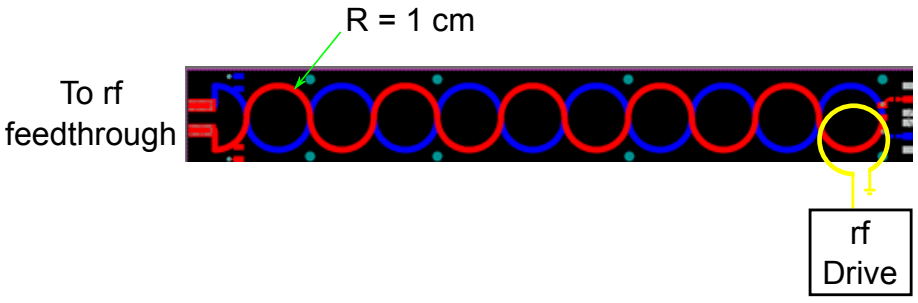

In the experiments, the rf potential may fluctuate due to thermal effects from either the rf resonator or the rf amplifier, which causes the secular frequencies to change. Moreover, we

[6] https://www.rogerscorp.com/index.aspx

often change the rf potential in order to deterministically control the ions' position, which tends to increase the rf power fluctuations. In principle, we can intermittently measure the transverse secular frequencies and feed back to the rf power controller during the clock operation. However, this is not favorable because it will reduce the clock duty cycle and hence hurt the clock stability [Dicke 53]. Therefore, we stabilize the pick-up rf power measured on one of the dc electrodes instead, which should stabilize the pseudopotential. The rf power is measured by a home-made detector based on an rf envelope tracking IC (Analog Devices, ADL5511), and referenced to a dc voltage. The generated error signal is then processed by a digital servo [Leibrandt 15] and fed to a voltage controlled variable gain amplifier.

2.2.4 Magnetic Field Control

As shown in Fig. 2.8, five coils are wrapped on the octagon directly to provide the necessary control of the magnetic field. Coils at the opposite viewports are connected in series to form a Helmholtz-type coil. The coil that defines the quantization axis is driven at around 300 mA by a diode laser current driver (Arroyo Instruments, 4205-DR) with an impedance matching circuit. A low-temperature-coefficient precision resistor is connected in series with the main coil next to the chamber to monitor the current. The main coil generates about 1.1 G along the quantization axis at the position of ions. The rest of the coils are shim coils and driven by dc power supplies to compensate the background magnetic field. Alignment of the laser beam and B-field direction is achieved by minimizing the $|\uparrow\rangle$ component when a $^{25}Mg^{+}$ is prepared in the $|\downarrow\rangle$ state when the circularly polarized detection beam is applied.

2.3 Ion Loading

Historically, loading ions into a trap using a thermal atomic beam from a resistively heated oven followed by either electron impact ionization or isotope-selective photoionization (PI) has been used in the NIST Ion Storage group. However, after successfully loading an ion, the oven temperature may take a certain amount of time to cool down, which may perturb the optical clock

transition frequency via blackbody radiation. Moreover, an oven generates a continuous atomic beam while we only need to load a single ion. The large number of atoms may contaminate the vacuum significantly after the loading process and possibly deposit atoms on the trap electrodes and dielectric surfaces, which may build up charges and even change the heating rate over time. To resolve these problems, we implemented laser ablation loading in our new trap system.

Figure 2.11: Al and Mg natural abundance ablation targets installed on one of the endcap electrodes.

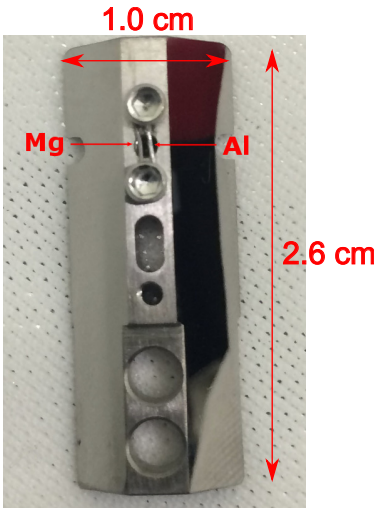

Ablation targets are installed on one of the endcap electrodes and held at the endcap potential, as shown in Fig. 2.11. This prevents electrons, possibly generated from the ablation process, from being deposited on the dielectric materials. Both targets are high purity, natural abundance wires of 10 mil (254 μm) diameter. For aluminum, there is only one stable isotope, ^{27}Al. For magnesium, three stable isotopes exist, $^{24,\,25,\,26}$Mg, and only 10% of the natural abundance is the desired isotope, $^{25}Mg^{+}$, while about 80% is ^{24}Mg. The distance from the targets to the center of the trap is 8 mm. The essential energy levels of ^{27}Al and ^{25}Mg related to the ionization process are shown in Fig. 2.12. To laser-ablate the neutral atoms from the target, we use a Q-switched frequency-doubled Nd:YLF laser at 523 nm (CrystaLaser QL523-500-O). The laser beam is focused onto the target, passing through apertures in both endcap electrodes and the trap center. The laser beam waist radius on the target is measured to be about 30 μm. A motorized mirror and an acousto-

optic modulator (AOM) are used to steer the beam and control the ablation power. The loaded $^{25}Mg^{+}$ is distinguished from the other isotopes using the laser-induced fluorescence at the 280 nm transition $|^2P_{3/2}, F = 4\rangle \leftrightarrow |^2S_{1/2}, F = 3\rangle$ while the $^{27}Al^{+}$ is recognized by measuring the axial secular frequency of a $^{25}Mg^{+}$-$^{27}Al^{+}$ pair. We check if a desired ion is loaded after every single pulse of the ablation laser.

Figure 2.12: Energy level diagrams of Mg and Al (not to scale). Values are taken from NIST Atomic Database, `http://www.nist.gov/pml/atomic-spectra-database`.

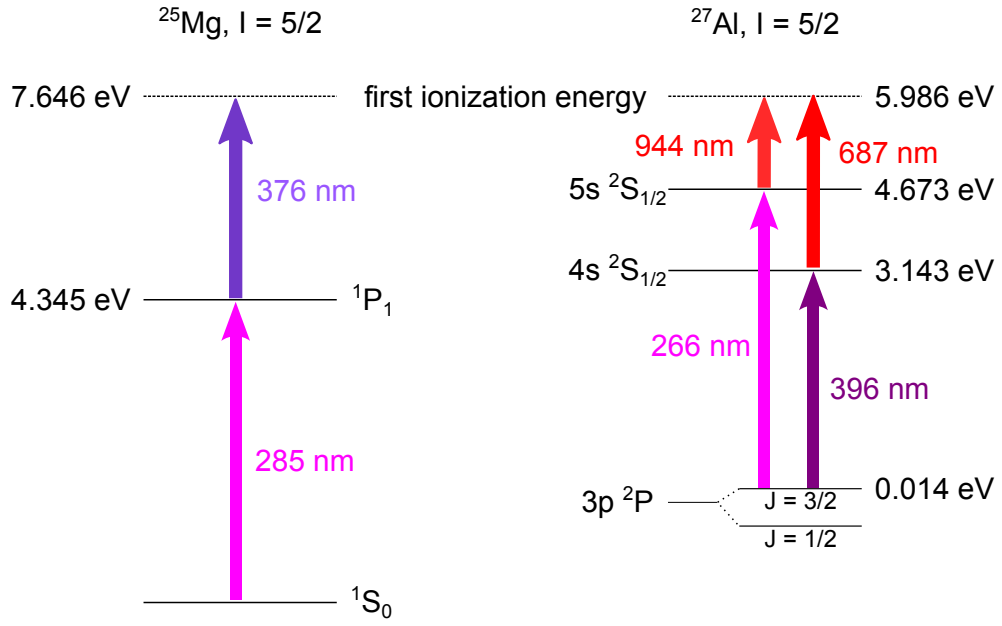

To load a $^{25}Mg^{+}$, the ablation beam is first steered towards the Mg target. A Doppler cooling beam, which is 400 MHz red-detuned from the $|^2P_{3/2}, F = 4\rangle \leftrightarrow |^2S_{1/2}, F = 3\rangle$ cycling transition, is turned on when the ablation laser is fired. Following this, a 20 MHz red-detuned Doppler cooling beam is turned on for 250 μs. Finally, a resonant laser pulse is sent to collect the fluorescence. The first thing we noticed is that ions can be generated and loaded into the trap in the absence of the photoionization light source at 285 nm, which was not seen before when using a resistively heated oven. The exact mechanism is not fully understood but a possible explanation is the generation of excited-state atoms during the laser ablation process followed by field ionization due to the trap rf field [van Ingen 96, Gürtler 04, Hendricks 07, Sheridan 11]. A typical pulse fluence to load a

$^{25}Mg^+$ is about 1.2 J/cm^2. Since our Mg^+ loading mechanism is independent of the isotopes and the ablation target is naturally abundant, to isotope-selectively load $^{25}Mg^+$ might be troublesome. Fortunately, the cooling light for $^{25}Mg^+$ in fact heats the most abundant isotope, $^{24}Mg^+$, and rejects the loading of the $^{24}Mg^+$ [Drullinger 80]. We do load $^{26}Mg^+$ occasionally, but $^{26}Mg^+$ can be dumped out of the trap easily by lowering the trap rf potential while keeping the existing $^{25}Mg^+$, if any, in the trap.

To load $^{27}Al^+$ efficiently, we find a PI laser is required. In the previous trap, a continuous-wave (cw) diode laser at 396 nm was used in a (1+1) resonance-enhanced multi-photon ionization (REMPI) process via the $|4s\,^2S_{1/2}\rangle$ state [Chou 10a]. In the new trap, we use a pulsed frequency-quadrupled Nd:YAG laser (Teem Photonics, STU-01E, < 0.4 ns pulse duration) and the $|5s\,^2S_{1/2}\rangle$ as the intermediate state. Although the transition rate via the $|5s\,^2S_{1/2}\rangle$ state is weaker, the higher peak power at 266 nm still provides sufficient ionization rate. In addition, this turn-key and maintenance-free laser reduces the work regarding the ion-loading. The PI process is accomplished by temporally and spatially overlapping the laser pulse with the atomic flux ablated from the target.

Based on our loading experience, we find the loading efficiency highly depends on the surface properties of the ablation target. Firing the ablation pulses on the same spot will eventually generate a "dead spot" that loses the ability to load ions. To avoid this, we randomly choose a new spot, which needs to be at least one beam waist away from the previous loading attempt, before each shot of the ablation laser by adjusting the deflection AOM frequency. The process to load a $^{25}Mg^+$ and a $^{27}Al^+$ is automated and the flowchart of the loading process is shown in Fig. 2.13.

2.4 $^{27}Al^+$ Laser System

To operate the $^{27}Al^+$ optical clock utilizing quantum logic spectroscopy, we need two coherent light sources at 267 nm to address the transitions between $|^1S_0\rangle \leftrightarrow |^3P_1\rangle$ and $|^1S_0\rangle \leftrightarrow |^3P_0\rangle$. In this section, I will describe the implemented laser systems for $^{27}Al^+$.

Figure 2.13: Flowchart of the automatic ion loading.

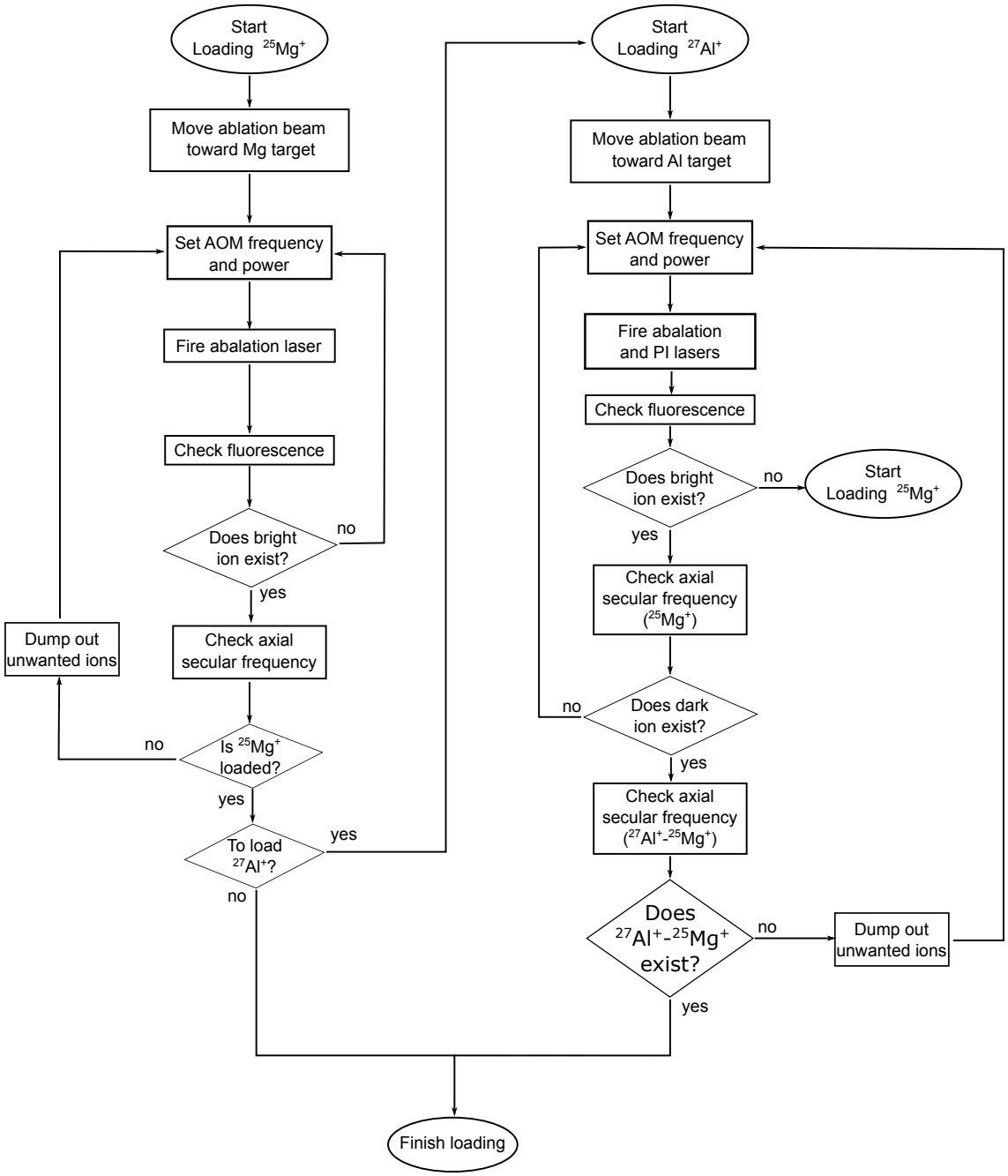

2.4.1 Energy Levels and Lasers

The relevant energy levels of $^{27}Al^+$ are shown in Fig. 2.14. The intercombination transition $|^1S_0\rangle \leftrightarrow |^3P_1\rangle$ is used for micromotion characterization and quantum logic read-out, while the transition $|^1S_0\rangle \leftrightarrow |^3P_0\rangle$ is the forbidden transition used as the optical frequency standard. We name the laser systems addressing these two transitions using the term symbols of the excited state, $^3P_1$ and $^3P_0$, respectively. Both laser systems are frequency-quadrupled fiber lasers. The IR sources are narrow-linewidth (Lorentzian FWHM $<$ 5 kHz) seed lasers made by NP Photonics, Inc. The two fiber lasers are further amplified by continuous wave (cw) ytterbium fiber amplifiers (Keopsys Group) to generate 1-2 Watts of optical power in the infrared (IR). The IR light is afterwards frequency-doubled to the visible (VIS) using single-pass periodically poled lithium niobate (PPLN) second-harmonic-generation (SHG) waveguides (NTT Electronics, custom modules) which is then doubled to the ultraviolet (UV) by home-made ring cavity frequency doublers using beta barium borate (BBO) crystals. Typically, $8\,mW$ of $^3P_1$ UV power and $700\,\mu W$ of $^3P_0$ UV power are obtained from the resonant UV doublers. The UV output power is stabilized by adjusting the input VIS pump power. Currently these two lasers are frequency narrowed and stabilized to high finesse cavities in the visible, which will be described later. The $^{27}Al^+$ laser beams at $267\,nm$ are reflected off of dichroic filters (Semrock, FF01-267/LP-25) before going into the vacuum chamber to overlap with the $^{25}Mg^+$ laser beams at $280\,nm$. To maintain the Gaussian beam profile and to avoid polarization distortion, the incident angle of the filter needs to be less than 5°. Both colors share the same focusing lenses and waveplates, which are attached to the chamber using home-made cage adapters. The difference of retardances between $267\,nm$ and $280\,nm$ for typical zero-order waveplates is less than 0.05 waves, which does not limit our experiments. However, chromatic aberration of the focusing lenses is observed and hence near one-to-one telescopes are installed in the $^{27}Al^+$ laser beam paths for compensation.

The laser beam geometry and AOM setup for $^{27}Al^+$ are shown in Fig. 2.15. To fully characterize the micromotion of the $^{27}Al^+$, three nearly mutually orthogonal $^3P_1$ beam lines are im-

Figure 2.14: Energy level diagram of $^{27}Al^{+}$.

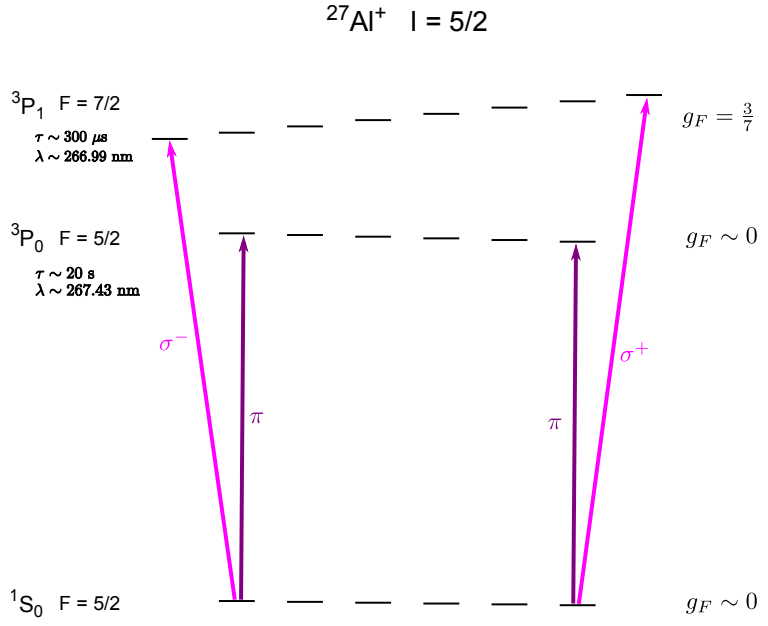

plemented. Two of them are perpendicular to the quantization axis and π-polarized, while the third one is along the quantization axis and also serves as the $^{27}Al^{+}$ state preparation beam. An electro-optic modulator (EOM) is installed in the state preparation beam to switch between the σ^{+} and the σ^{-} polarizations, which is used to pump the $^{27}Al^{+}$ to the stretched Zeeman levels, $|^1S_0,\ F = 5/2,\ m_F = 5/2\rangle$ and $|^1S_0,\ F = 5/2,\ m_F = -5/2\rangle$, respectively for the cancellation of the first-order Zeeman shift [Bernard 98]. Two counterpropagating $^3P_0$ (clock) beams are set up perpendicular to the quantization axis to drive the transitions $|^1S_0,\ F = 5/2,\ m_F = \pm 5/2\rangle \leftrightarrow |^3P_0,\ F = 5/2,\ m_F = \pm 5/2\rangle$, which provides cancellation of the first-order Doppler shift.

2.4.2 Frequency Stabilization of the $^3P_1$ Laser

The $^3P_1$ laser is frequency stabilized to the same ultra-low expansion (ULE) reference cavity used for the $^{25}Mg^{+}$ laser using the Pound-Drever-Hall (PDH) locking technique [Drever 83]. The locking scheme is depicted in Fig. 2.16. The $^{25}Mg^{+}$ and the $^3P_1$ laser beams are frequency-doubled to the VIS and sent through the cavity in opposite directions. The error signal is first filtered and

Figure 2.15: $^{27}Al^+$ laser beamlines. RD: resonant frequency doubler. All $^{27}Al^+$ beams are overlapped with the $^{25}Mg^+$ beams lines using dichroic beam combiners shown in Fig. 2.19. The EOM is used to switch the polarization between σ^+ and σ^- to optically pump the $^{27}Al^+$ to the desired Zeeman state.

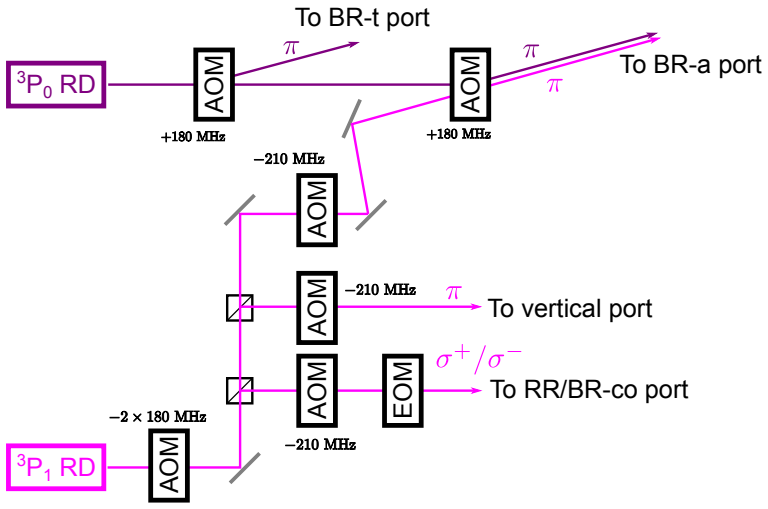

integrated using a digital servo box [Leibrandt 15], and then feeds back to both the piezoelectric transducer (PZT) of the seed laser and an AOM. The 88-mm- long ULE cavity is housed in a stainless steel vacuum can without active temperature stabilization. Typically $\sim$ 30 Hz/s of frequency drift in the VIS is observed due to the variation of the ambient temperature.

2.4.3 Frequency Stabilization of the $^3P_0$ Laser

Similarly, the $^3P_0$ laser is frequency referenced to a ULE high finesse cavity using the PDH locking scheme [Young 99]. However due to the narrower transition linewidth, the performance of the frequency stabilization is more demanding. The frequency stabilization set up is depicted in Fig. 2.17. The 24-cm-long ULE reference cavity is housed inside a temperature-controlled aluminum vacuum can, which is both thermally and vibrationally well isolated from the environment. The reference cavity finesse is measured to be about 400 000 in the VIS. The error signal feeds back to both the PZT of the seed laser and an AOM in IR by a digital servo box, which also controls the temperature of the seed laser to improve the long-term performance of the frequency stabilization. The phase noise introduced in the fiber link between the reference cavity and the UV frequency

Figure 2.16: $^{27}Al^{+}$ $^{3}P_1$ laser frequency stabilization scheme. Note that the transition frequency is based on one frequency comb measurement and the systematic shifts have not been evaluated.

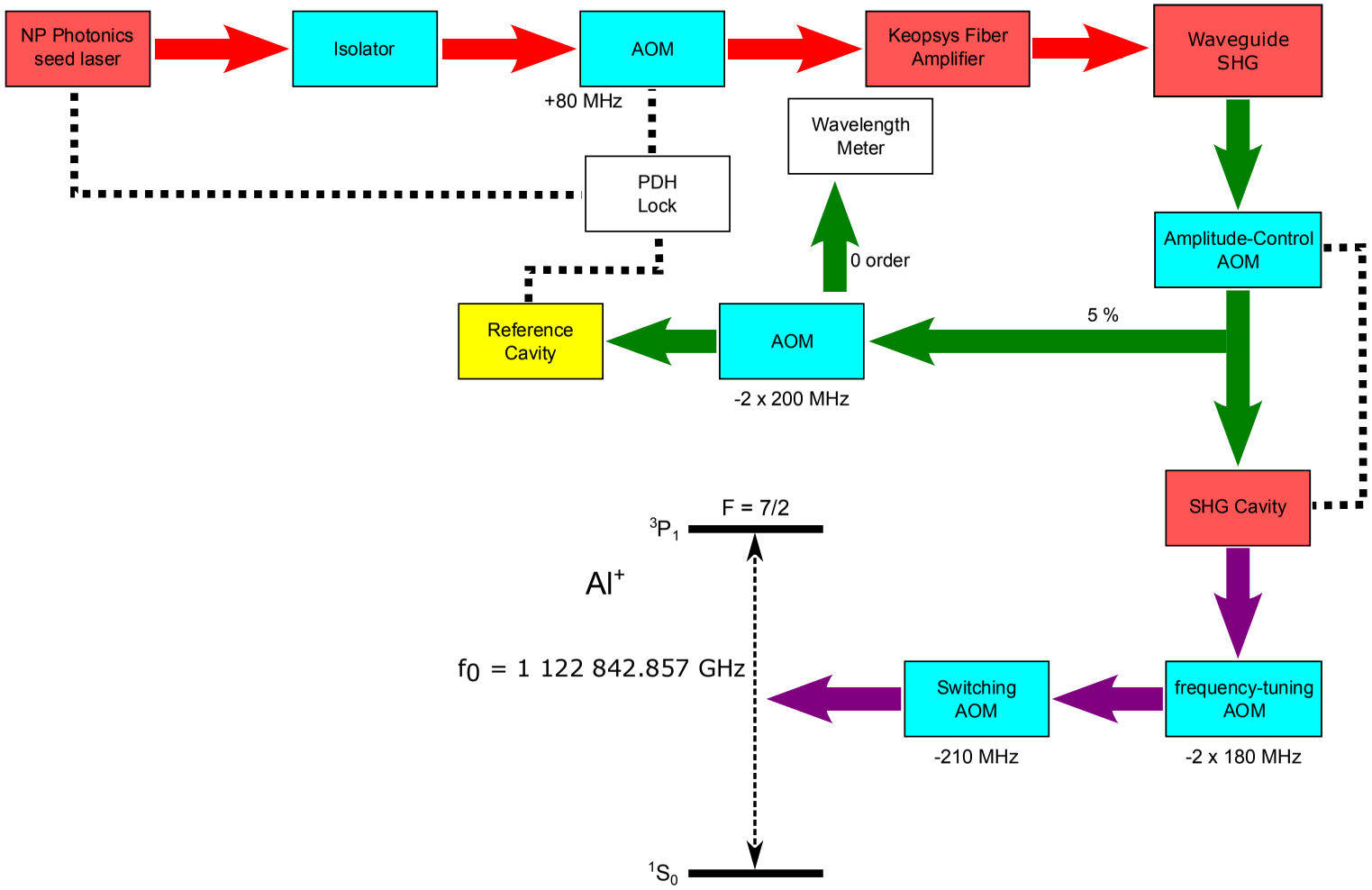

doubler is actively canceled using a standard fiber-noise cancellation scheme [Ma 94, Hume 10].

2.5 $^{25}Mg^{+}$ Laser System

The isotope ^{25}Mg is the only one with a non-zero nuclear spin among three stable magnesium isotopes. The Zeeman levels of hyperfine states in $|^2S_{1/2}, F = 2 \text{ and } 3\rangle$ and $|^2P_{3/2}, F = 3 \text{ and } 4\rangle$ used in the experiments are depicted in Fig. 2.18. Two fiber lasers (Menlo Systems Inc., OrangeOne) are frequency-quadrupled to generate the UV light sources at $280\,nm$ for transitions between $|^2S_{1/2}\rangle$ and $|^2P_{3/2}\rangle$. Similar to the $^{27}Al^{+}$ laser systems, the IR to VIS frequency conversion is conducted by single-pass PPLN SHG waveguides (NTT Electronics, custom modules). The VIS-to-UV frequency doubling is achieved using home-made resonant frequency doublers with BBO crystals [Wilson 11]. One of the fiber lasers is frequency-stabilized to a high finesse cavity (finesse $\mathcal{F} \simeq 75\,000$), made of the ULE glass, utilizing the PDH technique. This laser is used for Doppler laser cooling, quantum bit (qubit) repumping, and atomic state detection. The other laser is free-running and is used to drive stimulated Raman transitions between Zeeman levels of $|^2S_{1/2}, F = 2 \text{ and } 3\rangle$ for quantum logic manipulation and sideband cooling. Typically, we obtain about $15\,mW$ of the UV power pumped by $900\,mW$ of IR laser power. Several AOMs are used for frequency shifting, power control, and timing control. All laser beams, except the one going through the imager, are focused to about $30\,\mu m$ waist radius at the position of ions, measured by the knife-edge method using the trap electrodes. The laser beam geometry and the AOM configurations of the $^{25}Mg^{+}$ laser system are shown in Fig. 2.19, which will be described in detail in the following sections.

2.5.1 Qubit

Given the non-zero nuclear spin, I = 5/2, of the $^{25}Mg^{+}$, the ground state $|^2S_{1/2}\rangle$ splits into two hyperfine levels, $F = 2 \text{ and } 3$, with a frequency difference of about 1.8 GHz as shown in Fig. 2.18. This energy difference significantly reduces the off-resonant transition probability while driving transitions from(to) either of the hyperfine states. In our experiment, two Zeeman levels of

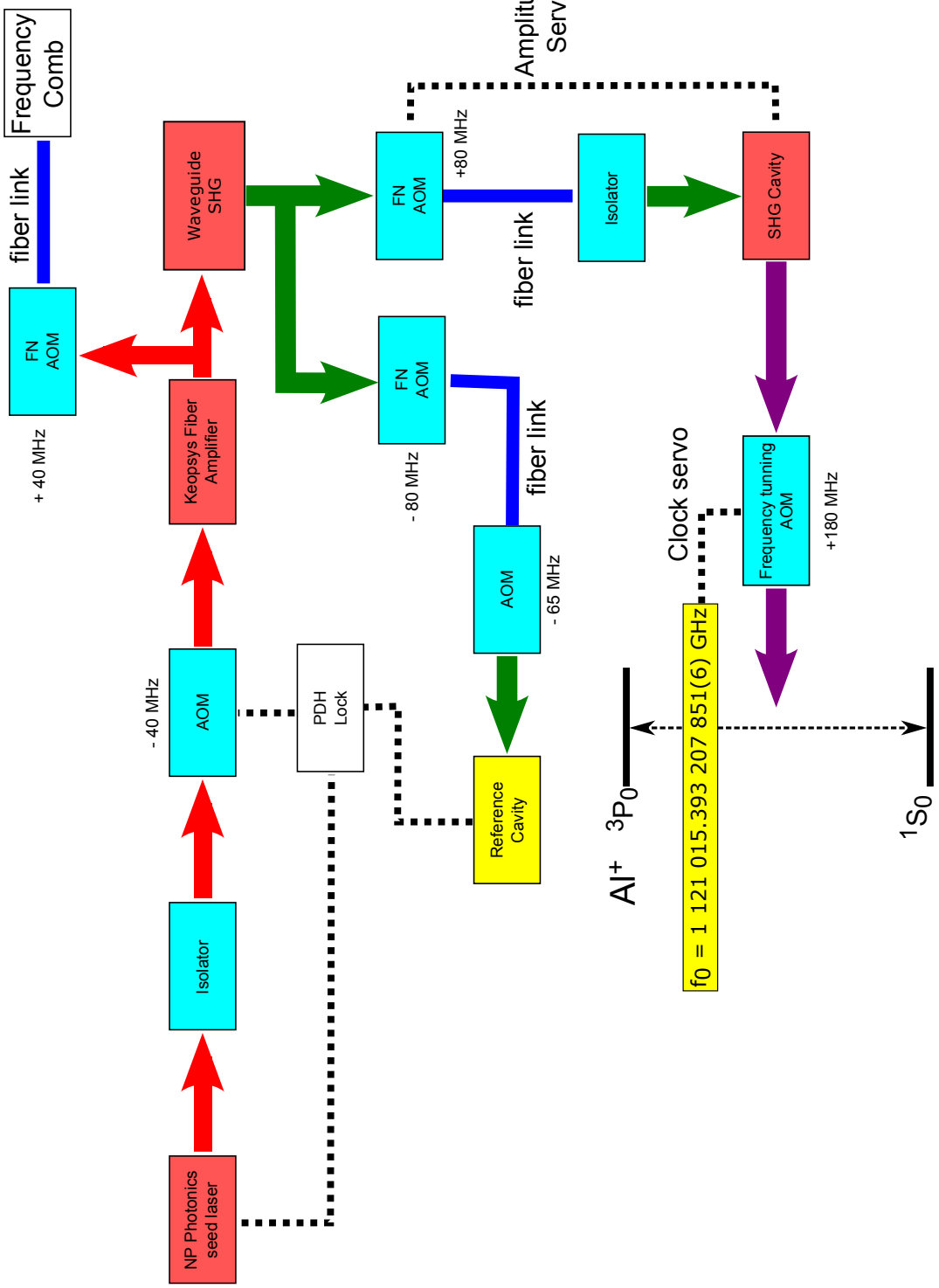

Figure 2.17: $^{27}Al^{+}$ $^{3}P_0$ laser frequency stabilization scheme. FN AOM: fiber-noise cancellation AOM.

Figure 2.18: Relevant energy level diagram of $^{25}Mg^{+}$ (not to scale). D: Doppler cooling, detection; FD: far-detuned cooling; R: repumping; RR: red Raman; BR-a: axial blue Raman; BR-t: transverse blue Raman; BR-v: vertical blue Raman; BR-co: co-propagating blue Raman.

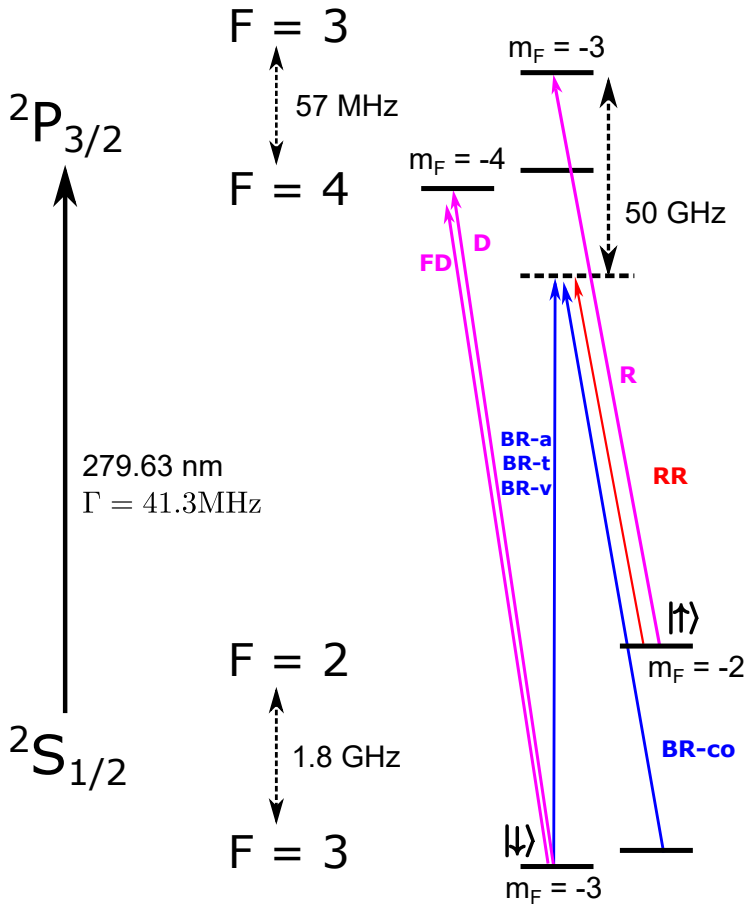

the hyperfine states are used as the qubit states:

$$|\uparrow\rangle \equiv |^2S_{1/2}, F = 2, m_F = -2\rangle, \tag{2.8}$$

$$|\downarrow\rangle \equiv |^2S_{1/2}, F = 3, m_F = -3\rangle. \tag{2.9}$$

The manipulation of qubit states can be achieved by either a Raman two-photon transition or a microwave transition. The discrimination of qubits is essential for both the characterization of ions' secular motion energy and the clock operation, which will be described in Sec. 2.6.1.

Figure 2.19: Schematic of the $^{25}Mg^{+}$ laser beam setup. WSHG: second harmonic generation waveguide; RSHG: resonant second harmonic generation; AOM: acousto-optic modulator; D: Doppler cooling and detection; FD: far-detuned cooling; R: repumping; RR: red Raman; BR-a: axial blue Raman; BR-t: transverse blue Raman; BR-v: vertical blue Raman; BR-co: co-propagating blue Raman.

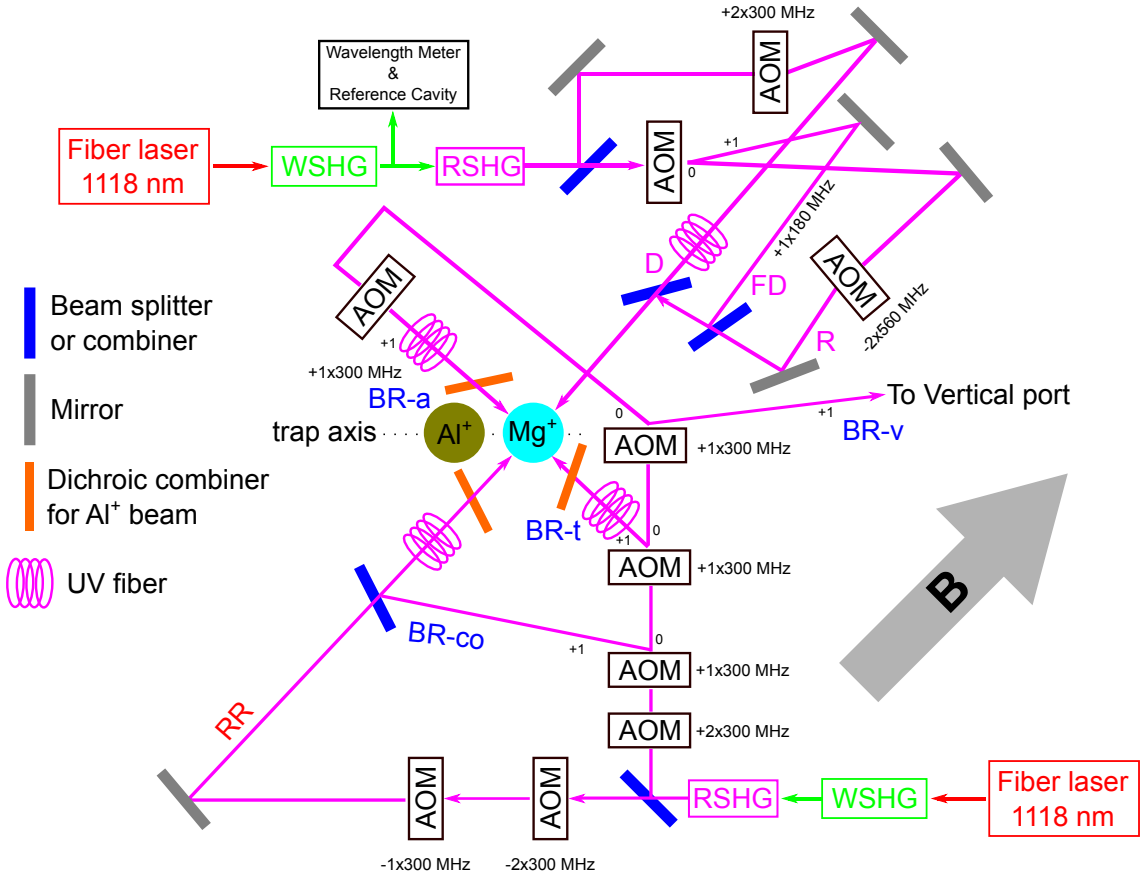

2.5.2 Atomic State Preparation and Doppler Laser Cooling

The Zeeman states $|\downarrow\rangle$ and $|^2P_{3/2}, F = 4, m_F = -4\rangle$ form a closed cycling transition, which is suitable for atomic state preparation and detection. In addition, the 40-MHz transition linewidth is also suitable for Doppler laser cooling. For each experiment, we always start with a 200-μs, σ^--polarized, and $\sim 1\,mW$ cooling pulse at 420 MHz red-detuned from the cycling transition. This far-detuned cooling pulse is efficient to cool hot ions, which might be generated by collisions with background gas. In addition, this intense cooling pulse also plays a role to prepare most of the $^{25}Mg^{+}$ population in the $|\downarrow\rangle$ state. Afterwards, a Doppler cooling pulse of duration $250\,\mu s$ - $2\,ms$

is applied to the ion, which depends on the number and the species of trapped ions. At the end of the experiment, a resonant detection pulse is applied and the laser-induced fluorescence from the cycling transition is collected and detected by the imaging system.

During the experiment, the Doppler cooling pulses and the detection pulses are actively controlled at the same power level. To ensure that the kinetic energy of ions is close to the Doppler limit temperature, we need to keep the laser intensity sufficiently low, with the overhead of a longer cooling time. To characterize the intensity of the Doppler cooling (detection) light, we measure the number of scattered photons using the detection beam when the $^{25}Mg^{+}$ is initially prepared in the $|\uparrow\rangle$ state [Chou 10a]. The number of scattered photons due to a detection pulse of a duration τ in μs can be expressed in terms of the population $\mathcal{P}_{\uparrow(\downarrow)}$ and the photon scattering rate $\Gamma_{\uparrow(\downarrow)}$ in the state $|\uparrow(\downarrow)\rangle$,

$$\begin{aligned}\mathcal{N}_{\gamma}(\tau) &= \eta_{c.e.}\int_{0}^{\tau}(\Gamma_{\downarrow}\mathcal{P}_{\downarrow}(t)+\Gamma_{\uparrow}\mathcal{P}_{\uparrow}(t))\,dt, \\ &= \eta_{c.e.}\mathcal{P}_{\uparrow}(0)\left\{\Gamma_{\downarrow}\tau+\frac{\Gamma_{\uparrow}-\Gamma_{\downarrow}}{\gamma}(1-e^{-\gamma\tau})\right\}\end{aligned} \tag{2.10}$$

where γ is the pumping rate from $|\uparrow\rangle$ to $|\downarrow\rangle$, and $\eta_{c.e.}$ is the collection efficiency of the imager. Given the hyperfine splitting and the branching ratio of the transition $|^{2}P_{3/2}, F=3, m_F=-3\rangle \rightarrow |\downarrow\rangle$, the Eq. 2.10 can be further reduced to,

$$\mathcal{N}_{\gamma}(\tau) = \mathbb{A}\left(\tau+\frac{217}{s}(e^{-\frac{s\tau}{217}}-1)\right) \tag{2.11}$$

where $\mathbb{A}$ is a constant, and $s \equiv I/I_s$ represents the saturation parameter of the laser beam. By fitting $\mathcal{N}_{\gamma}(\tau)$ to the detected photon counts, we can estimate the intensity of the detection and the Doppler cooling beam on the ion. In the experiment, we typically run the experiment with the intensity set to about 10% of the saturation intensity.

2.5.3 Repumping

For some pulse sequences, the $^{25}Mg^{+}$ may have some population in the $|\uparrow\rangle$ after an experiment. To ensure most of the population in the $|\downarrow\rangle$, a repumping pulse sequence is applied. The pulse

sequence starts with a σ^- repumping pulse to clear out the population in $|\uparrow\rangle$ via the transition $|\uparrow\rangle \leftrightarrow |^2P_{3/2}, F = 3, m_F = -3\rangle$. After a repumping pulse, one quarter of the population originally in $|\uparrow\rangle$ will end up in the $|^2S_{1/2}, F = 3, m_F = -2\rangle$ state. Therefore we drive a motion-insensitive, two-photon Raman transition by turning on the red-Raman (RR) and the co-propagating blue Raman (BR-co) lasers simultaneously to bring the $|^2S_{1/2}, F = 3, m_F = -2\rangle$ population back to the $|\uparrow\rangle$ state (see Fig. 2.18 and Fig. 2.19.) By alternating the repumping and the Raman pulses several times, we can move the majority of the population from $|\uparrow\rangle$ to $|\downarrow\rangle$. Typically, our repumping sequence consists of three repumping pulses and two Raman pulses, which means that 98.5% of the population in the $|\uparrow\rangle$ is transferred to the $|\downarrow\rangle$ for ideal π pulses.

2.5.4 Motion-Sensitive Raman Spectroscopy

Figure 2.20: Raman transition spectrum of a $^{25}Mg^+$-$^{27}Al^+$ two-ion pair with all six secular modes of motion resolved. Red: after Doppler cooling. Blue: after Raman sideband cooling. Disappearance of the RSB transitions after Raman sideband cooling indicates the ions' motion is close to the zero point energy.

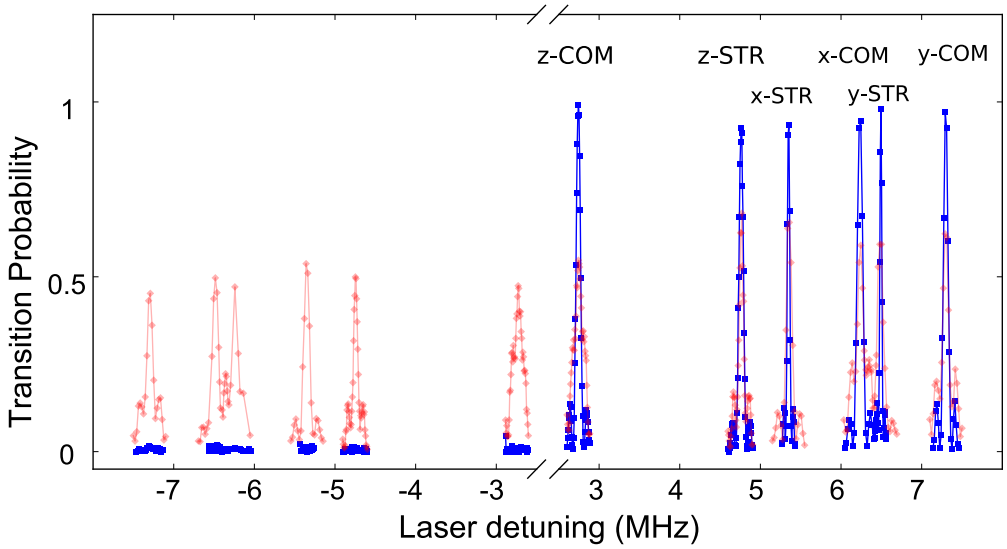

As shown in Fig. 2.18 and Fig. 2.19, we implemented four blue Raman (BR) beams in our system. The RR beam in combination with one of the BR beams can drive Raman transitions within

the hyperfine manifolds of the $|^2S_{1/2}\rangle$ state. In addition, except the BR-co, the differential wave vectors of BR beams and the RR beam have sufficient projections along the directions of the secular modes of motion, which are capable of driving the motional sidebands of the hyperfine transitions. The ability to drive the motion-sensitive Raman transitions is not only crucial to laser cooling and energy characterization but also for clock operation utilizing quantum logic spectroscopy. The axial (BR-a) and the transverse (BR-t) blue Raman beams are used to manipulate the motional quanta in the axial and the transverse directions, respectively, which gives us full control of the ions' motion in all three dimensions. The vertical blue Raman beam (BR-v) is mainly for micromotion compensation. During the experiments, we only manipulate motional quanta between two qubit states, $|\uparrow\rangle$ and $|\downarrow\rangle$. As explained in Sec. 2.1, the ions' motion inside the trap can be described by a Fock state distribution and hence we can separate the Raman transitions into three types. Throughout this thesis, the "carrier" Raman transition denotes the transition with no change of the motional state, while the red-sideband (RSB) and the blue-sideband(BSB) pulses for $^{25}Mg^+$ correspond to the $|\downarrow, n\rangle \rightarrow |\uparrow, n - \Delta n\rangle$ and $|\downarrow, n\rangle \rightarrow |\uparrow, n + \Delta n\rangle$ transitions, respectively, where n is the initial Fock state and Δn, the order of the sideband transition, represents the number of quanta changed by a laser pulse. With our Raman beam setup, we have demonstrated cooling of the motion of a $^{25}Mg^+$-$^{27}Al^+$ two-ion pair in all three dimensions by applying numerous RSB Raman pulses to the trapped ions followed by repumping sequences [Chen 17]. A typical Raman transition spectrum of a $^{25}Mg^+$-$^{27}Al^+$ two-ion pair as shown in Fig. 2.20 indicates that we have cooled the ions to near the 3D zero point energy. More details will be discussed in the next chapter.

2.6 Other Techniques

2.6.1 Maximum-Likelihood Probability Estimation

In our experiment, the mean photon counts collected during the detection time of 250 μs from $|\downarrow\rangle$ and $|\uparrow\rangle$ are about 8 and 0.9, respectively, and the two counts histograms overlap significantly as shown in Fig. 2.21. The observed histograms in the experiment typically result from the scattered

Figure 2.21: Typical photon histograms scattered from $|\downarrow\rangle$ and $|\uparrow\rangle$.

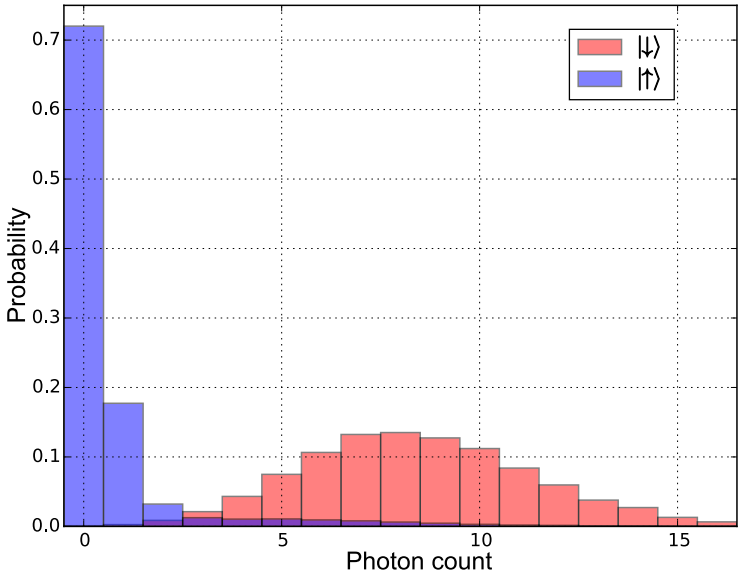

photons from a linear combination of two states and we find that applying a threshold to the photon counts is not sufficient to extract state populations at the 0.1 % level. To extract the probability in $|\downarrow\rangle$, we use a maximum-likelihood estimation method to analyze our data. Before experiments start, we need two reference histograms, $\mathcal{P}(k|\downarrow)$ and $\mathcal{P}(k|\uparrow)$, corresponding to the probability of observing k photons in $|\downarrow\rangle$ and $|\uparrow\rangle$, respectively. We determine reference histograms experimentally by taking fluorescence measurements when the ions are prepared in the states of $|\uparrow\rangle$ or $|\downarrow\rangle$. The state $|\downarrow\rangle$ is prepared by applying a repumping pulse sequence after Doppler cooling while $|\uparrow\rangle$ is prepared by applying a microwave π pulse from $|\downarrow\rangle$. During the experiment, we record a series of photon counts $\{k_i\}$ from a particular quantum state $|\Psi\rangle = \sqrt{p}\,|\downarrow\rangle + \sqrt{(1-p)}\,e^{i\phi}\,|\uparrow\rangle$ in m measurements, where p denotes the population in $|\downarrow\rangle$ and ϕ is the relative phase between $|\downarrow\rangle$ and $|\uparrow\rangle$. The errors in preparation of $|\downarrow\rangle$, $|\uparrow\rangle$ and the superposition states are negligible and do not contribute significantly to the determination of the state. For a binomial probability distribution, the likelihood function is defined as,

$$\mathcal{L}(p) = \prod_{i=1}^{m} \big(p\,\mathcal{P}(k_i|\downarrow) + (1-p)\,\mathcal{P}(k_i|\uparrow) \big). \tag{2.12}$$

Figure 2.22: Rabi oscillation of the motional insensitive Raman transitions. (a) and (b) Before and after the installation of the UV fibers and UV power servo, respectively.

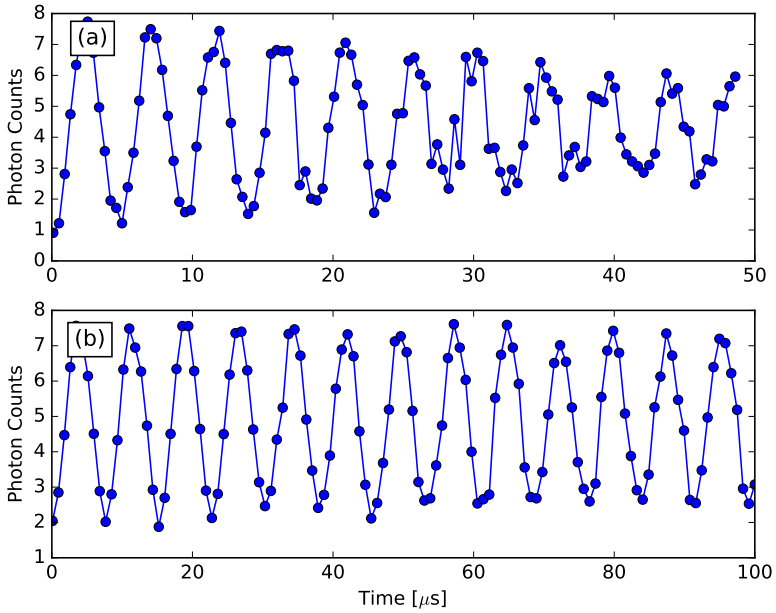

By maximizing the likelihood function numerically, we can estimate the population in $|\downarrow\rangle$ for any histogram observed in the experiments [Gaebler 16].

2.6.2 UV Fibers and Pulse Area Control

For clock operation, it is important to have long term stability in many components of the experiments. One important criterion of our system is to ensure the ion experiences the same pulse area at the right frequencies in each pulse sequence. To achieve this, we use fibers to minimize the laser beam pointing fluctuations [Colombe 14] and actively servo the pulse area by controlling the laser power after the fiber.

Nowadays fibers that are suitable for light sources at $280\,nm$ and $267\,nm$ are still not available in the market due to the formation of UV-induced color-center [Skuja 01]. However, using commercially available solid-core photonic crystal silica fibers after hydrogen loading and UV irradiation [Colombe 14], we can usually achieve $\sim$ 50% transmission through the fibers at both

$280\,nm$ and $267\,nm$. The recipe to make these fibers can be found on our group website[7] . The fiber attenuation at $267\,nm$ has not been systematically studied but it is believed to be close to the value at $280\,nm$ reported in Ref. [Colombe 14] based upon our experience. The fibers also spatially filter higher order transverse modes, typically seen at the output of BBO-based frequency doublers due to the large walk-off angle [Boyd 68], and hence reduce spatial intensity variations of laser fields at the position of ions. In general we have a few hundreds of μW to $2\,mW$ of UV power measured after the fibers. In Fig. 2.22, we show the Rabi oscillation curves of motion-insensitive Raman transition in $^{25}Mg^{+}$ before and after installing the UV fibers in our system.

Following each UV fiber output coupler, we set up a beam pick-off to monitor and control the laser power. The transmitted power through a fiber is actively maintained at a desired level by adjusting the rf power going to an AOM. This laser power servo is controlled by a high-speed digital controller [Leibrandt 15]. The high speed controller gives us the ability to control an individual pulse of duration $\gtrsim 1\,\mu s$ and the servo performance remains the same when the duty cycle of the pulse sequence changes. In addition, the use of fibers eliminates the pointing variations due to the thermal effects of the AOMs.

2.6.3 AOM Double-pass Configuration

AOMs are widely used in atomic physics experiments for frequency and timing control of laser pulses. In a double-pass configuration, the beam pointing becomes insensitive to the deflection angle of the AOM when a cat's eye retroreflector is implemented on the second pass [Snyder 75, Donley 05]. Moreover, by rotating the polarization of the second second pass by 90°, the retroreflected beam will follow the incident beam path and later can be separated from the input beam such that the beam pointing fluctuation caused by the thermal lensing effect of AOM will be canceled [Donley 05]. This technique is commonly used in the experiments which require a precision control of light intensity. However it is only possible when using the AOMs with significant deflection efficiency in two perpendicular polarization directions, which are not available in the UV.

[7] `http://www.nist.gov/pml/time-and-frequency-division/ion-storage`

Figure 2.23: The two-bounce (a) and three-bounce (b) double-pass AOM configurations. Path A (solid line): unperturbed beam path. Path B (dashed line): perturbed beam path due to the thermal effect of AOM.

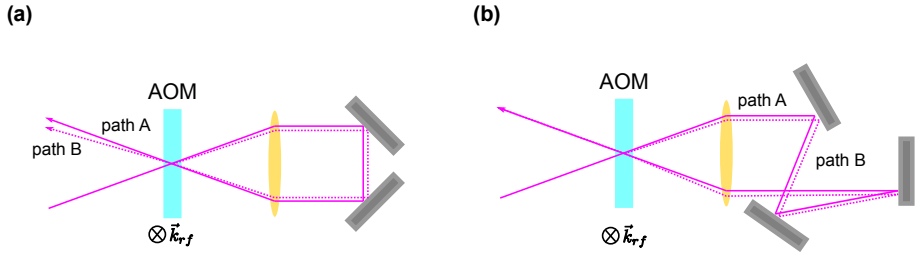

When using an UV AOM, the second pass needs to be deviated from the input beam by a small amount, which can be picked off for the experiments[8] . Therefore better thermal management is usually required to eliminate the beam pointing fluctuation [Kobayashi 06, Fröhlich 07].

In our system, we actually investigate a different route to reduce the thermal effect. In fact, the cancellation of the thermal effect in the double-pass setup relies on two factors.

- The second path passes through the same region of the AOM as the first one such that it experiences the same thermal lensing.
- The beam pointing change of the second path needs to be opposite to the first path in the lab frame.

These two conditions are achievable if there are odd numbers of mirror bounces after the AOM. In Fig. 2.23, we can see the three-bounce configuration cancels the thermal effect while the two-bounce configuration doubles the thermal drifts. In our setup, we did observe the reduction the beam pointing fluctuation by about a factor of 5 after changing from two-mirror to three mirror configuration. The drawback of this setup is that the Bragg condition cannot not be satisfied in both paths; however we can still achieve about 50 % deflecting efficiency after the second pass.

[8] Usually two beams are separated perpendicular to the deflecting direction.

2.7 Quantum Logic Spectroscopy

With the lack of direct fluorescence detection, we use a technique called quantum logic spectroscopy (QLS) to read out the atomic state of the $^{27}Al^+$ [Schmidt 05]. The basic idea is to use the secular motion as the information bus to transfer the atomic state information of the ion of interest, called the spectroscopy ion, to another ion of different species simultaneously trapped with the spectroscopy ion, called the logic ion. In the optical clock system described in this thesis, we trap a $^{25}Mg^+$ as the logic ion together with an $^{27}Al^+$. The out-of-phase mode of motion along the trap z axis is chosen to transfer the atomic state information. The information we need to know is if the $^{27}Al^+$ is in the $^1S_0$ state or not. The process is shown in Fig. 2.24 and described as follows.

(1) Ground state cooling on the $^{25}Mg^+$ to place the $^{25}Mg^+$-$^{27}Al^+$ two-ion pair axial COM and axial STR motional modes in their ground state. At this moment, we assume the $^{27}Al^+$ is in the $|^1S_0\rangle$ state.

(2) Prepare the $^{25}Mg^+$ in $|\downarrow\rangle$.

(3) Add one motional quantum to the STR mode by driving the blue sideband of the intercombination transition $|^{27}Al^+, {}^1S_0\, F = 5/2, m_F = \pm 5/2\rangle \rightarrow |^{27}Al^+, {}^3S_1\, F = 7/2, m_F = \pm 7/2\rangle$.

(4) Subtract one motional quantum by driving the red sideband of the $^{25}Mg^+$ transition $|\downarrow\rangle \rightarrow |\uparrow\rangle$.

(5) Detect $^{25}Mg^+$ atomic state by detecting the scattered photon count histogram from the transition $|\downarrow\rangle \leftrightarrow |^2P_{3/2},\, F = 4,\, m_F = -4\rangle$.

Because the $^{27}Al^+$ starts in the $|^1S_0\rangle$ state, the transitions in steps 3 and 4 succeed and the $^{25}Mg^+$ ends up in the $|\uparrow\rangle$. On the other hand, if the $^{27}Al^+$ does not start in the $|^1S_0\rangle$ state, steps 3 and 4 are inactive and the $^{25}Mg^+$ remains in the $|\downarrow\rangle$ state. Therefore by distinguishing the photon count histograms shown in Fig. 2.21, we can extract the initial atomic state of the $^{27}Al^+$.

Figure 2.24: Process of quantum logic spectroscopy. The atomic state of the $^{27}Al^{+}$ is determined by the scattered photon count histogram of the $^{25}Mg^{+}$. Left column, $^{27}Al^{+}$ not in the $^{1}S_0$ state; right column, $^{27}Al^{+}$ in the $^{1}S_0$ state.

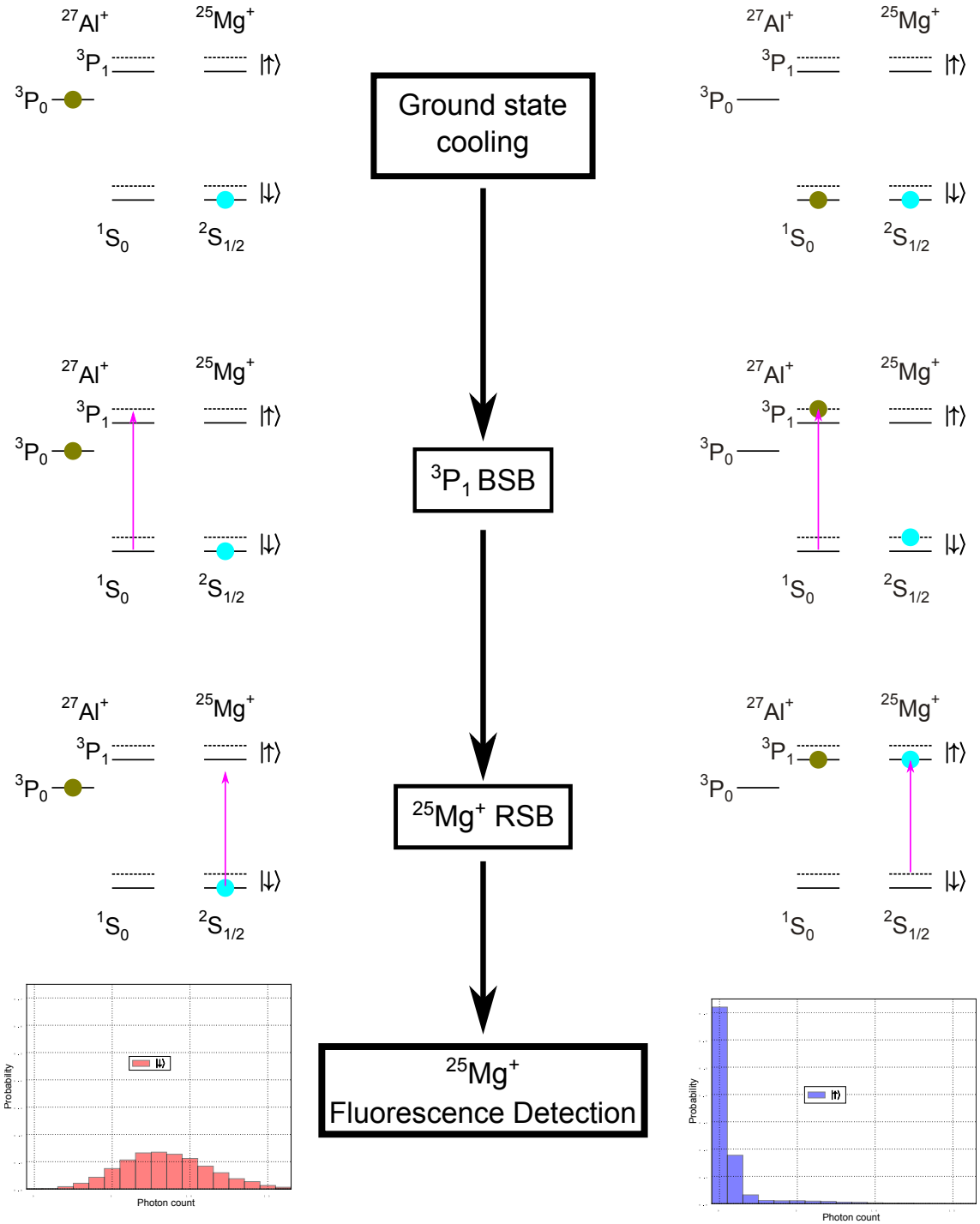

Table 2.2: Comparison of two different $^{27}Al^{+}$ optical clock operation protocols.

Clock operation protocol	$\mathscr{A}$ Doppler cooled clock	$\mathscr{B}$ Sideband cooled clock
Kinetic energy of the secular motion	Doppler limit	Ground state
Cooling light shift	Need to evaluate	–
Clock duty cycle	Higher	Lower
Overall clock shift	–	Potentially smaller

2.8 Clock Operation Pulse Sequence

Typically one optical clock operation sequence can be separated into three main parts: preparation, interrogation, and detection. We consider two different clock operation protocols, $\mathscr{A}$ and $\mathscr{B}$, proposed for the $^{27}Al^{+}$ optical clock operation. Their difference is the ions' kinetic energies during the interrogation period. The sequence $\mathscr{A}$, Doppler-cooled clock, maintains the ions at the Doppler limit temperature during the clock interrogation while the sequence $\mathscr{B}$, sideband-cooled clock, prepares the ions near the motional ground state at the beginning of the clock interrogation. The comparison between the two sequences is summarized in Table 2.2.

2.8.1 State Preparation

The preparation process includes the preparation for both the internal atomic states and the external motional states. Both of the protocols start with a 200 μs FD cooling pulse on the $^{25}Mg^{+}$ followed by a 2 ms Doppler cooling pulse to ensure the ion's motion is close to the Doppler limit. At the end of the preparation process, multiple $^{3}P_{1}$ pulses are applied to prepare the $^{27}Al^{+}$ in one of the stretched Zeeman levels of the ground state. For sequence $\mathscr{B}$, a ground state cooling pulse sequence is inserted after the Doppler cooling pulse to prepare the ions close to the ground state; this will be discussed in the next chapter. The pulse sequence of the state preparation process is presented in Fig. 2.25.

Figure 2.25: State preparation pulse sequences before the clock interrogation. FD, far-detuned cooling pulse; D, Doppler cooling pulse; Prep., $^3P_1$ state preparation pulse.

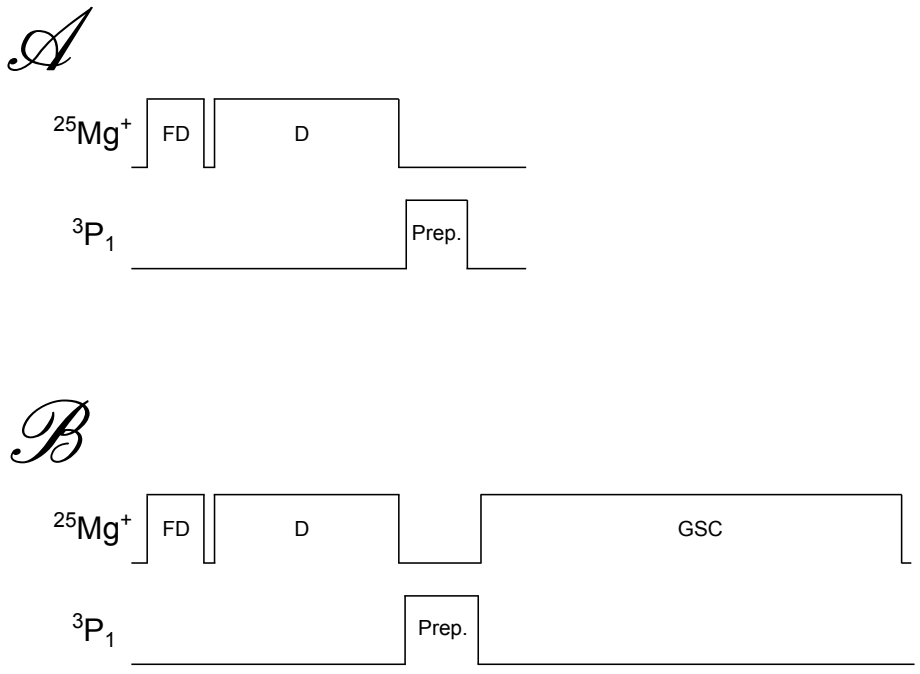

2.8.2 Clock Interrogation

When the state preparation is complete, we switch on the laser pulse to interrogate the clock transition of the $^{27}\mathrm{Al}^+$, $|^1S_0, F = 5/2, m_F = \pm 5/2\rangle \leftrightarrow |^3P_0, F = 5/2, m_F = \pm 5/2\rangle$. Rabi spectroscopy is used to determine the transition line center. For the sequence $\mathscr{A}$, the Doppler cooling light is turned on during the clock interrogation such that ions' kinetic energy is close to the Doppler cooling limit. in this case, the cooling light imparts an ac Stark shift to the clock transition, which needs to be characterized [Rosenband 08, Chou 10a]. On the other hand, the cooling is absent during the clock interrogation in the sequence $\mathscr{B}$ and the ions' kinetic energy increases due to the background heating [Turchette 00a]. Therefore, the characterization of the energy after sideband cooling and the background heating rate are necessary to determine the frequency shift due to time-dilation arising from the ions' energy [Chen 17]. Typically, a few tens to 200 ms interrogation time is used. The pulse sequence is depicted in Fig. 2.26.

Figure 2.26: Clock interrogation pulse. Clock, $^3P_0$ pulse; D, Doppler cooling pulse.

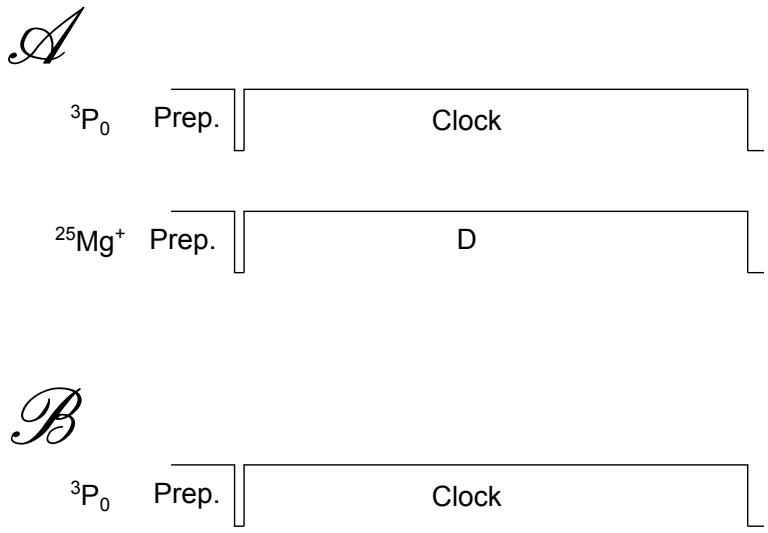

2.8.3 Atomic State Detection

The atomic state detection is achieved by utilizing quantum logic spectroscopy. After the interrogation pulse, the atomic state of $^{27}Al^+$ is determined from the resulting state of $^{25}Mg^+$ following Sec. 2.7. A quantum nondemolition measurement scheme is implemented to increase the detection fidelity by repeating the measurement sequence multiple times [Hume 07]. Adaptive selection of the number of repetitions using a Bayesian algorithm reduces the clock dead time and hence improves the stability [Quessada 03]. In general, $5 \sim 10$ repetitions of the quantum-logic spectroscopy sequence are needed to determine which state the $^{27}Al^+$ is in.

Chapter 3

Time Dilation Effect due to Secular Motion

Previously, the $^{27}Al^{+}$ optical clocks had achieved a fractional frequency uncertainty of 8.8×10^{-18} [Chou 10a]. One of the main uncertainties arose from the time dilation (second-order Doppler) shift due to secular motion while performing continuous sympathetic Doppler cooling on the $^{25}Mg^{+}$ ion during the clock interrogation[1] . The uncertainty was limited to 30% of the secular motion time dilation shift due to the difficulties of performing accurate temperature measurement of a $^{25}Mg^{+}$-$^{27}Al^{+}$ two-ion pair near the Doppler cooling limit. To date, trapped-ion optical clocks are all operated with the ions' secular motion near the Doppler cooling limit [Chou 10a, Barwood 14, Ludlow 15, Huntemann 16]. Although operating the clock with the motion cooled to near the zero-point energy had been mentioned almost three decades ago [Wineland 87], it has not been achieved due to the complexity of the cooling sequences and the challenge to determine the energies near the motional ground state. In this chapter, I will discuss how we overcome these difficulties to operate the clock near the 3D motional ground state and hence to reduce the secular motion time dilation shift and uncertainty.

3.1 Motion in RF Traps

The classical equations of motion of an ion inside a linear trap are given in Eq. (2.1) and Eq. (2.6). When the ion is cold, the ion's motion is quantized and can be described by a Fock state distribution for each of the secular modes of motion. The energy of a specific motional mode p is

[1] The first-order Doppler shift in the Al^{+} optical clock is strongly suppressed due to various reasons, which will be discussed in the next chapter.

Figure 3.1: Secular modes of motion of $^{25}Mg^{+}$-$^{27}Al^{+}$ ion pair.

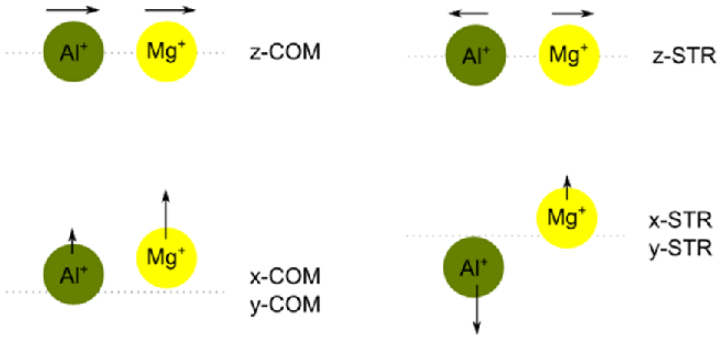

given by

$$E_p = \hbar\omega_p(\bar{n}_p + \frac{1}{2}), \tag{3.1}$$

where $\bar{n}_p$ is the average occupation number of the Fock state distribution. When one $^{25}Mg^{+}$ and one $^{27}Al^{+}$ are trapped simultaneously in a linear Paul trap, six independent secular modes of motion exist[2] . As shown in Fig. 3.1, there are two motional modes along each axis, the "common" (COM) mode where the velocities of two ions are in the same direction and the "stretch" (STR) mode where they are in the opposite directions. Therefore, if we can measure the average occupation number of all six modes of motion, we can determine the energy of the secular motion.

For a Paul trap, the pseudopotential generated by the rf field leads to an additional energy in the transverse directions which needs to be included when we characterize the energy of the ions. Because this motion has a characteristic frequency Ω_T and exists even in an ideal Paul trap, we usually call it "intrinsic micromotion" (IMM) to be distinguished from the excess micromotion (EMM) which arises from the imperfections of the ion-trapping potential. The energy of the IMM has been described in detail and it is approximately the same as the secular energy for a specific secular mode of pseudopotential motion [Wineland 87]. Therefore, the energy of the secular modes

[2] The effect of the mode-coupling due to the Kerr nonlinearity arising from the mutual Coulomb repulsion between ions is not essential and ignored here when the ions are cold [Marquet 03].

of motion and the IMM energy is given by

$$E = \sum_p \zeta_p \hbar\omega_p(\bar{n}_p + \frac{1}{2}), \tag{3.2}$$

where the factor ζ_p approximately equals 2 for the transverse motion, and 1 for the axial motion. The resulting time-dilation shift is given by

$$\frac{\delta f}{f} = -\frac{E}{m_{Al}\, c^2}. \tag{3.3}$$

3.2 Sideband Thermometry

The most common method to measure the secular motion energy of trapped ions in thermal equilibrium is to compare the transition probabilities between the first-order blue sideband (quanta-adding) and the first-order red sideband (quanta-subtracting) transitions [Diedrich 89, Monroe 95]. Given a thermal distribution with average occupation number $\bar{n}$, the probability $\mathcal{P}_{th}$ in a Fock state n is expressed as

$$\mathcal{P}_{th}(n) = \frac{1}{1+\bar{n}} \left(\frac{\bar{n}}{\bar{n}+1}\right)^n. \tag{3.4}$$

When we apply a pulse of duration t to drive the blue and red sideband transitions, the transition probabilities P_b and P_r are given by

$$P_b = \sum_{n=0}^{\infty} \frac{1}{2} \left[1 - \cos(2\Omega_{n,n+1}t)\right] \mathcal{P}(n), \tag{3.5}$$

$$P_r = \sum_{n=1}^{\infty} \frac{1}{2} \left[1 - \cos(2\Omega_{n,n-1}t)\right] \mathcal{P}(n), \tag{3.6}$$

where $\mathcal{P}(n)$ is the population in the motional state n, and $\Omega_{n,n\pm1}$ is the Rabi rate connecting the two Fock states, $|n\rangle$ and $|(n \pm 1)\rangle$. After substituting Eq. (3.4), the equations above become

$$\begin{aligned} P_b &= \left(\frac{\bar{n}+1}{\bar{n}}\right) \sum_{n=1}^{\infty} \frac{1}{2(\bar{n}+1)} \left[1 - \cos(2\Omega_{n,n-1}t)\right] \left(\frac{\bar{n}}{\bar{n}+1}\right)^n, \\ &= \left(\frac{\bar{n}+1}{\bar{n}}\right) P_r. \end{aligned} \tag{3.7}$$

Here we use $\Omega_{n,n+1} = \Omega_{n+1,n}$ in the derivation. Therefore, the average occupation number of a Fock state distribution in thermal equilibrium can be determined by measuring the ratio of probabilities

in the blue sideband and the red sideband transitions, $\beta \equiv P_b/P_r$, and is given by

$$\bar{n} = \frac{1}{\beta - 1}. \tag{3.8}$$

In fact a more general formula can be written as

$$\bar{n} = \frac{1}{\sqrt[\Delta]{\beta_\Delta} - 1}, \tag{3.9}$$

where β_Δ denotes the Δ-th order blue sideband and red sideband ratio. We only focus on the ratio of the first-order sideband ratio throughout this thesis. The derived average occupation number $\bar{n}$ and the measured sideband ratio are shown in Fig. 3.2.

Figure 3.2: The relation between $\bar{n}$ and the first-order sideband ratio for a thermal distribution.

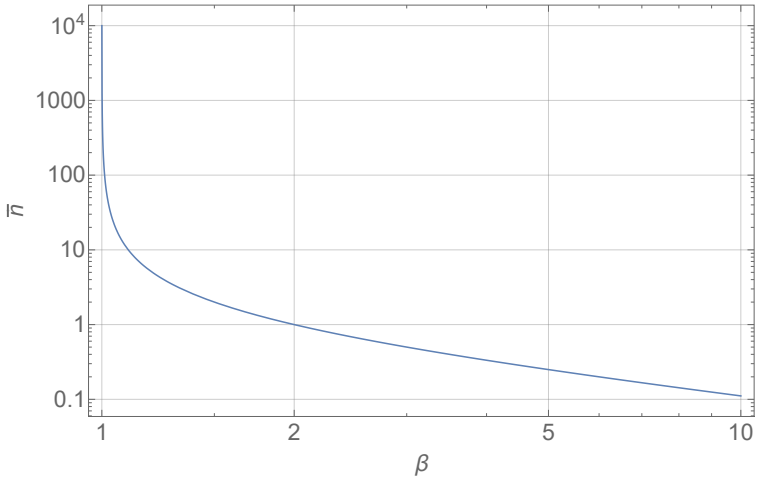

Although sideband thermometry provides a simple and robust method to measure the ion energy, we stress that the derivation above is only valid for the systems in thermal equilibrium. For a system possessing a non-thermal Fock state distribution, sideband thermometry may lead to a significant deviation from the actual ion energy [Chen 17]. Even for thermal equilibrium conditions, sideband thermometry may encounter certain practical challenges. For instance, when $\bar{n} \simeq 10$, it becomes very sensitive to a small change of the sideband ratio and hence the projection noise of the measurement in β limits the achievable accuracy. In the following two sections, I discuss specifically the determination of the secular motional energy close to and below the Doppler cooling limit in the case of the $^{25}Mg^{+}$-$^{27}Al^{+}$ two-ion pair.

3.3 Sympathetic Doppler Cooling and Energy Estimation

Sympathetic Doppler cooling of a $^{27}Al^+$ using a $^{25}Mg^+$ in a linear Paul trap has been investigated theoretically in Ref. [Wübbena 12] and I will just briefly summarize here. The cycling transition $|\downarrow\rangle \leftrightarrow |^2P_{1/2}, F = 4, m_F = -4\rangle$ with a 40 MHz linewidth is used to Doppler cool all six secular modes of motion. The laser frequency is set to be 20 MHz red-detuned from the transition and the intensity is controlled to be about 10% of the saturation intensity. Although the larger linewidth of $^{25}Mg^+$ leads to higher achievable cooling limit in comparison with other ion species such as Be^+, Ca^+, etc., the mass match between $^{27}Al^+$ and $^{25}Mg^+$ benefits the sympathetic cooling as shown in Fig. 3.3.

Figure 3.3: The sympathetic Doppler cooling limit of Al^+ versus the mass ratio of Al^+ and the coolant ion, adapted from Ref. [Wübbena 12]. The energy is in a unit of Doppler temperature of the coolant ion. The simulation is performed at different dimensionless heating rates S_E/S_{E0}.

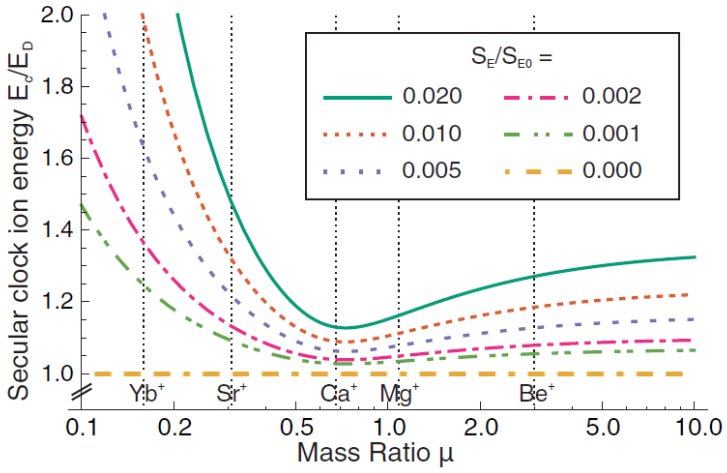

As shown in Fig. 2.8, the Doppler cooling beam has angles of about (60°, 60°, 45°) with respect to the axes of ions' motion (x, y, z), which provides sufficient projections to cool the motion in all three principal axes. If the Doppler cooling pulse is long enough such that the system reaches thermal equilibrium, the ions' energy can be determined using the sideband thermometry discussed in the previous section, which is the method used in the previous $^{27}Al^+$ clocks [Rosenband 08,

Chou 10a]. As an example, the energy determination given in Ref. [Chou 10a] is presented in Table 3.1. The measured energies deviate 15-20% from the theoretical estimation, which possibly arises from uncertainties of the angles between the Doppler cooling beam wavevector and the ions' motional directions, or the measurements of red(blue) sideband transition probabilities. Hence 30% of the total energy is conservatively given as the uncertainty of energy determination.

Table 3.1: The energy of six secular modes of motion in a $^{27}Al^{+}$-$^{25}Mg^{+}$ two ion pair after sympathetic Doppler laser cooling on the $^{25}Mg^{+}$. $\bar{n}_C$ and $\bar{n}_M$ are the calculated and the measured average occupation numbers, respectively. TD: time-dilation. The data are from Ref. [Chou 10a].

Mode	y-COM	y-STR	z-STR	x-COM	x-STR	z-COM
f [MHz]	6.53	5.66	5.20	4.64	3.41	3.00
$^{25}Mg^{+}$ amplitude [nm]	$4.9\hat{y}$	$2.9\hat{y}$	$4.6\hat{z}$	$5.5\hat{x}$	$-4.2\hat{x}$	$5.6\hat{z}$
$^{27}Al^{+}$ amplitude [nm]	$2.6\hat{y}$	$-5.0\hat{y}$	$-4.1\hat{z}$	$3.5\hat{x}$	$6.2\hat{x}$	$5.8\hat{z}$
$\bar{n}_M$	2.9	4.5	3.4	6.3	10.0	7.0
$\bar{n}_C$	3.3	3.8	3.4	5.9	8.0	5.9
TD/quantum [10^{-18}]	0.226	0.731	0.197	0.290	0.771	0.133
Total TD [10^{-18}]	0.77	3.66	0.77	1.97	8.41	1.00

Instead of using a direct comparison of the red and the blue sideband ratio to extract the ions' energy, here we explore another strategy to estimate the energy close to the Doppler limit temperature. The Rabi rate $\Omega^{(p)}_{n,n'}$ between two Fock states n and n' of a secular mode p is given by [Wineland 98]

$$\begin{aligned}\Omega^{(p)}_{n,n'} &\equiv \Omega \left| \langle n | e^{i\eta_p (a+a^\dagger)} | n' \rangle \right| \\ &= \Omega\, e^{-\frac{\eta_p^2}{2}} \sqrt{\frac{n_<!}{n_>!}} \eta_p^{|n-n'|} \mathcal{L}^{|n-n'|}_{n_<}\left(\eta_p^2\right)\end{aligned} \tag{3.10}$$

where Ω is the Rabi rate between two electronic states and $\eta_p \equiv kz_0$ is the Lamb-Dicke parameter, which can be interpreted as the ratio between the motional ground state wavefunction spread and the wavelength of the laser field. The lesser and greater of n and n' are represented as $n_<$ and $n_>$, respectively, while $\mathcal{L}^{\alpha}_{n}$ is the generalized Laguerre polynomial given by

$$\mathcal{L}^{\alpha}_{n}(x) = \sum_{m=0}^{n} (-1)^m \binom{n+\alpha}{n-m} \frac{x^m}{m!}. \tag{3.11}$$

Therefore, each observed Rabi oscillation curve is a superposition of oscillations of infinite numbers

of Fock states with different oscillation frequencies. Hence the population $P_\uparrow$ starting from $|\downarrow\rangle$ after a pulse with a duration t can be modeled as

$$P_\uparrow^{(\Delta n)}(t) = \sum_n^\infty \frac{1}{2}\left(1 - e^{-\gamma t}\cos(2\Omega_{n,n+\Delta n}\, t)\right) P_{th}(n), \tag{3.12}$$

where $P_{th}(n)$ denotes the population in a Fock state $|n\rangle$ in thermal equilibrium given in Eq. (3.4), γ is a decoherence rate, and Δn is the change of motional quanta. In Fig. 3.4, I show a simultaneous fit to the carrier, RSB, and BSB Rabi oscillations of the z mode for a single trapped $^{25}Mg^+$ with a given Lamb-Dicke parameter from an independent calibration experiment[3] . In general the fitting gives a 5-10% uncertainty of the average occupation number, $\bar{n}$, at a 63% confidence interval. This sounds promising; however, the situation changes when there is more than one ion inside the trap. When the wavevector of the laser field has projections on multiple modes of motion, the observed Rabi rate of a transition of the motional mode p, ${}^{(DW)}\Omega_{n,n'}^{(p)}$, perturbed by the Debye-Waller effect is given by [Wineland 98]

$$\begin{aligned} {}^{(DW)}\Omega_{n,n'}^{(p)} &= \Omega_{n,n'}^{(p)} \left| \sum_{n_{h\neq p}=0}^{\infty} \langle n^{(h)}| \prod_{h\neq p} e^{i\eta_p(a_h + a_h^\dagger)} |n^{(h)}\rangle \right|, \\ &= \Omega_{n,n'}^{(p)} \prod_{h\neq p} e^{-\frac{\eta_h^2}{2}} \mathcal{L}_{n_h}\left(\eta_h^2\right). \end{aligned} \tag{3.13}$$

Here h denotes other motional modes with a non-zero projection along the laser wavevector k. Therefore Rabi oscillation curves of a motional mode p close to the Doppler cooling limit of $^{25}Mg^+$ actually depend on the energies in other modes of motion h. This leads to a difficult determination of the motional energy due to the large numbers of parameters in the fit model. Moreover, the systematic and statistical error of the experimentally determined Lamb-Dicke parameter leads to an additional uncertainty of about 10 % of the determined energy[4] . Including all these factors, we estimate that we could achieve an energy uncertainty equal to 20% of the total energy. As a result, the time dilation shift uncertainty due to the secular motion is not significantly reduced in

[3] The Lamb-Dicke parameter is experimentally determined by measuring the Rabi rate ratio between the carrier and BSB transitions after ground state cooling.

[4] There are many factors that may contribute this. For example, an ac Stark shift due to certain leakage may light shifts the transition center and contributes to an error of the Lamb-Dicke parameter.

comparison with the values we reported previously in Ref. [Chou 10a]. We need a new method to reduce this uncertainty further, which will be described in the next section.

Figure 3.4: Thermal distribution fit to Rabi oscillations of the z mode of motion for a single trapped $^{25}Mg^{+}$. Black dots are fitting residuals.

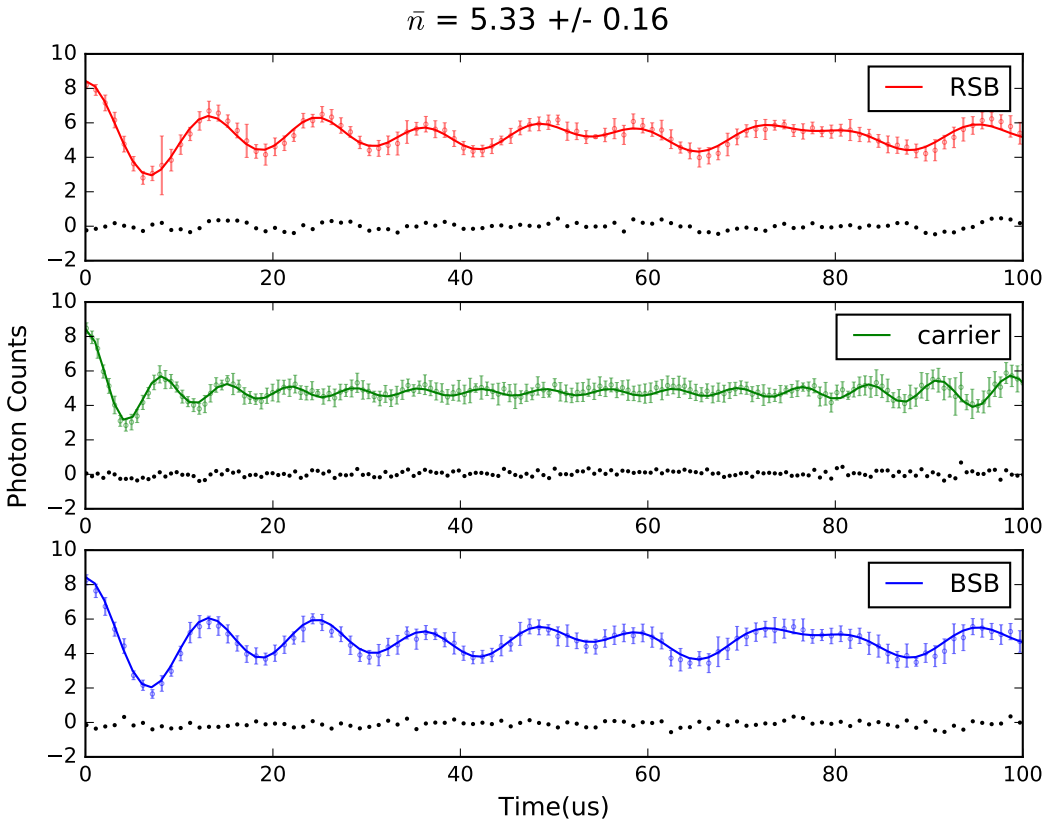

3.4 Sympathetic Sideband Cooling and Energy Estimation

In the previous section, we see the difficulties of characterizing the ions' energy to our desired accuracy at the Doppler cooling limit. A naive and straightforward thought is obvious,

How about cooling the ions below the Doppler cooling limit to reduce both the frequency shift and the uncertainty due to the time dilation of secular motion?

With the development of various cooling techniques [Diedrich 89, Monroe 95, Roos 00, Barrett 03,

Poulsen 12a, Poulsen 12b, Manfredi 12, Lin 13, Ejtemaee 16], operating an ion trap system below the Doppler cooling limit, or even close to the motional ground state, is possible. However, operating the $^{27}Al^{+}$ optical clock near the motional ground state requires more than the routine procedures used in other ion trap experiments.

The optical clock application requires all the motional modes to be cooled to the ground state instead of just a few of them, which implies a more complicated experimental design. Because the time dilation shift arises from the second order Doppler effect, which is proportional to the total energy of ions, it will not help much by simply cooling a few motional modes. In our case, six secular modes of motion need to be addressed. This requirement suggests that adiabatic cooling is not favorable [Poulsen 12b, Manfredi 12], because it requires adiabatic changes of the pseudopotential. Frequent changes of the pseudopotential are not only technically challenging and time-consuming but likely to lead to the electric noise and thermal instability of rf resonator. Sisyphus laser cooling, which has been demonstrated to cool Yb^{+} to near the motional ground state [Ejtemaee 16], will not work because our choice of the coolant ion $^{25}Mg^{+}$ does not have a suitable atomic structure in the low magnetic field regime. The lack of a suitable atomic structure is also problematic for electromagnetically-induced-transparency (EIT) laser cooling. Furthermore, EIT laser cooling in three dimensions is not fully understood and certain problems need to be solved [Lechner 16]. Moreover, characterizing the ions' energy at a desired accuracy, which requires a full understanding of the cooling dynamics, is always a challenge no matter which cooling technique is chosen. Therefore we have decided to use Raman sideband cooling to cool the $^{27}Al^{+}$-$^{25}Mg^{+}$ two-ion pair because it is widely used to cool $^{25}Mg^{+}$ close to the motional ground state in our group and does not have the problems that adiabatic cooling has. Moreover, the Raman sideband cooling has already been implemented for the axial secular modes of motion for QLS.

As shown in Fig. 2.8, we employ two sets of Raman beams to cool secular motions along the (x, y, z) directions efficiently. After a pulse addressing the RSB transition $|\downarrow, n_p\rangle \rightarrow |\downarrow, n_p - \Delta n_p\rangle$, Δn_p motional quanta are ideally removed from the ions' motional mode p. Using sideband thermometry to determine the ions' energy after sideband cooling encounters two main difficulties.

(1) The RSB transition probability almost vanishes.

(2) The outcome of the sideband cooling will not result in a thermal Fock state distribution.

While the first point may be overcome by increasing the data acquisition time, the second point reduces in the validity of sideband thermometry [Barrett 03]. Hence we need another method to estimate the energy after sideband cooling.

3.4.1 Numerical Model

To further understand the sideband cooling process, we developed a numerical model to simulate the dynamics of the Fock state distribution during sideband cooling. The cooling is modeled by a coherent RSB transition probability [Wineland 98], which is given by

$$P_{\uparrow,n}(t) = \frac{1}{2}\left[1 - e^{-\gamma t}\cos\left(2\Omega_{n,n+\Delta n}t\right)\right] P_{\downarrow,n+\Delta n}(0), \tag{3.14}$$

where Δn is the order of the RSB pulse, $\Omega_{n,n+\Delta n}$ is the Rabi rate for the transition $|\downarrow, n+\Delta n\rangle \leftrightarrow |\uparrow, n\rangle$ given in Eq. (3.13), γ is a decoherence rate, and t is the pulse duration. The heating can be described as an incoherent diffusion process and has an analytical form [Turchette 00b]. Following Eq. (9) in Ref. [Turchette 00b], we can write down the population P'_n in a Fock state n after heating by Δn as

$$\begin{aligned} P'_n =& \frac{1}{1+\Delta n}\sum_{j=max\{0,n-m\}}^{n}\left(\frac{\Delta n}{1+\Delta n}\right)^{j}\quad\frac{1}{1+\Delta n}\sqrt{1-\frac{\Delta n}{\bar{n}_a}}\right)^{2n-2j} \\ &\times\left(1-\frac{\bar{n}_a-\Delta n}{\bar{n}_a(1-\Delta n)}\right)^{m-n+j}\left(\binom{m}{n-j}\binom{n}{j}P_m. \end{aligned} \tag{3.15}$$

Here P_m denotes the population in a Fock state m before the heating, and $\bar{n}_a$ represents the average occupation number of the thermal reservoir, which is of the order of 10^4-10^5 quanta at room temperature. The net energy gained during the heating, Δn, is given by

$$\Delta n = \sum_{n=0}^{\infty}\left(nP'_n - \sum_{m=0}^{\infty}\left(mP_m.\right.\right. \tag{3.16}$$

In the simulation, we treat a RSB cooling pulse as a single time step. Each step consists of processes as follows. At the beginning, a Δ_{p_n}-th order RSB cooling pulse with a duration t is

applied to a motional mode p. The population in $|\uparrow\rangle$ after the pulse is given by

$$P_{\uparrow}(t) = \sum_{n_p=0}^{\infty} P_{\uparrow,n_p}(t), \tag{3.17}$$

$$= \sum_{n_p=0}^{\infty} \frac{1}{2}\left[1 - e^{-\gamma t}\cos\left(2\Omega_{n_p,n_p+\Delta_{p_n}} t\right)\right] P_{\downarrow,n_p+\Delta_{p_n}}(0). \tag{3.18}$$

This equation does not include any heating and we need to deal with the heating during the RSB pulse. This is achieved by using Eq. (3.15) to calculate the effects of heating of the population $P_{\uparrow}(t)$ and $P_{\downarrow}(t) = 1 - P_{\uparrow}(t)$, respectively. In the next step, an ideal repumping process after a RSB cooling pulse perfectly pumps all the population to $|\downarrow\rangle$. At this moment, we have $P_{\uparrow} = 0$ and $P_{\downarrow} = 1$. Finally, we apply a heating to all the population before the next RSB cooling pulse to account for heating mechanisms independent of atomic states. As a result, if we have enough understanding of the heating mechanisms during the cooling and include them in our model, the numerical simulation will give us an estimate of the energy.

3.4.2 Heating Mechanisms

During the sideband cooling, various heating mechanisms are involved. In general, there are three different categories of heating.

(1) Heating due to the recoil from both the RSB cooling pulses and the repumping pulses.

(2) Heating due to a coherent process from $|\uparrow, n\rangle$ to the $|\downarrow, (n+1)\rangle$ driven by the RSB cooling pulses.

(3) Heating due to the background electric field noise.

The first heating mechanism is due to the incoherent scattering of the photons. The effects of the recoil can be estimated theoretically [Itano 82, Wineland 87, Ozeri 07]. Given the resonant Rabi frequency Ω_0 and the detuning from the transition frequency δ, the energy gained for a specific motional mode due to the recoil per pulse can be formulated as

$$\Delta E_{rol} = P(\Omega_0, \delta) \times \frac{\hbar^2 k_0^2}{2m}(f_i + f_f), \tag{3.19}$$

where f_i and f_f are the projections of the unit vector of the absorption and the emission photon momenta along the direction of the motional mode, and k_0 is the momentum of the laser beam; $P(\Omega_0, \delta)$ is the transition probability, which is approximately given by

$$P(\Omega_0, \delta) \simeq \frac{4\Omega_0^2}{\sqrt{4\Omega_0^2 + \delta^2}}. \tag{3.20}$$

Eq. (3.19) and Eq. (3.20) can be used to estimate the amount of the heating during the repumping sequences. Note that the recoil energy in Eq. 3.19 will be distributed among secular modes of motion and the change of the motional quanta of each mode is propotional to the square of its Lamb-Dicke parameter, η^2. The probability to scatter a photon during a Raman transition π pulse for $^{25}Mg^+$ has been theoretically studied and is given by [Ozeri 07]

$$P = \left(\frac{\pi\gamma}{\omega_f}\right)\left(\frac{2\delta^2 + (\delta - \omega_f)^2}{|\delta(\delta - \omega_f)|}\right), \tag{3.21}$$

where ω_f is the angular frequency between two fine structure levels, $^2P_{1/2}$ and $^2P_{3/2}$, and γ is the natural linewidth of the excited states. In fact, the scattering probability in Eq. (3.21) can be decomposed into two different mechanisms. The first is the Raman scattering, in which a change of the atomic state occurs, while the second is the Rayleigh scattering, which is simply the elastic scattering. The scattering rates are given by

$$P_{Raman} = \left(\frac{2\pi\gamma}{3}\right)\left(\frac{\omega_f}{|\delta(\delta - \omega_f)|}\right), \tag{3.22}$$

$$P_{Rayleigh} = \left(\frac{\pi\gamma}{\omega_f}\right)\frac{2\delta^2 - 2\delta\omega_f + \omega_f^2/3}{|\delta(\delta - \omega_f)|}. \tag{3.23}$$

Experimentally the Raman scattering rate can be determined by measuring the transition probability of $|\downarrow\rangle \leftrightarrow |\uparrow\rangle$ due to the Raman lasers. However, the Rayleigh scattering rate is difficult to measure directly. In our experiment, we have $(\delta/\omega_f) \sim 0.02 \ll 1$ such that the Rayleigh scattering rate is approximately 50% of the Raman scattering rate. For our experimental conditions, the Raman scattering rate is calculated and experimentally confirmed to be $< 10^{-4}$ quanta/μs for each motional mode. Importantly both the Raman and the Rayleigh scattering rate are independent of the frequency differences between the two Raman beams and all motional modes will heat each

time the Raman beams are applied to the ions. For this reason, although the heating rates due to the Raman and Rayleigh scatterings are small, these two mechanisms contribute significantly to the ions' final energy.

For the repumping sequences, the recoil heating is determined experimentally using sideband thermometry by preparing the $^{25}Mg^{+}$ in the motional ground state of $|\downarrow\rangle$ and then repeatedly applying a pulse sequence consisting of a carrier pulse followed by a repumping sequence. This heating mechanism scales with η^2 and is about 0.054 quanta per cycle for $\omega_z \simeq 2\pi \times 2.8$ MHz with a single $^{25}Mg^{+}$ in the trap. Although this value is relatively large, the effective heating due to repumping needs to be multiplied by the amount of population not in the motional ground state, which becomes negligible at the end of the sideband cooling process. The comparison between the experimentally measured values and the theoretical estimates of the repump heating rate is shown in Fig. 3.5.

Figure 3.5: Heating due to a repumping sequence in a $^{25}Mg^{+}$-$^{27}Al^{+}$ two-ion pair. Blue circle: measured values from a two-ion pair; magenta square: estimated value using the measured heating rate of a single $^{25}Mg^{+}$; olive diamond: theoretical calculation. The measurements are performed at the drive frequency $\Omega_T \simeq 2\pi \times 76$ MHz.

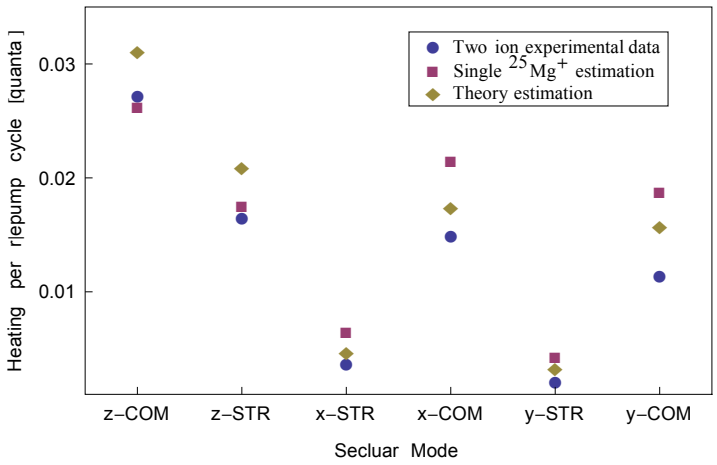

The second category of heating is due to a coherent process, illustrated in Fig. 3.6. If the $^{25}Mg^{+}$ is pumped to the $|\uparrow\rangle$ state either coherently or incoherently while a RSB cooling pulse is being applied, the cooling pulse will coherently add quanta to ions' motion. One of the channels

to the $|\uparrow\rangle$ state results from the off-resonant coupling to the carrier transition when a RSB cooling pulse is applied, which has been discussed in Ref. [Monroe 95]. When an ion is in the motional ground state, the probability of motional excitation due to this heating channel scales as $1/\omega^2$, where ω is the secular mode frequency. The off-resonant transition probability can be reduced by using either shaped pulses or longer pulse duration. Another channel to the $|\uparrow\rangle$ state arises from spontaneous emission from the Raman intermediate states. This process is absent when using the optical transitions for sideband cooling, such as Ca^+ and Yb^+. The motional excitation probability due to this channel depends on the cooling pulse duration and the frequency detuning of the Raman beams, and scales as $1/\eta$. In general, this heating channel can be reduced by increasing the Raman laser detuning. One important thing is that mechanism (2) only heats the motional mode which the cooling pulse is applied to and has very little effect on the other modes.

Figure 3.6: Illustration of a heating mechanism involving a coherent process. A RSB pulse removes a motional quanta coherently for the initial state $|\downarrow\rangle$, but adds a quanta for the initial state $|\uparrow\rangle$. Therefore, population in the $|\uparrow\rangle$ state during the RSB cooling pulses, either due to the off-resonant coupling to the carrier transition (green dashed arrow) or due to incoherent spontaneous emission from the excited states (blue dashed arrow), results in heating.

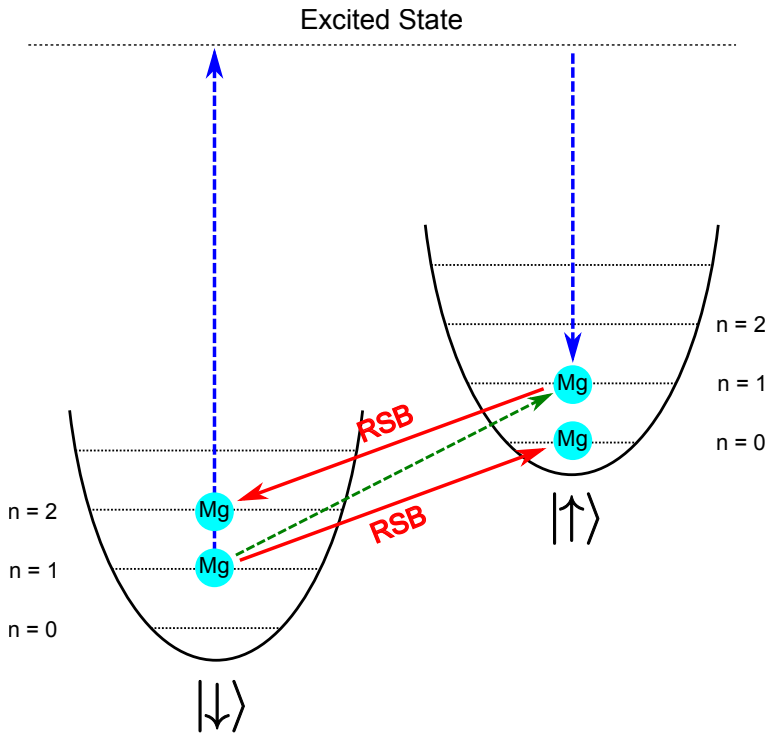

Modeling the heating due to mechanism (2) is not an easy task. From Eq. (3.13), we note that the amount of heating depends on the actual Fock state distribution when a cooling pulse is applied. Since we are primarily interested in the final energy after sideband cooling where $\bar{n}$ is small for each mode, we use the value of the motional excitation rate from $|\downarrow, n = 0\rangle$ when a first-order RSB is applied as the heating for each RSB cooling pulse to simplify our model. This value is obtained by numerically solving the optical Bloch equation and only including states $|\downarrow, n = 0\rangle$, $|\downarrow, n = 1\rangle$, and $|\uparrow, n = 0\rangle$ [Johansson 12, Johansson 13]. As an example, the results of the optical Bloch equation simulation are depicted in Fig. 3.7 and Fig. 3.8 for one of our experimental conditions. This simplification will affect the simulated sideband cooling time constant but not the simulated cooling limit, so it is appropriate when the number of cooling pulses is sufficient such that the population in the motional ground state dominates after sideband cooling.

The third mechanism is the heating due to electric field noise at the frequencies of motional modes, which results from the trapping fields, called "technical noise", or fluctuating potentials on the electrode surfaces. To reduce the technical noise, two 5-MHz-bandwidth band-pass filters are installed in series before the rf resonator to provide noise reduction in addition to the frequency filtering due to the rf resonator. The rf resonator is shielded by a copper tube, which is mechanically and electrically connected to the chamber to ensure a stable ground level. Although there is no low-pass filter built inside the vacuum chamber for the dc electrodes, each dc electric line passes through at least one $\sim$ 10 kHz low-pass filter before connecting to the vacuum feedthrough. Although we do not claim that the technical noise is eliminated completely in our system, we think we have reduced it significantly. The heating due to the fluctuating surface potentials is usually called anomalous heating and its physical origin is still not known. Many theories were proposed to try to explain the experimental observations [Gesley 85, Daniilidis 11, Safavi-Naini 11]. To date the previous experimental data suggest that the anomalous heating depends highly on the materials and the surfaces of the electrode [Hite 12, Kim 17] and decreases dramatically with increasing ion-to-electrode distance [Turchette 00a]. Choosing 250-μm ion-to-electrode distance is a compromise between the anomalous heating and the required rf power for the desired transverse

Figure 3.7: Simulation of the motional excitation due to the off-resonant carrier transition followed by a first-order RSB cooling pulse. The trap drive frequency is $\Omega_T \simeq 2\pi \times 40$ MHz. The red, green, and blue lines denote the population in vibrational levels of the $^{25}Mg^+$ hyperfine ground states $|\downarrow, n=0\rangle$, $|\uparrow, n=0\rangle$, and $|\downarrow, n=1\rangle$, respectively. The x axis is normalized to the π time of RSB transitions $|\downarrow, n=1\rangle \leftrightarrow |\uparrow, n=0\rangle$.

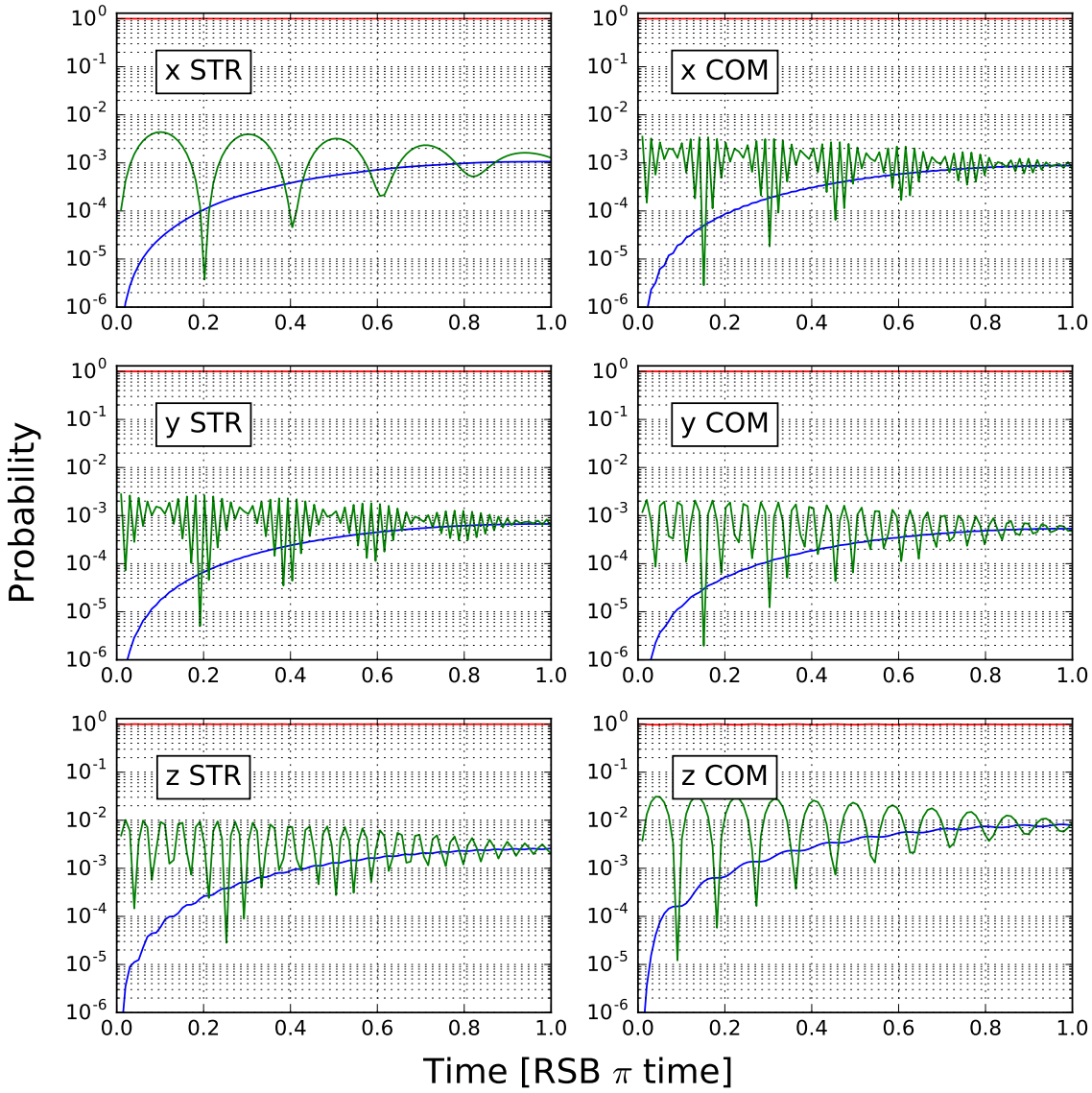

Figure 3.8: Simulation of the motional excitation due to the spontaneous emission from the Raman intermediate states followed by a first-order RSB cooling pulse. The trap drive frequency is $\Omega_T \simeq 2\pi \times 76$ MHz. The red, green, and blue lines denote the population in vibrational levels of the $^{25}Mg^+$ hyperfine ground states $|\downarrow, n=0\rangle$, $|\uparrow, n=0\rangle$, and $|\downarrow, n=1\rangle$, respectively. The x axis is normalized to the π time of RSB transitions $|\downarrow, n=1\rangle \leftrightarrow |\uparrow, n=0\rangle$.

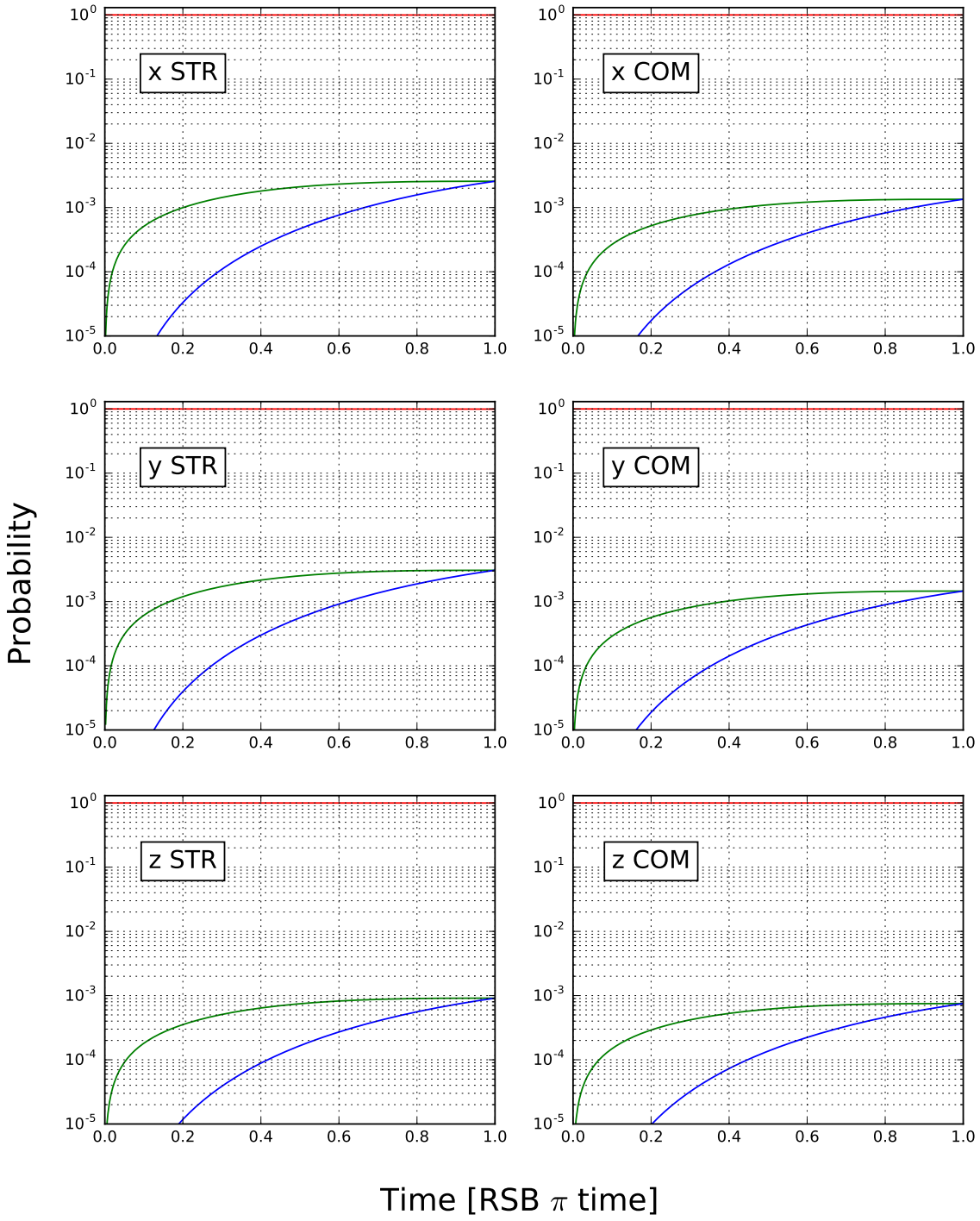

confinement, while using sputtered gold as the electrode surface is based upon previous experiences and literature [Brownnutt 15]. Experimentally, we cannot distinguish the breakdown of the electric field noise between technical noise and patch field noise. What we can measure is the contribution from all types of ambient electric field noise at the frequencies of the secular modes of motion.

To measure the heating rate of ions' motion due to electric field noise, we first prepare the ions close to the motional ground state. Depending on the value of the heating rate, ions then experience 10 to 30 ms of "dark time" without any cooling, such that the ions' motion can heat due to the ambient electric field. After the dark time, we measure the average occupation number of the ions in a specific motional mode and hence the heating rate utilizing sideband thermometry. Sideband thermometry is suitable for measuring the heating rate because the ambient heating rapidly drives the Fock state distribution towards thermal equilibrium [James 98, Dodonov 00].

3.4.3 Summary

With the amount of heating due to various mechanisms from either theoretical estimation or experimental determination, we can start to model the evolution of the Fock state distribution during the sideband cooling process. We assume the ion is initially in the $|\downarrow\rangle$ state and that the ions' motion is in a thermal distribution at the Doppler cooling limit, with a 20-30% energy uncertainty. After a RSB cooling pulse, part of the population will end up in the $|\uparrow\rangle$ state given by Eq. (3.14). During the pulse, ions will heat primarily due to mechanism (2) in Sec. 3.4.2, which only affects the Fock state distribution of the motional mode that the Raman sideband cooling pulse addresses. After the cooling pulse, the population in the $|\uparrow\rangle$ state will be repumped back to the $|\downarrow\rangle$ state and experience recoil heating due to the repumping pulse sequence. After a repumping sequence, the ion is in the $|\downarrow\rangle$ state. The heating from both the scattering of the Raman and Rayleigh processes, and the electric field noise is then calculated based upon the illumination time of the Raman laser pulses, and the total time spent during the cooling and the repumping sequence, respectively. After a cooling pulse, the Rabi rates are re-calculated using Eq. (3.13) based upon the real-time Fock state distribution to account for the Debye-Waller effect. In the simulation, we can trace the Fock

state distribution evolution throughout the sideband cooling pulse sequences. In addition, we can use the numerical model to predict the performance of different pulse sequences to design a pulse sequence based on speed and final temperature goals.

Although we want to include all the important physics in our numerical model to represent what happens to the ions' motion, there are still several assumptions and minor effects neglected in the model.

- All the pulses in the cooling and the repumping sequences are perfectly on resonance and applied to the ions for exactly the duration specified.
- The heating mechanism (2) in Sec. 3.4.2 is independent of the Fock states.
- The heating due to the scattering of the $|\downarrow\rangle$ state in a repumping sequence is negligible.
- The sideband cooling starts from the theoretical Doppler cooling limit.
- The Fock state distribution truncates at a finite number, usually between 150 and 200. The population above this state is assumed to be negligible and excluded from the simulation.
- The $^{25}Mg^{+}$ ion stays within the space spanned by $|\downarrow\rangle$, $|\uparrow\rangle$, and $|F = 3, m_F = -2\rangle$ during the cooling process and there is no population leakage to any other energy levels.
- Higher order off-resonant transition probability, which scales as η^2/ω^2, is not considered.
- Cross-mode coupling is assumed to be small and not considered.

For our experiments, these assumptions have been verified either theoretically or experimentally to ensure they are valid. For other experimental conditions, some of them may need to be re-considered and included in the simulation. The model is validated by comparing it with experimental data at intermediate times during the cooling sequences. The results are presented in Fig. 3.9 and show nice agreement between the model and the data.

Figure 3.9: Rabi oscillations of the first RSB (red, circle), the first BSB (blue, down triangle), and carrier (green, up triangle) Raman transitions of the z mode for a single $^{25}Mg^{+}$ after different numbers of pulses in the sideband cooling sequence at $\simeq$ 76 MHz drive frequency. Carrier Rabi oscillation curves are shifted by -0.5 for visibility. The cooling sequence consists of 17 second order RSB pulses followed by 8 first order RSB pulses to prepare the ion near the motional ground state. Hence only second order RSB pulses are applied in the first four panels. Solid lines are given by the numerical simulation without any free parameters. The simulated population evolution of the first ten Fock states during the cooling process is shown in the insets. There are 150 Fock states included in the simulation.

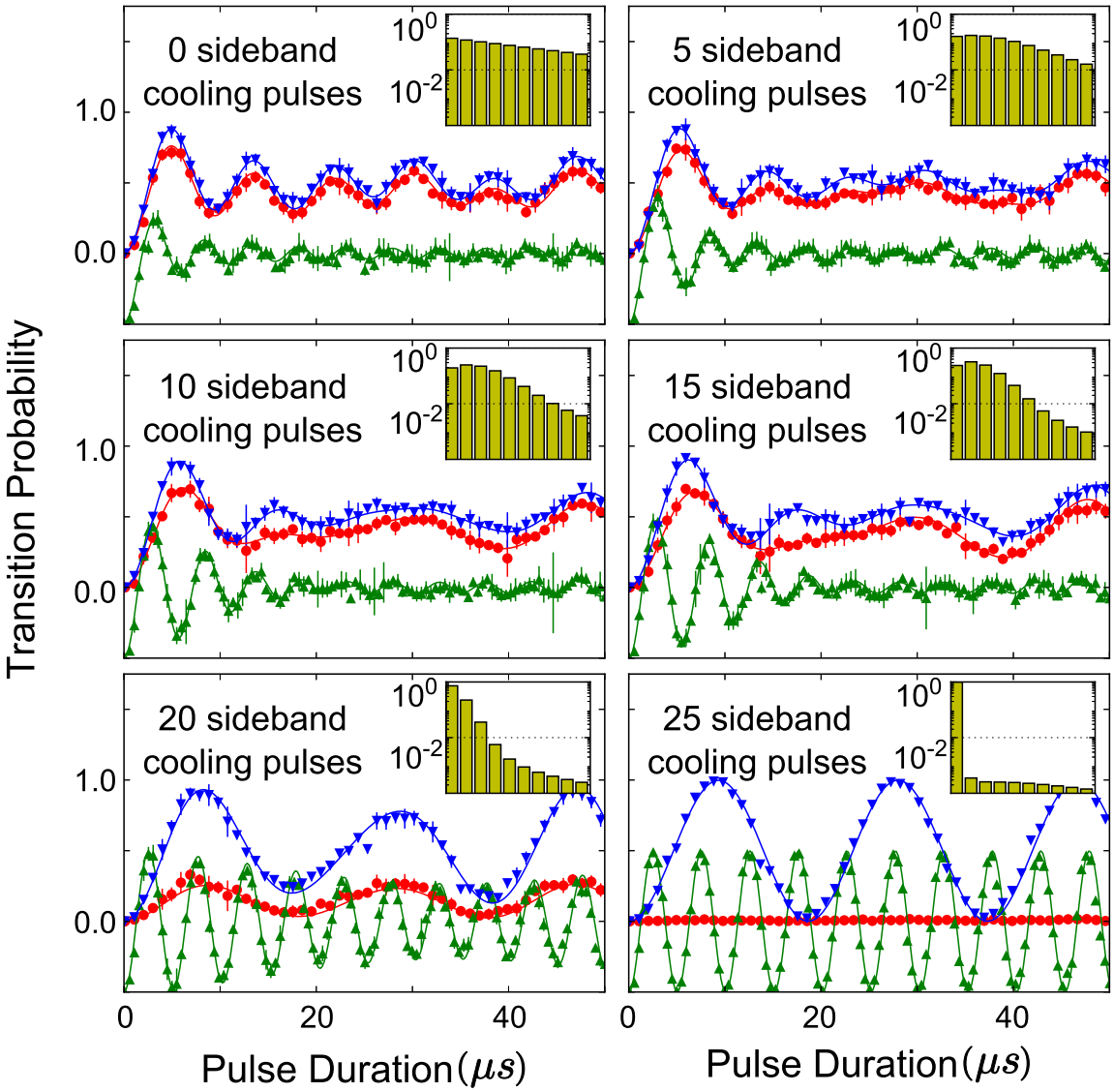

3.5 Cooling Pulse Optimization

Having a complete description of the sideband cooling not only helps characterize the motional energy but benefits the design of an efficient cooling pulse sequence. In Eq. (3.10), we note that the motional sideband Rabi rate depends on the Lamb-Dicke parameter η and the Fock state n. For example, the sideband Rabi rates of $\eta = 0.27$ are depicted in Fig. 3.10. We can see that the first-order RSB Rabi rate almost vanishes when $n \simeq 50$, which indicates that using only first-order RSB cooling pulses is neither efficient nor practical to cool the population above $n \simeq 50$ to the motional ground state [Wan 15]. Therefore, a sideband cooling pulse sequence utilizing higher-order RSB cooling pulses must be used in order to cool the population in higher Fock states. Another important thing we can see in Fig. 3.10 is that the Rabi rate of the first-order RSB transition is larger than those of the higher order RSB transitions when n is close to zero. This indicates that the first-order RSB pulses are always more efficient when the ions' motion is close to the motional ground state.

Figure 3.10: Motional sideband transition Rabi rates $\Omega_{n,n-\Delta n}$ in units of the carrier transition Rabi rate when $\eta = 0.27$.

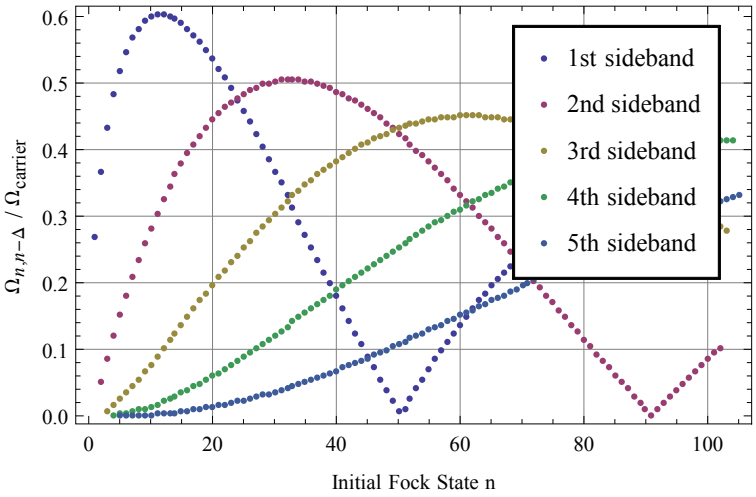

In this section, I will describe two different optimization approaches to design an efficient sideband cooling pulse sequence based upon our model. The first sequence was used when we

Table 3.2: Parameters of a $^{25}Mg^{+}$-$^{27}Al^{+}$ two-ion pair at 76 MHz drive frequency.

	x-COM	x-STR	y-COM	y-STR	z-COM	z-STR
Frequency (MHz)	6.2	5.4	7.2	6.5	2.7	4.8
Lamb-Dicke parameter ($^{25}Mg^{+}$)	0.12	0.06	0.11	0.05	0.18	0.16
Time-dilation shift per quantum (10^{-18})	−0.21	−0.85	−0.18	−0.86	−0.12	−0.18
Occupation number from simulation (quanta)	0.009 9	0.009 0	0.007 8	0.004 9	0.015	0.003 5
Occupation number from single-thermal distribution fit (quanta)	0.008 7	0.005 9	0.009 9	0.006 9	0.006 6	0.004 4
Occupation number from double-thermal distribution fit (quanta)	0.024	0.024	0.027	0.037	0.044	0.018
Occupation number bounds (quantum)	0-0.06	0-0.05	0-0.04	0-0.06	0-0.09	0-0.04

operated our system at an rf drive frequency $\Omega_T \simeq 2\pi \times 76$ MHz, while the second one, which is applicable to more general trapping conditions, is used at $\Omega_T \simeq 2\pi \times 40$ MHz.

3.5.1 Cooling Pulse Sequence at Drive Frequency $\Omega_T \simeq 2\pi \times 76$ MHz

The conditions of the trap operated at the drive frequency $\Omega_T \simeq 2\pi \times 76$ MHz are summarized in Table 3.2. The first-order RSB cooling pulses for the z-COM mode (Lamb-Dicke parameter $\eta = 0.18$) become less efficient for the population at higher Fock states because of smaller Rabi rates. Therefore, second order RSB pulses are implemented in the sideband cooling pulse sequence. Our simulation shows that including higher order RSB pulses significantly reduces the population in high Fock states.

The optimization process starts by choosing a fixed number of total cooling pulses, $\mathcal{N}$, which sets roughly the time spent for the sideband cooling. We do not perform a global optimization of all the pulse durations and orders because of the numerous degrees of freedom, which makes it numerically challenging. Instead we perform a pulse-by-pulse optimization. We limit the optimizer

to choose either a first or a second order RSB pulse based upon a figure of merit. In a global optimization, the figure of merit is the final total energy, but in a pulse-by-pulse optimization this is not a good choice because it tends to focus on the populations in the low-lying Fock states first, which will be cooled by the subsequent pulses. The *i-th* cooling pulse is chosen from either the first or the second order RSB pulse to minimize

$$\langle n_p \rangle_{opt} = \sum_{n_p=\mathcal{N}-i+1}^{\infty} P_{n_p} n_p, \tag{3.24}$$

which is the total motional energy (in units of $\hbar\omega_p$, where ω_p is the motional frequency of the secular mode p) lying above the Fock state $n_p = \mathcal{N} - i$ after the *i-th* pulse is applied. The logic of choosing this figure of merit is that the remaining $(\mathcal{N} - i)$ pulses ideally will cool all of the population in the states from $n_p = (\mathcal{N} - i)$ to $n_p = 1$ to the ground state by choosing the proper duration of the first-order RSB pulses.

This optimization process was performed for the z-COM mode only because this mode is the most problematic due to its larger Lamb-Dicke parameter and more significant population in higher Fock states after Doppler cooling. The optimization suggests a pulse sequence with multiple second-order RSB pulses followed by a few first-order RSB pulses at the end. In fact, we find the total energy after sideband cooling is not very sensitive to the exact number of the second-order RSB pulses. Hence the cooling pulses we chose for the experiments were a compromise between the optimization results and factors such as the cooling time spent and the ease of parameterizing the cooling sequence in our experimental control system.

The resulting pulse sequences we used in our experiments are the following. For a single $^{25}Mg^{+}$, we applied 17 second-order RSB pulses followed by 8 first-order RSB pulses on the axial mode, and 25 first-order RSB pulses on the two transverse modes. For a $^{25}Mg^{+}$-$^{27}Al^{+}$ ion pair, 15 second-order RSB pulses followed by 25 first-order pulses were applied on the axial modes, while 40 first-order RSB pulses were applied on the transverse modes. Cooling pulses were alternatingly applied to motional modes in the descending order of secular frequencies. The simulated evolution of the average occupation numbers in the six secular modes is plotted against the number of cooling

pulses applied in Fig 3.11. For the two axial modes, the different cooling rates occurring around 100 pulses in the figure corresponds to the change from second-order RSB pulses to first-order RSB pulses. The frequency spectra of all six resolved motional modes is shown in Fig. 2.20.

Figure 3.11: The evolution of average occupation number, $\bar{n}$, during the sideband cooling at $\Omega_T \simeq 2\pi \times 76$ MHz. The trap conditions are given in Table 3.2.

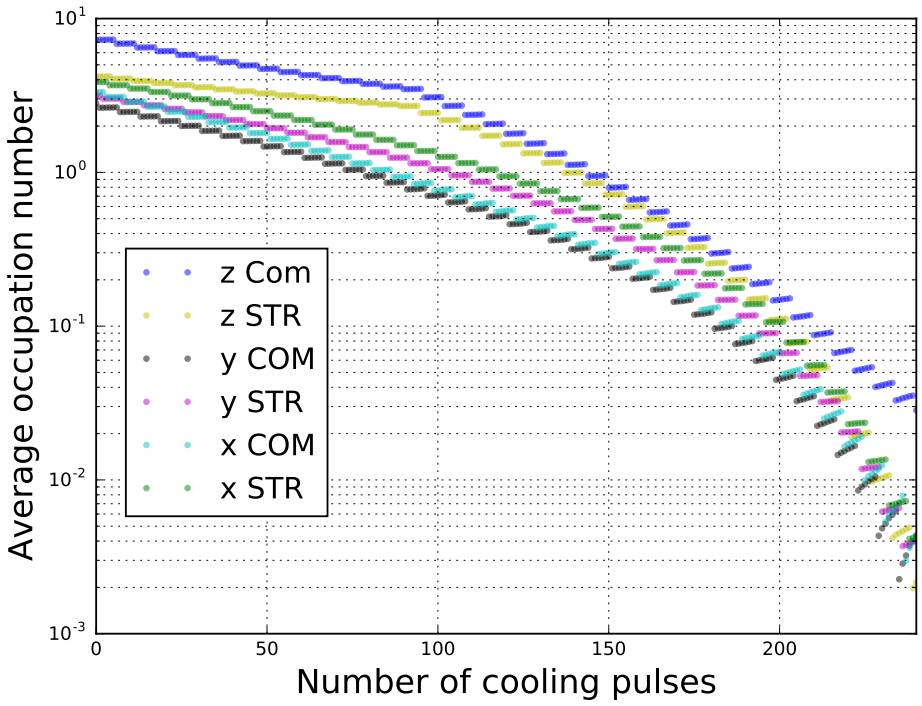

One important conclusion from this optimization process is that two pulse sequences may result in very different Fock state distributions and energy, but yet give very similar results in a typical sideband thermometry experiment. Using second-order sideband pulses was crucial for achieving low energy in the axial modes with higher Lamb-Dicke parameters. While some more improvement may be possible by performing a global optimization, the cooling pulse sequence has provided us with a sufficient solution in terms of the cooling efficiency and the achievable energy for the clock operation.

3.5.2 General Sideband Cooling Pulse Sequence

We have also operated our system at a lower drive frequency, $\Omega_T \simeq 2\pi \times 40$ MHz to reduce the excess micromotion[5] . Due to the trap stability considerations, we fixed the Mathieu parameters q_i given in Eq. (2.5) as we changed the drive frequency. The trap parameters are summarized in Table 3.3. The motional sideband Rabi rates of two secular modes are shown in Fig. 3.12. The first thing we noticed is that there is more population in the higher Fock states after the Doppler laser cooling due to the lower secular frequencies. In addition, the Lamb-Dicke parameters of all secular modes increases significantly. Therefore, sideband cooling utilizing higher order RSB cooling pulses becomes necessary for most modes. Although we can still apply the optimization procedure discussed in the previous section on each secular modes, it becomes too complicated in terms of the parameterization of the cooling sequence in our experimental control system. Therefore we are interested in finding a simple method to design a cooling pulse sequence.

For the clock operation, what we actually care about is the energy that the ions have after sideband cooling. If we apply a sideband cooling pulse sequence consisting of $\mathcal{N}_p$ ideal RSB π pulses to cool a Fock states distribution of the motional mode p in a descending order starting from the Fock state $n = \mathcal{N}_p$, there exists a crude upper bound of the remaining energy after sideband cooling,

$$E(\mathcal{N}_p) \lesssim \hbar \sum_{n_p=\mathcal{N}_p+1}^{\infty} P_{n_p} n_p. \tag{3.25}$$

If the pulse duration is chosen properly, the population in a Fock state n can always be cooled no matter which order of RSB pulse is used. This indicates that the upper bound $E(\mathcal{N}_p)$ is independent of the order of RSB pulses we are using[6] . Therefore, we end up with a rough energy upper bound simply based upon the number of pulses applied. Moreover, since the z-COM mode has the largest occupation number after the sideband cooling, the upper bound for the z-COM mode actually applies for all the other modes. In such a case, the only parameter we need to specify for sideband

[5] See Sec. 4.2 for details.

[6] The zero-point energy is ignored here since it is just an energy offset and plays no role in the sideband cooling process.

Figure 3.12: Motional sideband transition Rabi rates $\Omega_{n,n-\Delta n}$ in units of the carrier transition Rabi rates of the (a) z-COM mode and the (b) x-COM mode when the trap is operated at $\Omega_T \simeq 2\pi \times 40$ MHz. Green bars represent the energy in each Fock state at the Doppler cooling final temperature. The red dashed line denotes the threshold Fock state $\mathcal{N}_p$ such that the energy in the Fock states of the motional mode p above $\mathcal{N}_p$ is less than 10% of the total energy.

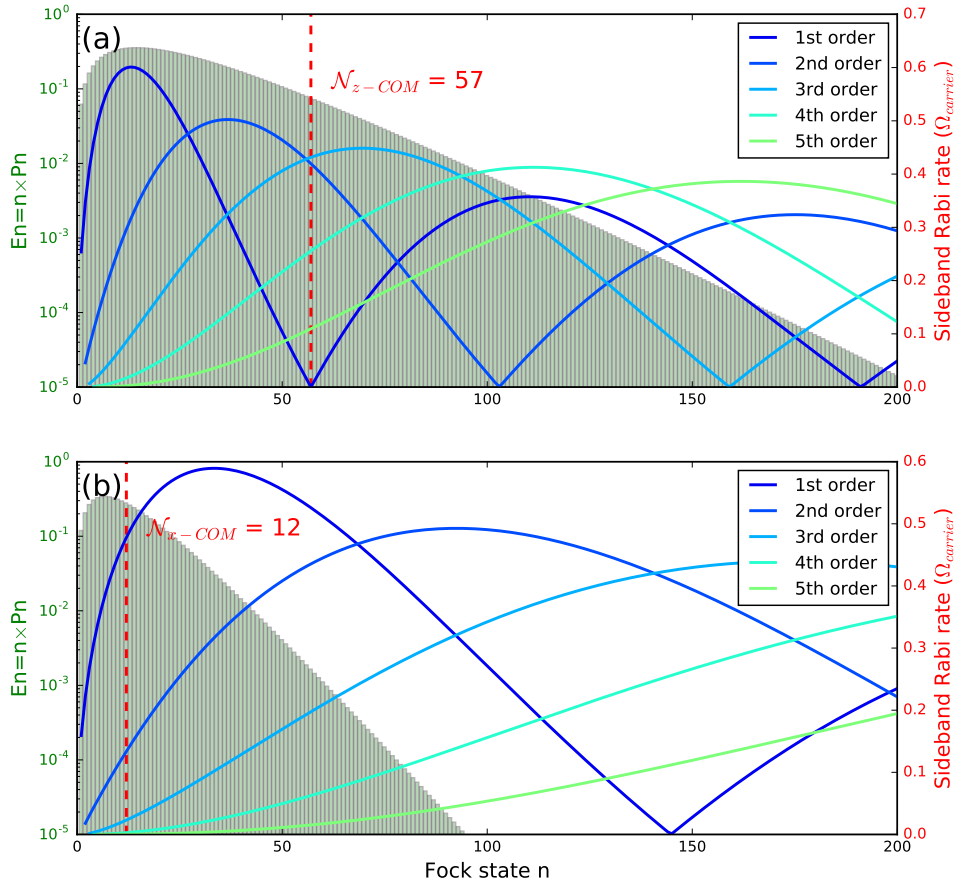

Table 3.3: Parameters of a $^{25}Mg^{+}$-$^{27}Al^{+}$ two-ion pair at 40 MHz drive frequency.

	x-COM	x-STR	y-COM	y-STR	z-COM	z-STR
Frequency (MHz)	3.3	2.85	3.95	3.5	1.5	2.5
Lamb-Dicke parameter ($^{25}Mg^{+}$)	0.16	0.08	0.15	0.065	0.25	0.21
Time-dilation shift per quantum (10^{-18})	−0.11	−0.52	−0.09	−0.52	−0.07	−0.10
Occupation number from simulation (quanta)	0.014	0.033	0.008 0	0.007 5	0.18	0.044
Occupation number from single-thermal distribution fit (quanta)	0.022	0.009 4	0.021	0.005 9	0.060	0.063
Occupation number from double-thermal distribution fit (quanta)	0.069	0.13	0.028	0.005 9	0.98	0.65
Occupation number bounds (quantum)	0-0.10	0-0.16	0-0.04	0-0.01	0-1.31	0-0.78

cooling the $^{25}Mg^{+}$-$^{27}Al^{+}$ ion pair is just one: the ratio of the "crude" remaining energy $E(\mathcal{N}_p)$ and the energy after Doppler laser cooling in the z-COM mode. This ratio further sets the number of pulses we should apply on each of secular modes. For our experiment, we usually set this ratio to be 0.1 for the $^{25}Mg^{+}$-$^{27}Al^{+}$ two-ion pair, which guarantees at least 90% of the total energy of ions has been removed during the sideband cooling process. This ratio corresponds to 57 sideband cooling pulses on each of the motional modes.

Although this crude upper bound always holds independent of the orders of the sideband pulses, the final achievable energy and the cooling efficiency do depend on the order of sideband cooling pulses. Again, we only perform a pulse-by-pulse optimization instead of a global optimization because of the numerical difficulties. Suppose we want to apply a RSB π pulse to cool the population P_{n_p} in a specific Fock state n_p of the secular mode p, the amount of energy change per

Figure 3.13: The evolution of average occupation number, $\bar{n}$, during the sideband cooling at $\Omega_T \simeq 2\pi \times 40$ MHz. The trap conditions are given in Table 3.3.

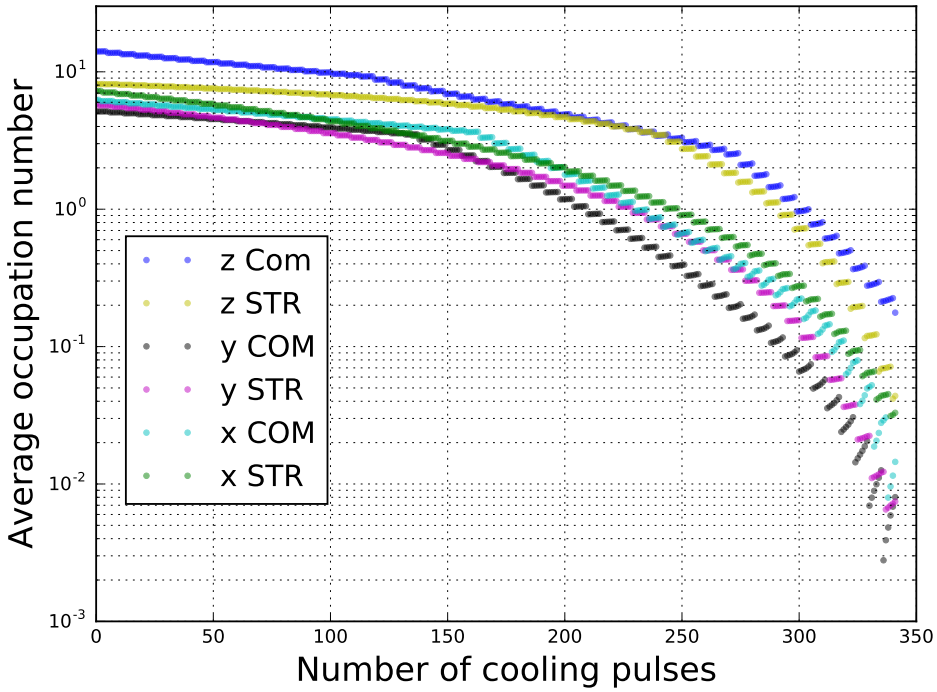

unit time for the population in the Fock state n_p corresponds to

$$\frac{dE(n_p)}{dt} = \frac{2\hbar\Delta n_p\,\Omega_{n_p,n-\Delta n_p}}{\pi} P_{n_p}, \tag{3.26}$$

where $\Omega_{n_p,n_p-\Delta n_p}$ is the Δn_p-th order RSB Rabi rate given in Eq. (3.10). For a sequence consisting of $\mathcal{N}_p$ RSB pulses, the optimization of the i-th pulse is performed by choosing the order of the RSB transitions to maximize the energy change per unit time in the Fock state $n_p = (\mathcal{N}_p - i + 1)$, $dE(\mathcal{N}_p - i + 1)/dt$, for a given Lamb-Dicke parameter η_p. Currently our experimental control system is programmed in such a way that the computer will perform the optimization processes on all six motional modes and automatically choose the pulse durations and frequencies with given $\mathcal{N}_p$ and η_p. The simulated evolution of the average occupation number of six secular modes during this cooling pulse sequence is shown in Fig. 3.13. The pulse sequence used to cool $^{25}Mg^{+}$-$^{27}Al^{+}$ at $\Omega_T \simeq 2\pi \times 40$ MHz is summarized in Table 3.4. In the experiment, the pulses were alternatingly

applied to motional modes in a descending order of secular frequencies. Typically, this cooling sequence took about 10 ms to cool all six modes close to the motional ground state.

Table 3.4: Number of sideband cooling pulses of each sideband order for the drive frequency $\Omega_T \simeq 2\pi \times 40$ MHz.

Sideband order	3	2	1
x-COM	0	27	30
x-STR	0	0	57
y-COM	0	23	34
y-STR	0	0	57
z-COM	19	26	12
z-STR	1	39	17

3.6 Clock Frequency Shifts and Uncertainties due to Secular Motion

3.6.1 Determination of the Energy after Sideband Cooling

The main goal of the development of the numerical model is to determine the ions' energy after sideband cooling to a desired accuracy. As an example, the simulated Fock state distribution of the z-COM mode after sideband cooling at the 76 MHz drive frequency is shown in Fig. 3.14. Besides the thermal-like distribution for the Fock states $n < 3$, we note that there is a plateau probability distribution for Fock states $n \gtrsim 5$ appearing in our simulation. Although the sum of the probability in the plateau distribution is typically too small to be observed in the experiments, our simulation indicates that it usually contributes more than 90% of the total energy. For the z-COM mode at $\Omega_T \simeq 2\pi \times 76$ MHz, about 95% of the total energy is in the plateau distribution in the higher Fock states.

To include the energy contribution from this "hidden" population, we fit the simulated Fock state distribution to a linear combination of two thermal distributions to extract the mean occupation number $\bar{n}_h$ that characterizes the energy of the plateau distribution. Given $\bar{n}_h$ as a fixed parameter, we then fit the RSB Rabi oscillation data shown in Fig. 3.16 to a double thermal

distribution. The probability in a specific Fock state $P(n)$ is expressed as

$$P(n) = \alpha \mathcal{P}_{th}(n|\bar{n}_l) + (1-\alpha)\mathcal{P}_{th}(n|\bar{n}_h), \tag{3.27}$$

where $\bar{n}_h$ is derived from the simulation and $\bar{n}_l$ is a fit parameter that characterizes the energy in the lower Fock states. The probability $\mathcal{P}_{th}(n|\bar{n})$ denotes the population in the Fock state $|n\rangle$ of the thermal distribution with the average occupation number $\bar{n}$, which is given in Eq. (3.4), and α represents the weight between the two thermal distributions.

The effect of off-resonant carrier transitions is also considered in the analysis. The off-resonant transitions cause a small amplitude ($< 0.5\%$), high frequency ($\gtrsim 1$ MHz) oscillation in addition to the residual RSB Rabi oscillation. Because the residual RSB and off-resonant carrier transitions have very different frequencies, the transition probabilities at any given pulse duration can be approximated by the sum of these two effects. Unfortunately, we do not have the required timing resolution in our experimental control system to resolve the off-resonant transitions. To include this effect in our energy estimate, we first record the laser power as a function of time for the experimental pulses and numerically calculate the off-resonant carrier transition amplitudes. Then we assume the fast oscillations due to the off-resonant transitions cause an offset towards higher transition probability and scatter of the experimental data. Therefore, we add this additional offset to our fitting model and represent the scatter as the red shaded region as shown in Fig. 3.16. For the system operating at 76 MHz drive frequency, this effect is significant for the data of the z-COM RSB transition but not the other motional modes. This is due to the adiabaticity arising from the relatively long turn-on and turn-off time of the laser pulses (~ 100 ns) in comparison with the oscillation frequencies.

In Fig. 3.16, we also show mean occupation numbers from both the fit to the single and double thermal distribution models and the simulation. In general the least-squared fit to the Rabi oscillation curves using the double thermal distribution model give a factor of two to three smaller in χ^2 in comparison with the single thermal distribution model. Moreover the double thermal distribution fit tends to give a higher estimate of the ions' energy. Therefore, the 95%

Figure 3.14: The simulated Fock state distribution in z-COM mode after sideband cooling at $\Omega_T \simeq 2\pi \times 76$ MHz. The red line represents a fit to a double-thermal distribution with mean occupation numbers 0.004 and 11, and weights 0.99 and 0.01.

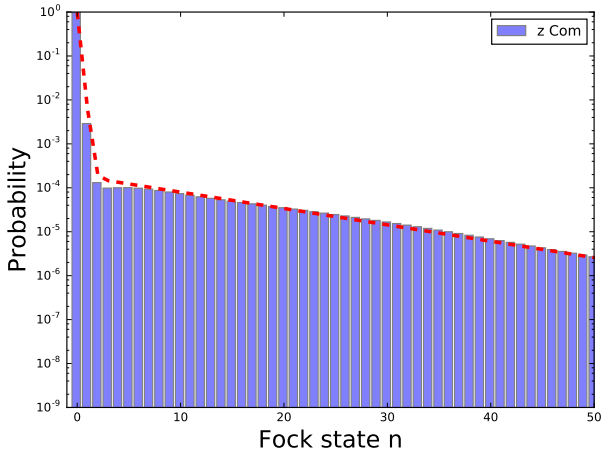

confidence interval of the fit to a double thermal distribution is used as the estimate of the energy upper bound. To examine the effects of both the non-linearity of the fitting model and the non-Gaussian distribution of the experimental data, we performed a bootstrapping test by re-sampling residuals [DiCiccio 96]. The results were consistent with that from the least-squares fit.

The energy determination was performed at two different drive frequencies, $\simeq 40$ and $\simeq 76$ MHz. The heating contributions are summarized in Table 3.5 and Table 3.6. The fit to the RSB transitions of the residual motional excitation are plotted in Fig. 3.15 and Fig. 3.16. The results are summarized in Table 3.3 and Table 3.2.

3.6.2 Time-dilation Shift due to Secular Motion

The time-dilation shift per motional quantum for the two rf drive frequencies are shown in Table 3.3 and Table 3.2. Note that the shifts include the contributions from the IMM. As discussed in Sec. 2.8, for the sideband cooled optical clock utilizing the protocol $\mathscr{B}$, there is no additional cooling light shift during the clock interrogation. As a result, we can completely eliminate the associated light shift existing in the previous $^{27}Al^{+}$ optical clocks that used the protocol

Figure 3.15: Red-sideband Rabi oscillations on the $|\downarrow\rangle \rightarrow |\uparrow\rangle$ transition of $^{25}Mg^{+}$ for the six $^{25}Mg^{+}$-$^{27}Al^{+}$ motional modes after sideband cooling at $\Omega_T \simeq 2\pi \times 40$ MHz. The blue data points are the average of experimental data and the error bars are the standard deviation of the mean. Solid line: double-thermal distribution fit; dotted line: single-thermal distribution fit; dashed line: simulation. The red shaded regions represent the range of the off-resonant carrier transitions. The insets represent the average occupation numbers from fits and the simulation. Diamond: simulation; circle: single thermal distribution fit; square: double thermal distribution fit. The green error bars represent the experimentally determined uncertainties of average occupation numbers after sideband cooling. The upper bound of energy is given by the 95% confidence interval of the double-thermal distribution fit.

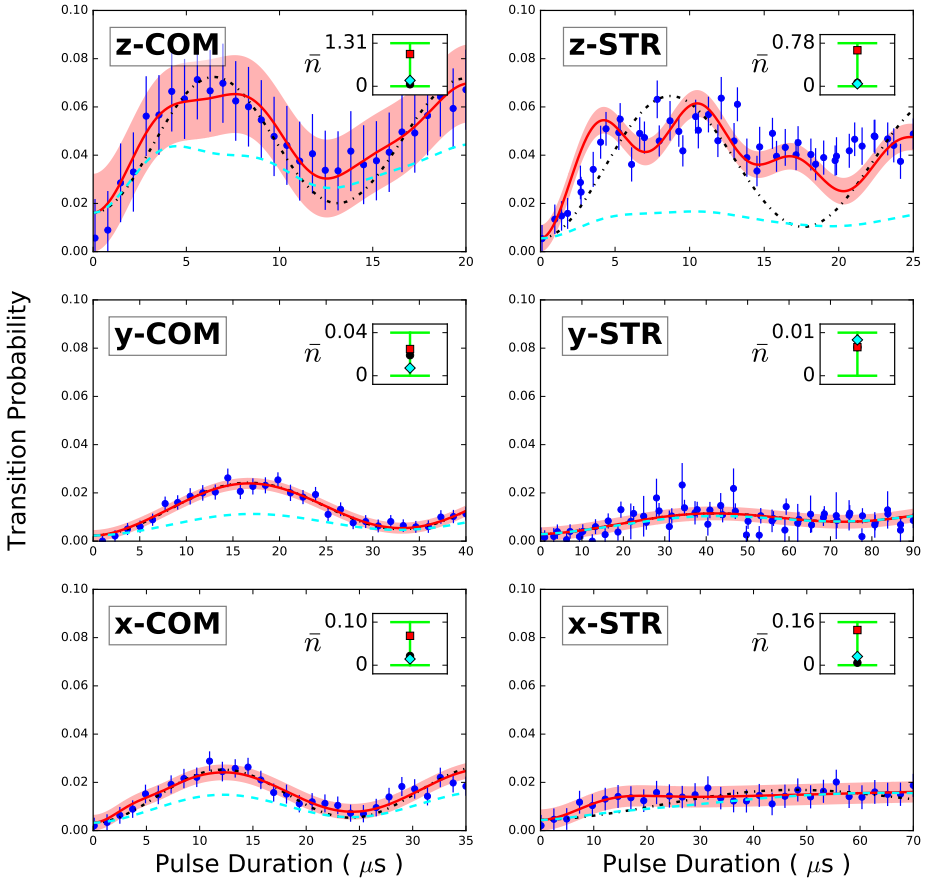

Figure 3.16: Red-sideband Rabi oscillations on the $|\downarrow\rangle \rightarrow |\uparrow\rangle$ transition of $^{25}Mg^{+}$ for the six $^{25}Mg^{+}$-$^{27}Al^{+}$ motional modes after sideband cooling at $\Omega_T \simeq 2\pi \times 76$ MHz. The blue data points are the average of about 50 000 experiments and the error bars are the standard deviation of the mean. Solid line: double-thermal distribution fit; dotted line: single-thermal distribution fit; dashed line: simulation. The red shaded regions represents the range of the off-resonant carrier transitions of the double-thermal distribution fit, which is significant for the z-COM mode, but not the other motional modes. The insets represent the average occupation numbers from fits and the simulation. Diamond: simulation; circle: single thermal distribution fit; square: double thermal distribution fit. Circles overlay diamonds to within less than the size of the symbol. The green error bars represent the experimentally determined uncertainties of average occupation numbers after sideband cooling. The upper bound of energy is given by the 95% confidence interval of the double-thermal distribution fit.

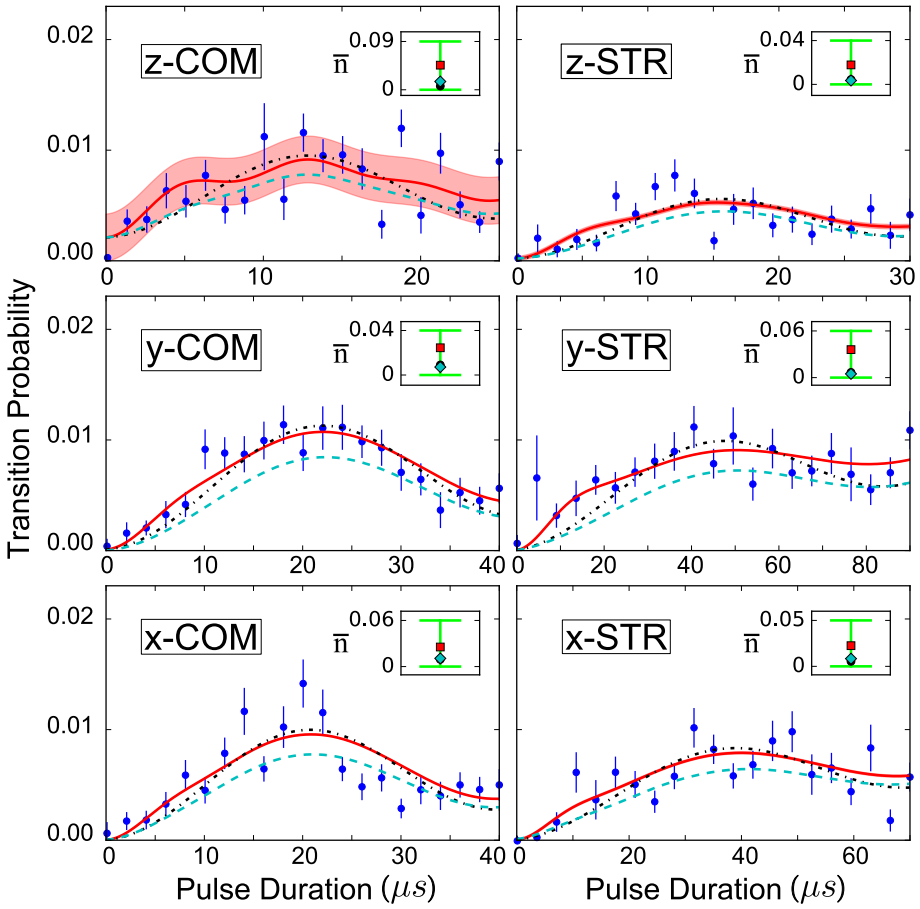

Table 3.5: Summary of heating rates due to different mechanisms considered in the simulation at 40 MHz drive frequency.

	x-COM	x-STR	y-COM	y-STR	z-COM	z-STR
Repumping sequence (quanta/cycle)	0.037	0.015	0.009	0.002	0.082	0.031
Raman scattering (quanta/μs)	4.6×10^{-5}	1.2×10^{-5}	4.1×10^{-5}	8.7×10^{-6}	5.8×10^{-5}	3.9×10^{-5}
Rayleigh scattering (quanta/μs)	2.3×10^{-5}	6.0×10^{-6}	2.1×10^{-5}	4.4×10^{-6}	2.9×10^{-5}	2.0×10^{-5}
Off-resonant coupling (quanta/pulse)	7.4×10^{-4}	1.3×10^{-3}	4.8×10^{-4}	6.0×10^{-4}	8.8×10^{-3}	2.0×10^{-3}
Spontaneous decay and RSB (quanta/pulse)	1.1×10^{-3}	2.3×10^{-3}	1.3×10^{-3}	2.8×10^{-3}	7.4×10^{-4}	9.3×10^{-4}
Electric field noise (quanta/s)	21.0 ± 0.4	4.4 ± 0.5	19.9 ± 0.4	4.5 ± 0.2	26.5 ± 2.7	1.9 ± 0.2

Table 3.6: Summary of heating rates due to different mechanisms considered in the simulation at 76 MHz drive frequency.

	x-COM	x-STR	y-COM	y-STR	z-COM	z-STR
Repumping sequence (quanta/cycle)	0.015	0.004	0.012	0.002	0.027	0.017
Raman scattering (quanta/μs)	4.6×10^{-5}	1.2×10^{-5}	4.1×10^{-5}	8.7×10^{-6}	5.8×10^{-5}	3.9×10^{-5}
Rayleigh scattering (quanta/μs)	2.3×10^{-5}	6.0×10^{-6}	2.1×10^{-5}	4.4×10^{-6}	2.9×10^{-5}	2.0×10^{-5}
Off-resonant coupling (quanta/pulse)	3.9×10^{-4}	3.6×10^{-4}	2.1×10^{-4}	3.3×10^{-4}	1.6×10^{-3}	6.5×10^{-4}
Spontaneous decay and RSB (quanta/pulse)	1.4×10^{-3}	2.6×10^{-3}	1.5×10^{-3}	3.1×10^{-3}	7.5×10^{-4}	9.1×10^{-4}
Electric field noise (quanta/s)	11.95 ± 0.64	1.94 ± 0.08	9.47 ± 1.00	1.96 ± 0.18	9.12 ± 0.32	0.34 ± 0.02

$\mathscr{A}$ [Rosenband 08, Chou 10a]. After preparing ions in the 3D motional ground state following the protocol $\mathscr{B}$, the average occupation number of the ions in a specific motional mode p during a clock interrogation of duration t_i can be expressed as

$$\langle n_p(t_i)\rangle = \bar{n}_{p,0} + \frac{1}{2}\dot{\bar{n}}_p t_i, \tag{3.28}$$

where $\bar{n}_{p,0}$ is the energy after sideband cooling given in Table 3.3 and Table 3.2, and $\dot{\bar{n}}_p$ is the heating rate due to ambient electric field noise given in Table 3.5 and Table 3.6. Angle brackets denote a time-average over the clock interrogation time. The upper bound on the fractional time-dilation shift is estimated as the $\frac{t_i}{2}\left(\dot{\bar{n}}_p + 2\sigma_{\dot{\bar{n}}_p}\right)$ value added with the upper bound of $\bar{n}_{p,0}$. Here $\sigma_{\dot{\bar{n}}_p}$ is standard deviation of the mean of the heating rate measurements given in Table 3.5 and Table 3.6. For the lower bound, we take the mode p to be initially in its ground state and use $\frac{t_i}{2}\left(\dot{\bar{n}}_p - 2\sigma_{\dot{\bar{n}}_p}\right)$ as the contribution from the heating. The bounds of the time-dilation shift for a specific mode p are given as

$$\begin{aligned}\left(\frac{\delta f}{f}\right)_p^{upper(lower)} &= \left(\frac{\delta \nu_p}{f}\right)\langle n_p(t_i)^{upper(lower)}\rangle \\ &= \left(\frac{\delta \nu_p}{f}\right)\left(\bar{n}_{p,0}^{upper(lower)} + \frac{t_i}{2}(\dot{\bar{n}}_p \pm 2\sigma_{\dot{\bar{n}}_p}\right)\end{aligned} \tag{3.29}$$

where $\delta\nu_p$ denotes the secular motion time-dilation shift per motional quantum. Finally, we conservatively assume the shifts in six different secular modes are correlated, which should be the worst case, and use the average of the upper bound and lower bound as the estimate for the time-dilation shift.

$$\left(\frac{\delta f}{f}\right)_{secular}^{upper(lower)} = \sum_p \left(\frac{\delta f}{f}\right)_p^{upper(lower)}, \tag{3.30}$$

$$\left(\frac{\delta f}{f}\right)_{secular} = \frac{\left(\frac{\delta f}{f}\right)_{secular}^{upper} + \left(\frac{\delta f}{f}\right)_{secular}^{lower}}{2}. \tag{3.31}$$

The time-dilation shifts and uncertainties due to the secular motion of the protocol $\mathscr{A}$ and the protocol $\mathscr{B}$ are plotted together in Fig. 3.17. More than an order of magnitude reductions in both the shift and the uncertainty are achieved at both rf drive frequencies at our typical clcok interrogation time.

Figure 3.17: Comparison of the secular motion time-dilation shifts in two different clock operation protocols. The blue line, yellow line, and the red line represent the fractional frequency shifts, while the shaded regions are uncertainties. For a typical clock interrogation time of 150 ms, the secular motion time-dilation shift of a sideband cooled optical clock is $-1.7^{+0.3}_{-0.2} \times 10^{-18}$ at $\Omega_T \simeq 2\pi \times 40$ MHz; $-(1.9 \pm 0.1) \times 10^{-18}$ at $\Omega_T \simeq 2\pi \times 76$ MHz. The uncertainty of a Doppler cooled optical clock is the sum of the secular motion time-dilation shift, $-(16.3 \pm 5.0)^{-18}$, and the ac Stark shift from the Doppler cooling light, $-(3.6 \pm 1.5) \times 10^{-18}$ [Chou 10a].

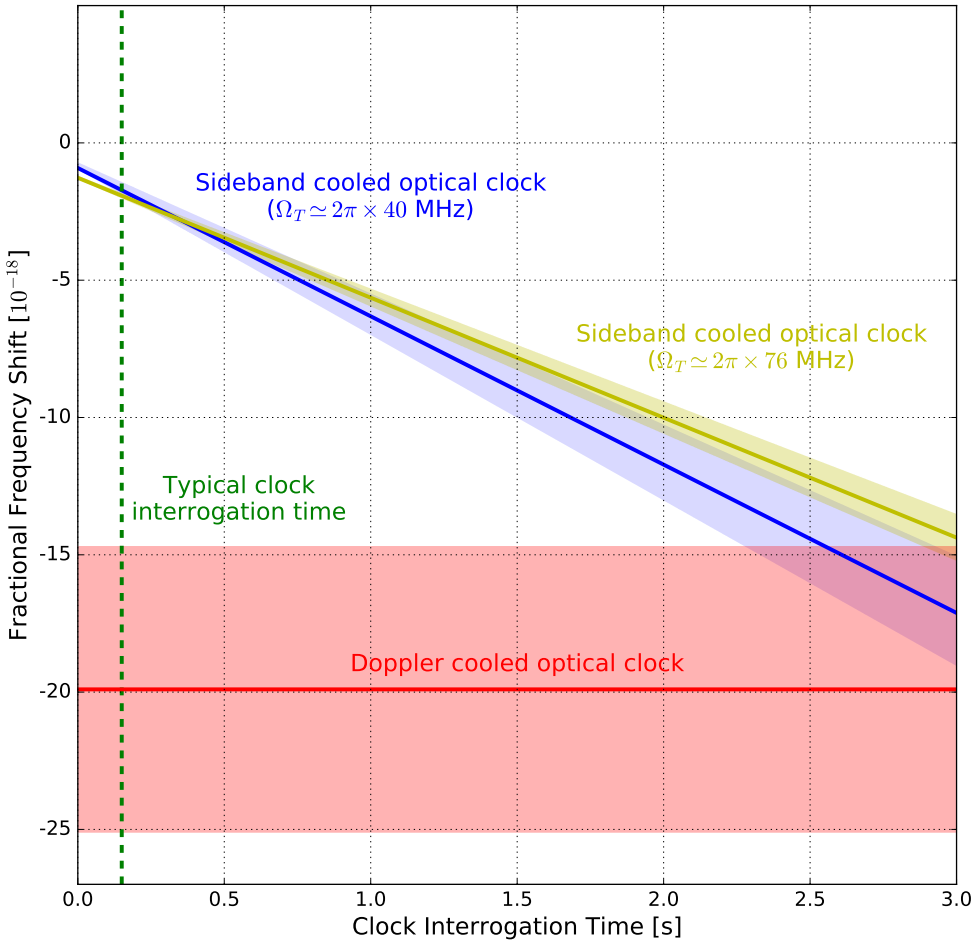

Chapter 4

Other Systematic Effects and Concerns

In the previous chapter, I discussed how we implemented a new clock protocol to reduce both the secular motion time-dilation shift and its uncertainty to be below the mid-10^{-19} level. In this chapter I will describe several other systematic effects that influence the $^{27}Al^{+}$ optical clock operation and certain considerations for running the clock.

4.1 Linear Doppler Shift

In addition to the quadratic Doppler shift discussed in the previous chapter, atoms with a nonzero velocity in the lab frame experience a linear Doppler shift, which is given by

$$\frac{\delta f}{f} = \frac{\vec{v} \cdot \hat{k}_L}{c}, \tag{4.1}$$

where $\vec{v}$ is the velocity of the atom, and $\hat{k}_L$ is the unit wavevector of the probe laser. However, with the typical secular frequencies of a few MHz and rf drive frequencies of a few tens of MHz, the ion's secular motion and micromotion do not shift the observed frequency but instead results in frequency sidebands with Rabi rates given in Eq. (3.10). In such a case, the resulting systematic frequency shift is due to the line-pulling effect caused by the motional sidebands. Because the transform-limited width of the interrogation pulse is much smaller than the lowest characteristic frequency of ion's motion and the sideband Rabi rates are reduced by the Debye-Waller effect, the clock frequency shift due to the line pulling effects is estimated to be $\ll 1\,\mu$Hz and hence negligible[1]

.

Another source of linear Doppler shift arises from the recoil during the interrogation. However the trapped ion is immune to this effect because of the Mössbauer effect [Dicke 53, Bergquist 87, Rosenband 08].

Therefore, we only need to consider the ion's motion with a characteristic time scale similar to or larger than the interrogation pulse duration. Possible sources of motion are long-term variations of the trapping potential, and thermal drifts of the uncompensated laser beam path and the trap structure. The linear Doppler shift due to these slow drifts can be suppressed by probing the atomic transition alternately using counterpropagating beams, which averages the frequency shift to zero if the drifts are not correlated with the probe direction [Rosenband 08]. This will be characterized on the fly when the clock is operating.

4.2 Excess Micromotion Shift

4.2.1 Introduction

One of the main contributions to the systematic uncertainties in all the ion-based optical frequency standards is the time-dilation shift due to EMM [Rosenband 08, Chou 10a, Barwood 14, Huntemann 16]. EMM arises from the imperfections of the trapping potential, which have been studied thoroughly in the literature [Berkeland 98]. Among all proposed ion species for optical frequency standards, $^{27}Al^{+}$ is among the most sensitive to these imperfections due to its smaller mass. There are two types of imperfections that lead to EMM. The first type of imperfections is an additional dc electric field, which might result from charges on the surfaces of dielectric materials. This dc electric field will push ions away from the rf pseudopotential minimum such that ions experiences additional micromotion. This type of EMM can be compensated routinely by applying suitable dc voltages to the trap electrodes; its magnitude is usually limited by how well we can measure and compensate it. I will discuss how we measure and compensate EMM in Sec. 4.2.2. The

[1] This assumes the ion is in the motional ground state, which is a worst case that leads to the largest frequency shift.

second type of EMM is caused by phase imbalances between the rf electrodes, which usually result from imperfections of the trap fabrication, including the geometrical asymmetry and the impedance mismatching between electrodes. This type of EMM is difficult to reduce externally once the trap is made and hence sets the minimum of EMM of a Paul trap. However, it is possible to reduce EMM due to phase imbalances by adjusting the trap drive frequencies. This was demonstrated in our system and will be discussed in Sec. 4.2.3.

4.2.2 Characterization and Compensation

Many experimental techniques have been developed to measure and to compensate EMM to a high precision [Berkeland 98, Chuah 13, Keller 15, Gloger 15]. In our experiments, the sideband ratio method was used to characterize the EMM. To compensate the EMM due to stray electric fields, two dc compensation electrodes as shown in Fig. 4.1, fabricated on the trap wafer, and the endcap electrodes provide the necessary degrees of freedom in three orthogonal directions. The ions are pushed around the trap center by these electrodes to null out the dc fields accounting for the EMM. The initial compensation of EMM was performed in two ways. The EMM in the horizontal plane was compensated by adjusting the dc compensation voltages such that the ion position does not change when the trap rf potential amplitude is varied; the EMM in the vertical direction was compensated by minimizing the EMM sideband of the $^{27}Mg^+$ transition $|\downarrow\rangle \leftrightarrow |^2P_{3/2}, F = 3, m_F = -3\rangle$ using the BR-v beam tuned to be on resonance. The ultimate EMM compensation and determination were performed by measuring the Rabi rate of the EMM sidebands in both the $^{25}Mg^+$ Raman transition $|\downarrow\rangle \leftrightarrow |\uparrow\rangle$ and the $^{27}Al^+$ transitions $|^1S_0\rangle \leftrightarrow |^3P_1\rangle$, which are both in the resolved sideband regime.

As shown in Eq. (2.1) and Eq. (2.6), the frequency spectrum of the ion's motion in an ideal linear Paul trap consists of frequency components at ω_i and $(\omega_i \pm \Omega_T)$, which give rise to motional sidebands on the transitions at these frequencies. There is no pure tone at the rf drive frequency Ω_T. However, when the ion is exposed to an EMM field, the component of the ion's motion at the

Figure 4.1: (a) Electrodes fabricated on the wheel trap wafer used throughout this thesis. Note that diagonal electrodes are hard-wired together on the wafer. Voltages V_1 and V_2 represent the actual rf potential applied to the ion, while V_0 denote the rf potential before splitting the lead into two. (b) A simple circuit model demonstrates the asymmetry between two diagonal electrodes in our ion trap. The rf phase imbalance can be explained by introducing the different capacitance to the ground of different rf electrodes.

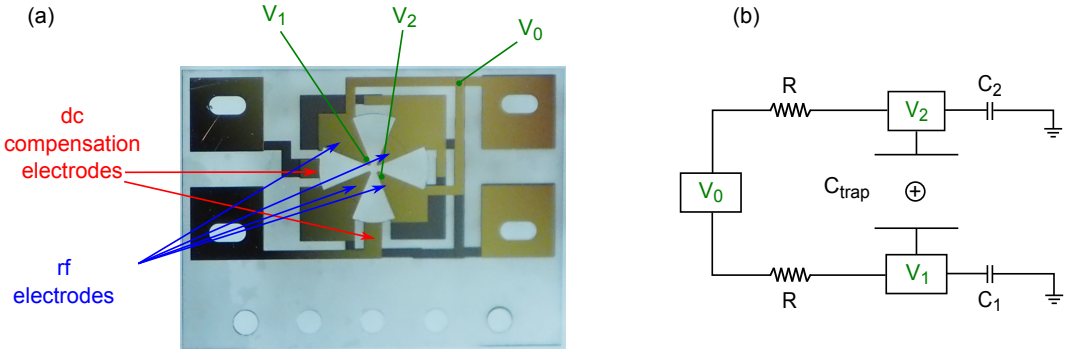

frequency Ω_T is given by

$$m\dot{\vec{v}}_{EMM} = Q\vec{E}_{EMM}\cos(\Omega_T t), \tag{4.2}$$

$$\langle v_{EMM}^2 \rangle = \frac{1}{2}\left(\frac{QE_{EMM}}{m\Omega_T}\right)^2, \tag{4.3}$$

where $\vec{v}_{EMM}$ is the velocity of the ion caused by the EMM field $\vec{E}_{EMM}\cos(\Omega_T t)$. This leads to a phase modulation of the probe laser field. The atomic transition spectrum $I(\omega)$ is approximately given by [Keller 15]

$$I(\omega) \simeq J_0(\beta)\delta(\omega-\omega_L) + J_1(\beta)\left(\delta(\omega-\omega_L+\Omega_T)+\delta(\omega-\omega_L-\Omega_T)\right), \tag{4.4}$$

where δ is the Dirac delta function, ω_L is the probe laser frequency, and J_i is the i-th order Bessel function of the first kind. Here, $\beta = \vec{k}_L \cdot \vec{v}_{EMM}/\Omega_T$ denotes the modulation index resulting from the EMM, where $\vec{k}_L$ is the wavevector of the probe laser. The ratio of the Rabi rates of the carrier and the EMM sideband transitions is approximated by

$$\frac{\Omega_{EMM}^{(\pm1)}}{\Omega^{(0)}} \simeq \frac{\beta}{2}, \tag{4.5}$$

where $\Omega_{EMM}^{(\pm1)}$ and $\Omega^{(0)}$ represent Rabi rates of the first-order EMM sideband and carrier transitions,

respectively. Experimentally the amount of EMM is determined by measuring the ratio of the π-pulse duration of the carrier and EMM motional sideband transitions,

$$\xi = \frac{t_{\pi}^{(0)}}{t_{\pi,EMM}^{(\pm 1)}} = \frac{\Omega_{EMM}^{(\pm 1)}}{\Omega^{(0)}}. \tag{4.6}$$

The resulting fractional frequency shift due to the time dilation effect in a $^{27}Al^{+}$ optical clock due to E_{EMM} is given by

$$\left(\frac{\delta f}{f}\right)_{EMM} = -\frac{\langle v_{EMM}^2 \rangle}{2c^2} = -\left(\frac{QE_{EMM}}{2m_{\mathrm{Al}}c\Omega_T}\right)^2 = -\frac{\Omega_T^2 \xi^2}{k_L^2 c^2}\left(\frac{m_{\mathrm{probe}}}{m_{\mathrm{Al}}}\right)^2, \text{ and} \tag{4.7}$$

$$E_{EMM} = \left(\frac{2m_{\mathrm{probe}}\Omega_T^2}{k_L Q}\right)\xi, \tag{4.8}$$

where m_{probe} denotes the mass of the ion that is used to measure the EMM. One thing to emphasize here is that E_{EMM} in Eq. 4.8 includes effects from both the stray dc electric fields and the phase imbalance, while adjusting the dc fields to minimize ξ can only compensate the EMM due to the stray dc fields.

4.2.3 Residual EMM due to Phase Imbalances

The magnitude of the time dilation shift due to EMM resulting from the phase imbalance is given in Eq. 19 in Ref. [Berkeland 98], which scales as

$$\left(\frac{\delta f}{f}\right)_{EMM}^{phase} \propto q^2\, \delta\phi^2\, \Omega_T^2, \tag{4.9}$$

where $\delta\phi$ denotes the rf phase difference between electrodes and q is the Mathieu parameter. If we keep the Mathieu parameter q the same when we adjust the rf drive frequency Ω_T to maintain the stability of the ions' motion, the time-dilation shift has a relation as

$$\left(\frac{\delta f}{f}\right)_{EMM}^{phase} \propto \delta\phi^2\, \Omega_T^2, \tag{4.10}$$

and the secular frequencies scale as

$$\omega_i \propto \Omega_T. \tag{4.11}$$

Therefore, without changing the trap design, we can reduce the EMM time dilation shift by lowering the rf drive frequency Ω_T. The drawback is the smaller secular frequencies, which leads to

longer cooling times. In addition, smaller secular frequencies imply larger Lamb-Dicke parameters which make the sideband cooling more difficult as discussed in Sec. 3.5 [Wan 15, Chen 17]. Moreover the heating rate also increases when the secular frequencies decreases [Gesley 85, Wineland 98, Daniilidis 11, Safavi-Naini 11, Hite 12]. Fortunately, our understanding of sideband cooling presented in Chapter 3 resolves the above issues and makes it possible to operate the clock at the lower trap drive frequency.

In our ion trap, the phase difference $\delta\phi$ can be explained by the different capacitive coupling between each rf electrode and ground, which is presented in Fig. 4.1. The circuit model in Fig. 4.1 leads to a scaling of $\delta\phi$ as

$$\delta\phi \propto \Omega_T(\mathrm{C}_1 - \mathrm{C}_2) \propto \Omega_T. \tag{4.12}$$

Substituting Eq. 4.12 into Eq. 4.10, we obtain

$$\left(\frac{\delta f}{f}\right)^{phase}_{EMM} \propto \Omega_T^4. \tag{4.13}$$

In Fig. 4.2, the measured and predicted total time-dilation shift due to EMM is plotted against Ω_T in comparison with the time-dilation shift due to the secular motion in a sideband cooled clock given in Chapter 3. We can see that our model agrees with the experimental observation nicely.

4.2.4 Evaluation of the Time Dilation Shift due to EMM

In previous sections, we discussed how we measure and compensate the EMM in our system. However in a realistic linear Paul trap, there is one more issue that needs to be addressed: the EMM along the z direction, denoted as a-EMM. In an ideal linear Paul trap, the a-EMM does not exist. However, due to the manufacturing imperfections and the finite length of the trap, a non-negligible a-EMM typically exists. The a-EMM was mapped out with the stimulated Raman transition of a single $^{25}\mathrm{Mg}^+$ using the combination of the RR and the BR-a beams. The result is depicted in Fig. 4.3. When we operate the trap at $\Omega_T \simeq 2\pi \times 40$ MHz, the typical axial frequency is about 1.5 MHz and the distance between the $^{27}\mathrm{Mg}^+$ and the $^{27}\mathrm{Al}^+$ is about $5\,\mu m$. Therefore, we can operate the clock in two conditions. In the first condition, the $^{27}\mathrm{Al}^+$ is positioned at the minimum

Figure 4.2: Time dilation shift due to EMM and secular motion with respect to the drive frequency $\Omega_T/2\pi$. Blue dashed line: estimated time dilation shift due to EMM when keeping the Mathieu parameter q_i constant. Red square: measured time dilation shift due to EMM. Green diamond: measured time dilation shift due to the secular motion given in Chapter 3.

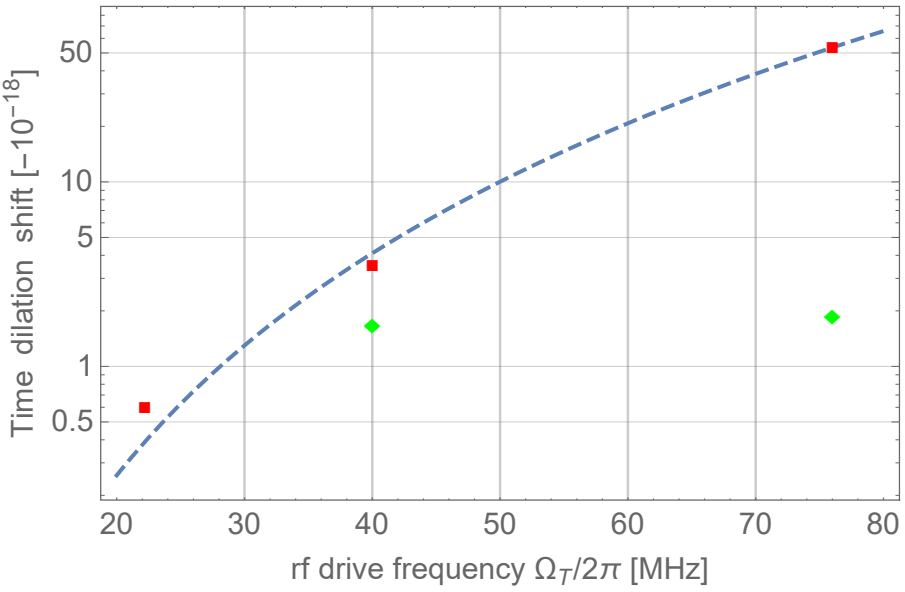

of the time dilation shift due to the a-EMM, which corresponds to a shift $(\delta f/f) \simeq -8.2 \times 10^{-20}$. In this experimental condition, the $^{27}Al^{+}$ will move by $5\,\mu m$, corresponding to a time dilation shift $(\delta f/f) \simeq -6.0 \times 10^{-18}$, when the $^{25}Mg^{+}$-$^{27}Al^{+}$ two-ion pair reorders due to background gas collisions. We can either post-select the experimental data in the right ion order or add an additional uncertainty to account for the frequency shift when the $^{27}Al^{+}$ is in the wrong position [Chou 10a]. In the second condition, the two ions are equally spaced from the minimum of a-EMM such that the reordering of the two-ion pair does not change the time dilation shift due to the a-EMM. In this condition, the time dilation shift is $(\delta f/f) \simeq -2.0 \times 10^{-18}$ and deterministic ion-order control is not necessary. However, the down side of this operation is that we need to calibrate all of the systematic effects at both positions, which might be tedious experimentally. We prefer to operate our system while the $^{27}Al^{+}$ is held at the minimum of the a-EMM.

The EMM perpendicular to the trap axis in the horizontal plane (h-EMM) can also be evaluated by driving the Raman transition of a single $^{25}Mg^{+}$ with the RR and the BR-t beams.

Figure 4.3: The time dilation shift due to the a-EMM. The blue points are experimental data and the red line is a fit to a second-order polynomial.

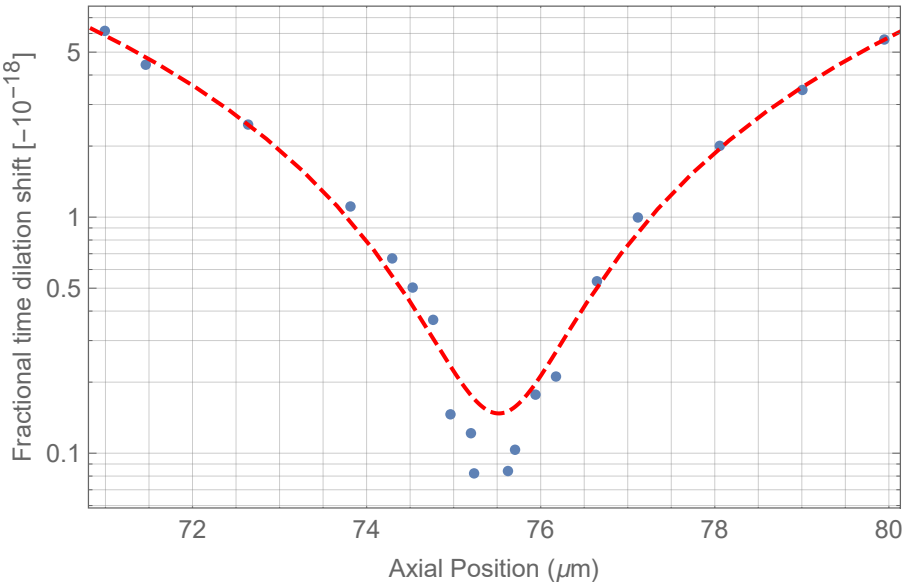

For the last direction, unfortunately the differential wavevector of the RR and the BR-v beams is about 36.5° with respect to the vertical and cannot be easily used to measure the vertical EMM (v-EMM). However it still provides us with sufficient information in the vertical direction for the initial check before doing the $^{27}Al^{+}$ spectroscopy. The v-EMM and h-EMM were both measured using a single $^{25}Mg^{+}$ when we mapped out the a-EMM. We do not see a strong dependence along the trap axis in either v-EMM or h-EMM.

The final evaluation of the time-dilation shift due to the EMM is performed on the $|^1S_0\rangle \leftrightarrow |^3P_1\rangle$ transitions of the $^{27}Al^{+}$. Similar to the evaluation done with $^{25}Mg^{+}$, the ratio between the π times of the carrier and the EMM motional sideband is used to estimate the strength of the EMM field along the direction of the laser beam. Three $^3P_1$ laser beams shown in Fig. 2.8 and Fig. 2.9 probe the EMM in three nearly mutually orthogonal directions. The $\sigma^{+/-}$ transition $|^1S_0, F = 5/2, m_F = \pm 5/2\rangle \leftrightarrow |^3P_1, F = 7/2\, m_F = \pm 7/2\rangle$ is used for the laser beam through the RR/BR-co port, while the π transition $|^1S_0, F = 5/2, m_F = \pm 5/2\rangle \leftrightarrow |^3P_1, F = 7/2\, m_F = \pm 5/2\rangle$ is used for the beams through the BR-a port and vertical port. The capability of EMM compen-

sation using the transition $|^1S_0\rangle \leftrightarrow |^3P_1\rangle$ has a fundamental limit imposed by the excited state lifetime $\tau(^3P_1) \simeq 300\,\mu s$. Note that we are not able to decompose the contribution of the a-EMM and h-EMM when using the $^3P_1$ laser due to the limited optical access available in our system. However, this will not affect the characterization of the total EMM as long as the ion's motion is probed in three orthogonal directions. Unlike the Raman transitions in $^{25}Mg^+$, the vertical $^3P_1$ laser beam is only 10° with respect to the vertical, which contributes $\sim 3\,\%$ of the systematic effect in the determination of the time-dilation shift due to the v-EMM. For the wheel trap version C, which is currently used in the $^{25}Mg^+$-$^{27}Al^+$ system, we found that the v-EMM dominates the EMM. This is caused by the unbalanced coupling of the micromotion compensation electrode to the rf electrodes. This leads to a phase difference between rf electrodes and hence an EMM that cannot be compensated by dc fields [Berkeland 98]. A typical measurements of the time-dilation shift due to the EMM using the $^3P_1$ transitions at $\Omega_T \simeq 2\pi \times 40$ MHz is summarized in Table 4.1, which gives the fractional frequency shift due to the E_{EMM} $\frac{\delta f}{f} \simeq -3.5 \times 10^{-18}$.

In the previous $^{27}Al^+$ optical clocks, the time dilation shift uncertainty due to the EMM was conservatively estimated to be the sum of the frequency shifts in three directions in quadrature [Chou 10a]. This assumption was made to account for the long-term drift of the EMM, possibly due to the variation of built-up charge resulting from the loading process and the rf power drift arising from the thermal effects. However, in our new trap system, we see much smaller drifts of the EMM, which may benefit from the ablation loading, elimination of the dielectric material exposed to the ion, the active rf power stabilization, and the stable phase differences between electrodes. A long-term characterization of the EMM is underway. If we can constrain the uncertainty to be around 30 % of the shift, we can push the time dilation shift uncertainty due to the EMM below 1.0×10^{-18}.

4.3 Blackbody Radiation Shift

Characterizing the frequency shift due to the background blackbody radiation (BBR) is a main challenge among most optical frequency standards. This effect was first proposed and theo-

Table 4.1: The field strength that causes EMM and the resulting time dilation shift measured by the $^3P_1$ transitions.

Port	RR/BR-co	BR-a	vertical
E_{EMM} [V/m]	11.65	26.08	75.47
Fractional time dilation shift	-7.4×10^{-20}	-3.7×10^{-19}	-3.1×10^{-18}

retically studied for atomic frequency standards about four decades ago [Gallagher 79, Itano 81a]. The BBR shift results from off-resonant coupling of the BBR to atomic levels. The frequency shift of an atomic level $|a\rangle$ due to an off-resonant monochromatic radiation $\mathcal{E}_0 \cos(\omega t)$ is

$$\delta\nu_a = -\frac{1}{4h}\mathcal{E}_0^2 \alpha_a(\omega), \tag{4.14}$$

where h is the Planck constant, and $\alpha_a(\omega)$ is the scalar polarizability of the level $|a\rangle$ defined as

$$\alpha_a(\omega) = \frac{e^2}{m_e} \sum_j \left(\frac{f_j}{\omega_j^2 - \omega^2} \right. . \tag{4.15}$$

Here ω_j and f_j denote the frequency and the oscillator strength of transitions that connect to the energy level $|a\rangle$, respectively. Therefore the frequency shift of the transition $|a\rangle \rightarrow |b\rangle$ due to an off-resonant radiation field is given by

$$\Delta\nu = \delta\nu_b - \delta\nu_a = -\frac{1}{4h}\mathcal{E}_0^2 \Delta\alpha_{a\rightarrow b}(\omega), \tag{4.16}$$

where $\Delta\alpha_{a\rightarrow b}(\omega)$ is the differential polarizability between two atomic states. When an $^{27}Al^+$ is exposed to a BBR field, the resulting shift of the clock transition can be calculated by integrating over the power spectrum of the BBR,

$$\Delta\nu_{clock} = \frac{-1}{4\epsilon_0 \pi^3 c^3} \int_0^\infty \left(\Delta\alpha_{clock}(\omega) \frac{\omega^3}{e^{\hbar\omega/k_B T} - 1} d\omega. \right. \tag{4.17}$$

Here k_B and ϵ_0 denote the Boltzmann constant and vacuum permittivity respectively. In Eq. (4.17), we see that the characterizations of both the BBR temperature environment and the differential polarizability are required to evaluate the frequency shift due to the BBR, which will be discussed in the next two sections.

4.3.1 Polarizability of the Clock Transition

The differential polarizability of the clock transition can be rewritten as [Porsev 06]

$$\Delta\alpha_{clock} = \Delta\alpha^0_{clock}(1 + \eta(T)), \tag{4.18}$$

where $\Delta\alpha^0_{clock}$ is the differential dc polarizability and $\eta(T)$ is a small dynamic correction accounting for the other atomic transitions connecting to the two clock states. For the case of the $^{27}Al^+$ clock transition, the dynamic correction is $< 0.4\%$ of the dc polarizability such that we only need to evaluate the effect due to dc polarizability [Mitroy 09, Safronova 11]. To experimentally evaluate the dc polarizability, the ac Stark shift of the clock transition is measured using a near IR laser. And then the dc polarizability is determined by extrapolating the calculated polarizability at the IR laser frequency to the zero frequency [Rosenband 06, Chou 11a]. The dc polarizability is experimentally determined as $\alpha^0_{clock} = (7.02 \pm 0.95) \times 10^{-42}$ $\mathrm{Jm^2/V^2}$ [Chou 11a], which agrees well with the latest theoretical calculation, $(8.2 \pm 0.8) \times 10^{-42}$ $\mathrm{Jm^2/V^2}$ [Safronova 11]. The uncertainty of the measurement is dominated by the characterization of the beam profile of the near IR laser at the position of the $^{27}Al^+$.

4.3.2 BBR Environment

In comparison with other atomic species proposed as the frequency standards [Simon 98, Degenhardt 05, Safronova 11, Sherman 12, Barwood 14, Nicholson 15, Huntemann 16], the relatively smaller dc polarizability of $^{27}Al^+$ indicates that the evaluation of the BBR environment is not as demanding as other optical atomic clocks [Nicholson 15, Beloy 14]. Therefore, instead of doing a full evaluation of the BBR environment, we use the highest and the lowest temperature of the chamber to bound the BBR shift [Chou 10a]. Inside the vacuum, the trap wafer is expected to be at the highest temperature due to resistive heating caused by the rf current. Heat is removed primarily through thermal conduction via the copper post. Three thermocouples are attached to the trap wafer and the post to monitor the temperature during operation. The trap temperature increase above the room temperature versus the rf drive power is shown in Fig. 4.4. When the

Figure 4.4: Rise of the trap temperature above ambient versus rf drive power at $\Omega_T \simeq 2\pi \times 76$ MHz.

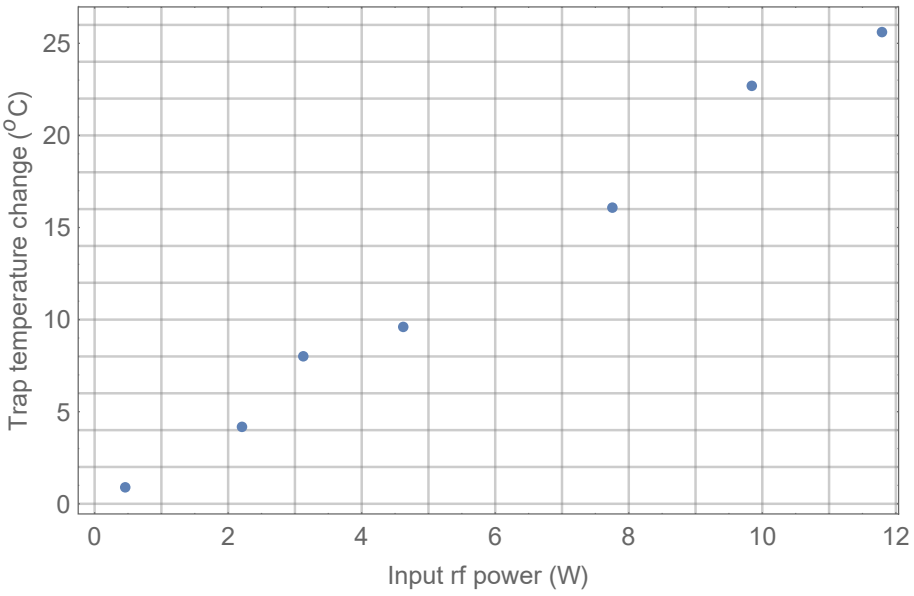

trap is operated at $\Omega_T \simeq 2\pi \times 40$ MHz, the input rf power is 1 W and the trap temperature is $< 5°C$ above room temperature. Including the effect of the room temperature drift, the BBR field impinging upon the $^{27}Al^+$ is bounded in a range $T_{ion} = 20$ - $25\,°C$.

4.3.3 Estimate of Clock Shift due to BBR

Given the differential dc polarizability, the clock frequency shift due to BBR at a certain ambient temperature can be obtained by integrating Eq. (4.17). The fractional frequency shift versus the ambient temperature is shown in Fig. 4.5. From Eq. (4.17), the uncertainty of the BBR shift can be decomposed as

$$\sigma_{\Delta\nu_{clock}} = \left(\frac{k_B^4}{4\hbar^4\epsilon_0\pi^3c^3}\right)\sqrt{\left(\frac{\pi^4}{15}T^4\,\sigma_{\Delta\alpha_{clock}}\right)^2 + \left(\frac{4\pi^4}{15}\Delta\alpha_{clock}\,T^3\Delta T\right)^2}, \tag{4.19}$$

where $\sigma_{\Delta\alpha_{clock}}$ and ΔT denote the uncertainties of the differential polarizability and the measured BBR temperature, respectively. The contribution of the BBR shift at the ambient temperature T= 300 K is shown in Fig. 4.6. In our experimental conditions, the uncertainty arising from the differential polarizability, about a factor of three larger than that due to the temperature

Figure 4.5: The fractional clock frequency shift versus the BBR temperature.

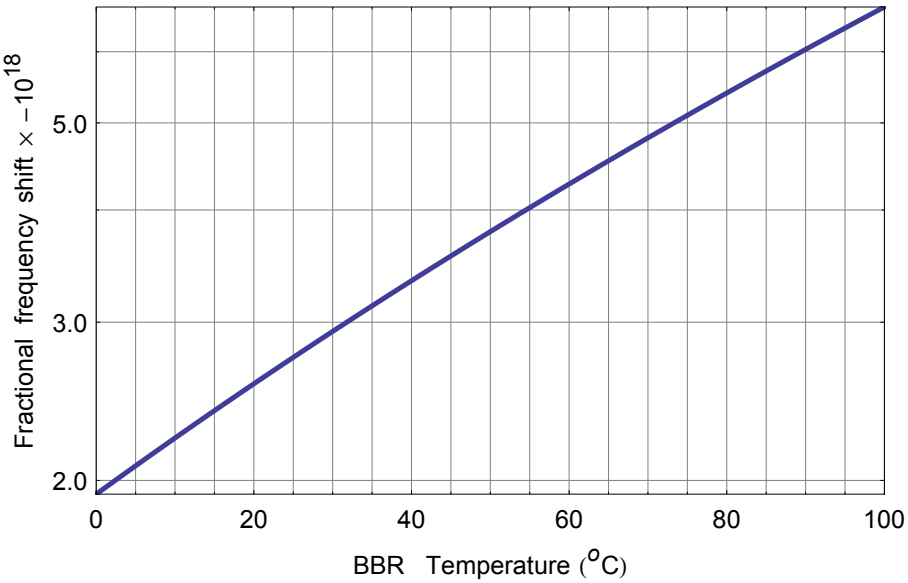

uncertainty, dominates the clock shift uncertainty due to the BBR. The evaluation of the fractional frequency shift uncertainty due to the BBR is $(\delta f/f) = -(2.7 \pm 0.3) \times 10^{-18}$.

Figure 4.6: The of BBR shift uncertainty at the ambient temperature T= 300 K.

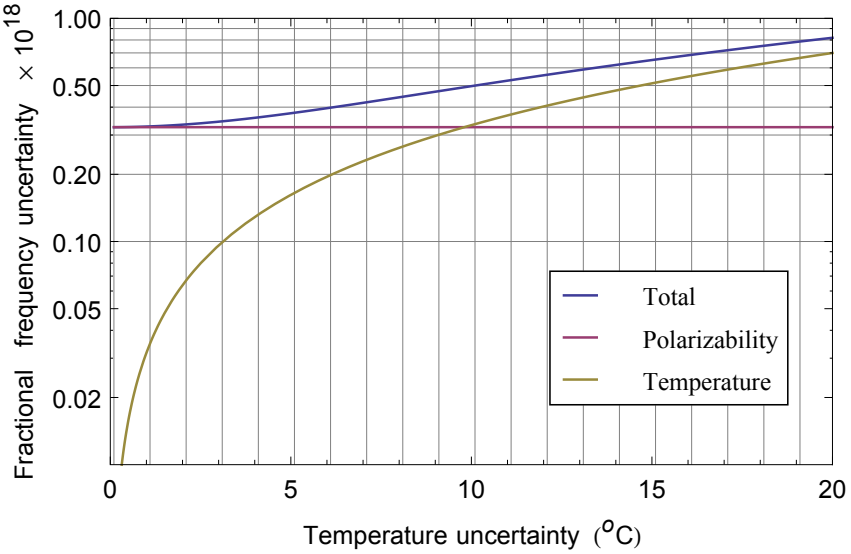

4.4 Zeeman Shift

When an atom experiences a weak, but non-zero magnetic field B, its transition frequency f_0 is approximately perturbed by

$$f - f_0 \simeq C_1 B + C_2 B^2, \tag{4.20}$$

where C_1 and C_2 are coefficients that account for the linear and quadratic Zeeman effects. For the $^{27}Al^+$ optical clock, the linear Zeeman shift can be experimentally canceled during the clock operation on the fly by probing a virtual $m_F = 0$ transition frequency, which is the mean frequency of two stretch Zeeman transitions $|^1S_0,\ F = 5/2,\ m_F = \pm 5/2\rangle \leftrightarrow |^3P_0,\ F = 5/2,\ m_F = \pm 5/2\rangle$ [Bernard 98, Rosenband 07][2] . The coefficient $C_2 = -0.719\,88(48)\,\mathrm{Hz/G^2}$ was measured previously by comparing the clock transition frequencies of $^{27}Al^+$ and $^{199}Hg^+$ while the magnetic field of the $^{27}Al^+$ clock was varied [Rosenband 08]. The clock frequency shift due to the quadratic Zeeman effect in an interrogation cycle is given by [Rosenband 07, Chou 10a]

$$\left(\frac{\delta f}{f}\right) = C_2 \langle B^2 \rangle, \tag{4.21}$$

$$\langle B^2 \rangle = \langle B \rangle^2 + B_{ac}^2. \tag{4.22}$$

Here $\langle B \rangle$ is the time average of the magnetic field at the position of the ion and B_{ac}^2 is the variance of the magnetic field about the mean, which results from the variation of ambient magnetic field. In a linear Paul trap, B_{ac} can be caused by the rf current flowing in the electrodes, which depends on the design of the trap. In our system, we use microwave hyperfine transitions in the ground state $|^2S_{1/2}\rangle$ of $^{25}Mg^+$ as a probe of the magnetic field. The magnetic field dependence of the ground state hyperfine levels of $^{25}Mg^+$ has been studied [Itano 81b]. Given the hyperfine constant and the Landé g-factor, the transition frequencies between different Zeeman levels are calculated

[2] Note that this cancellation works only when the frequency drift rate of each Zeeman transition due to the ambient magnetic field variaion is much smaller than the ratio of the frequency uncertainty and the clock servo time constant, $\delta f/\tau_{clock}$. The two transitions are separated by ≈ 10 kHz at $B \approx 1.1$ Gauss in our experiment.

to the lowest order in B using the Breit-Rabi formula as

$$f\left(|F=3,\, m_F=-3\rangle \leftrightarrow |F=2,\, m_F=-2\rangle\right) \simeq f(B=0) + 2.335\, B, \text{ and} \tag{4.23}$$

$$f\left(|F=3,\, m_F=0\rangle \leftrightarrow |F=2,\, m_F=0\rangle\right) \simeq f(B=0) + (2.194\times 10^{-3})\, B^2, \tag{4.24}$$

where frequency f is in units of MHz and the magnetic field B is in units of Gauss. While $\langle B\rangle$ can be experimentally determined by measuring the linear frequency shift of the transition $|F=3,\, m_F=-3\rangle \leftrightarrow |F=2,\, m_F=-2\rangle$ against the applied magnetic field, B_{ac} is determined by measuring the frequency shift of the transition $|F=3,\, m_F=0\rangle \leftrightarrow |F=2,\, m_F=0\rangle$ versus the applied rf power P_{rf}, where P_{rf} is proportional to B_{ac}^2. As shown in Fig. 4.7, we experimentally find a relation for the wheel trap version C at 76 MHz rf drive frequency

$$10^4 \times B_{ac}^2 = (2.5\pm 0.3) P_{rf} + (9.5\pm 0.9), \tag{4.25}$$

where B_{ac}^2 is in units of Gauss^2 and P_{rf} is in units of Watt. Therefore the estimate of the fractional clock frequency shift is $(\delta f/f) = -(890.7\pm 0.6)\times 10^{-18}$ at $\langle B\rangle \simeq 1.1$ G, limited by the uncertainty of the quadratic Zeeman shift coefficient C_2 of $^{27}\mathrm{Al}^+$.

4.5 Background Gas Collisions

Background gas collisions during the clock interrogation may lead to a frequency shift in two ways: (a) a relative phase shift between the $^{27}\mathrm{Al}^+$ and the probe laser due to the electric field from the background gas molecules and atoms. (b) a time dilation shift due to the kinetic energy transfer between the $^{27}\mathrm{Al}^+$ and the background gas.

One of the challenges for evaluating the effect of background gas collisions is the difficulty of estimating the actual collision rate, since all the ion-based optical clocks operate at a vacuum level where vacuum gauges are unreliable[3] . Fortunately for the $^{27}\mathrm{Al}^+$ optical clock utilizing quantum logic spectroscopy, the order of the ion crystal is sometimes changed by collisions, and the rate of these reordering events can be used as an indirect pressure measurement. As discussed in

[3] We typically operate the clock at a pressure $< 5.0\times 10^{-11}$ torr.

Figure 4.7: Magnetic field variance about the mean versus the trap drive rf power. Red: linear fit to the experimental data, $B_{ac}^2 \times 10^4 = (2.5 \pm 0.3)P_{rf} + (9.5 \pm 0.9)$. The non-vanishing B_{ac} at the zero rf power is due to the ambient fluctuating magnetic field noise, such as that from the 60 Hz currents in nearby electronics.

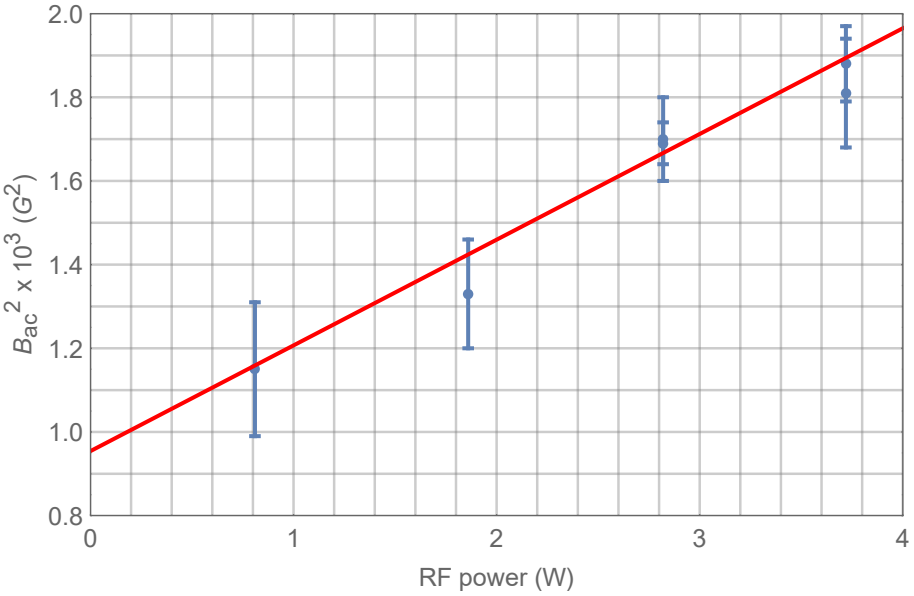

Ref. [Rosenband 08], if we assume the ion-pair reorders if and only if a Langevin collision occurs, the frequency shift due to mechanism (a) has an upper bound of $0.15\,\kappa$ independent of the interrogation pulse duration, where κ is the collision rate [Gioumousis 58]. In Fig. 4.8, the reordering rate of the ion pair within a five-minute time window is plotted against the time after two ions are loaded into the trap. No clear dependence is seen in Fig 4.8, indicating the ion-loading process does not significantly contaminate the vacuum. The mean reordering rate is 0.013 Hz at 40 MHz rf drive frequency, which corresponds to a fractional frequency shift $(\delta f/f) = 3.4 \times 10^{-18}$. However, this shift can be reduced by a factor of two by post-selecting measurements without ion reordering. Furthermore it may also be possible to reject experiments in which there has been a collision that did not cause reordering by performing a temperature measurement on the $^{25}Mg^+$ after the clock interrogation pulse.

With regard to mechanism (b), glancing collisions with impact parameters larger than one Langevin radius may still transfer non-negligible energy to the $^{27}Al^+$ that leads to a time dilation

Figure 4.8: Ion pair reordering rate during the clock operation within a five-minute time window. The x axis is the time after a $^{25}Mg^{+}$-$^{27}Al^{+}$ pair is loaded into the trap. Measurements were done at $\Omega_T \simeq 2\pi \times 40$ MHz and trap parameters are given in Table 3.3.

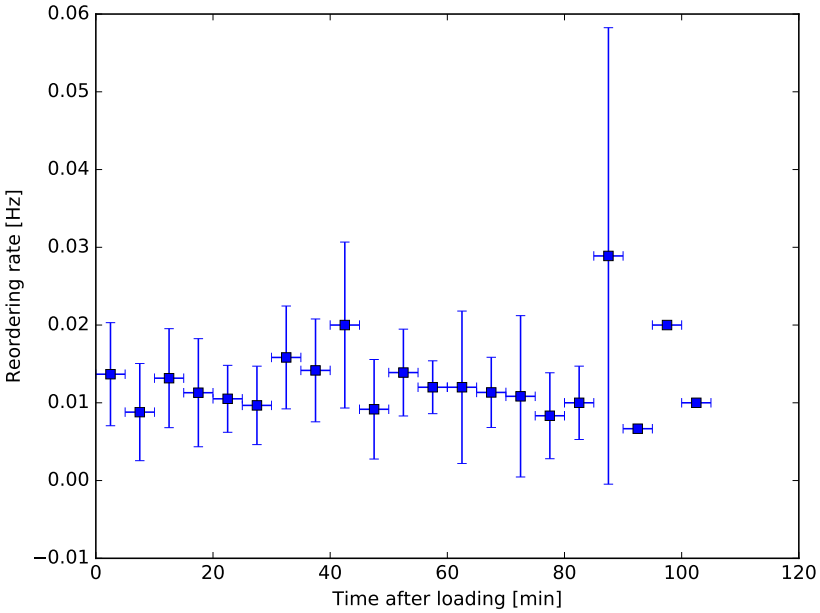

shift. These collisions do not necessarily change the ion order and hence cannot be excluded by the post selection. We are currently working on modeling this effect.

4.6 Stark Shift due to the RF Drive Field

Similar to the BBR, the rf drive field also gives rise to an ac Start shift. Therefore, we can write down the Stark shift due to the rf drive field.

$$\Delta\nu = -\frac{1}{4h}(E^2_{EMM} + E^2_{IMM})\Delta\alpha_{clock}(\Omega_T). \tag{4.26}$$

Following the derivation in Eq. 4.2 and Eq. 4.3, we can obtain the strength of the electric field accounting for the IMM, which is given by

$$\langle E^2_{IMM}\rangle = \sum_{i\subset\{x,y\}}(\frac{1}{2} + \bar{n}_i)\frac{2\hbar\omega_i m_{Al}\Omega_T^2}{Q^2}, \tag{4.27}$$

where ω_i and $\bar{n}_i$ are secular frequencies and average occupation numbers in the transverse direction. With the E_{EMM} values given in Table 4.1 and the average occupation numbers given in Chapter 3, the resulting shift at $\Omega_T \simeq 2\pi \times 40$ MHz is $(\delta f/f) = 1.8 \times 10^{-19}$. In our system, this shift is dominated by the effect of E_{EMM} and the contribution from E_{IMM} is less than 1 %.

4.7 Formation of AlH^+

An essential practical problem for the $^{27}Al^+$ optical clock, though not affecting the accuracy, is the formation of AlH^+ molecular ions. This hydride formation limits the continuous operation of the optical clock because it stops ticking as soon as the molecule forms. The chemical reaction,

$$Al^+ (^1S) + H_2 + 3.8\,eV \longrightarrow AlH^+ (X^2\,\Sigma^+) + H,$$

is known to be endothermic when both the $^{27}Al^+$ and the H_2 are in the electronic ground states [Klein 82, Müller 86, Seck 14]. However when the $^{27}Al^+$ is excited to the metastable state ^3P, the reaction,

$$Al^+ (^3P) + H_2 \longrightarrow AlH^+ (X^2\,\Sigma^+) + H + 0.9\,eV,$$

becomes exothermic. When the clock is operating, we tend to run with the population in the metastable state $^3P_0$ close to 0.5 to reach the quantum projection limit. Thus, Langevin collisions are likely to generate AlH^+ molecules. In addition, the generated hot molecule may be lost from the trap. Currently this is the limitation of the $^{27}Al^+$ clock up time. In Fig. 4.9, we plot the up times of 29 clock runs; the exponential fit gives a lifetime of about 22 minutes. This problem can be resolved by either improving the vacuum or implementing photodissociation of the AlH^+ [Seck 14].

Figure 4.9: Clock up times of 29 experimental runs. Red line is the fit to a exponential function, which give about 22 minutes of lifetime.

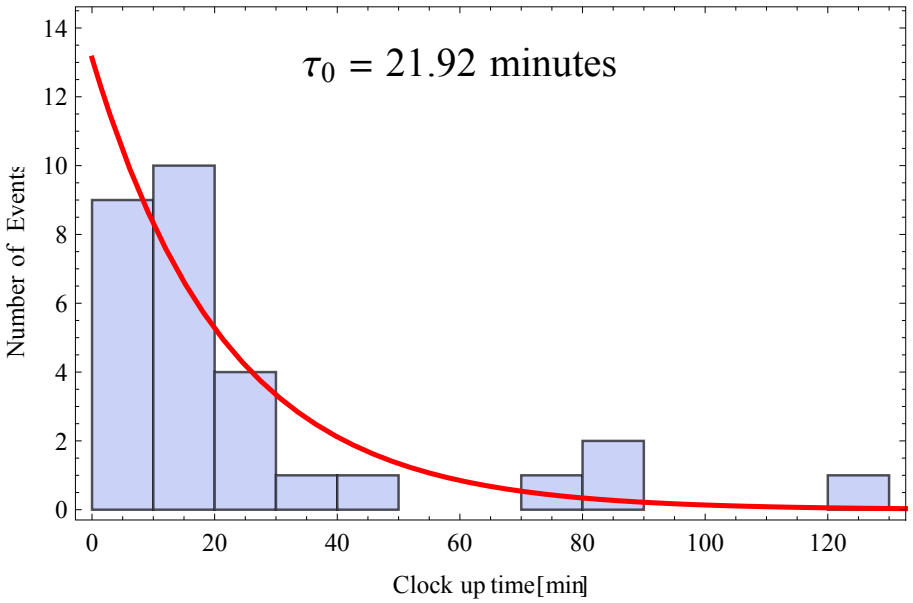

Chapter 5

Conclusion

In this thesis, I have discussed several systematic effects in our current $^{27}Al^+$ clock sympathetically cooled by $^{25}Mg^+$ and utilizing quantum logic spectroscopy. Although the full characterization of the $^{27}Al^+$ optical clock is still ongoing, I would like to summarize some of the most important systematic effects that we have considered so far.

The time dilation shift due to the ion's motion dominated the uncertainty in the previous $^{27}Al^+$ clocks [Rosenband 08, Chou 10a]. The contribution of the secular motion has been reduced more than an order of magnitude in the current system by operating the clock near the 3D motional ground state [Chen 17]. This new protocol also eliminates the need for cooling light during the clock interrogation, which led to an ac Stark shift in the previous clock. We have characterized the secular motion energy at two different rf drive frequencies. In both cases, the secular motion time dilation shift is dominated by the zero-point energy of the harmonic trapping potential at a typical clock interrogation time, which has a definite value and does not contribute significantly to the clock uncertainty. The time dilation shift due to EMM is reduced by a factor of three in the current trap, which is dominated by the EMM-v resulting from the phase imbalance between rf electrodes. Although the shift is of the same order as the previous clock, we do see much less long-term drift of the EMM in contrast to the old clocks. This may be because there is less charge build-up due to implementing laser ablation loading and reducing the amount of dielectric materials in the trap. The current evaluation of the time dilation frequency shift due to EMM is promising and we may be able to control its uncertainty below 1.0×10^{-18}.

With regard to the effect of blackbody radiation due to the ambient environment, an earlier measurement of the polarizability of the clock transition [Chou 11a] coupled with the improved thermal management of the trap shown in this thesis leads to a fractional frequency shift of $-(2.7 \pm 0.3) \times 10^{-18}$. The uncertainty is now dominated by the uncertainty in the value of the polarizability.

The preliminary evaluation of the quadratic Zeeman shift gave a value of $-(890.7 \pm 0.6) \times 10^{-18}$. The uncertainty is reduced by operating the trap at a lower rf drive power, which corresponds to less rf current flowing on the electrode surfaces. This trapping condition leads to relatively smaller secular frequencies and larger Lamb-Dicke parameters, which is a challenge for 3D sideband cooling. An optimized sideband cooling pulse sequence has been developed to make this possible. The uncertainty of the quadratic Zeeman shift is limited by the uncertainty of the coefficient.

The frequency shift due to background gas collisions may be the largest remaining uncertainty of the $^{27}Al^{+}$ optical clock presented in this thesis. The observed reordering rate of the $^{25}Mg^{+}$-$^{27}Al^{+}$ ion pair indicates that the pressure of the current trap is about a factor of 2.5 higher than the previous clocks. This leads to an estimate of the fractional frequency shift uncertainty of 3.4×10^{-18}, arising from the phase shift due to hard collisions with H_2 molecules of impact parameters less than one Langevin radius [Rosenband 08]. A clock operation protocol is being developed to post-select measurements without collisions. In terms of the time dilation shift due to collisions, we are working on modeling this effect to estimate its systematic frequency uncertainty.

There are still some systematic effects in our system that we have not carefully considered so far, such as the AOM frequency chirp, the servo error, and the ac Stark shift caused by the probe laser. However, since the experimental conditions related to these systematic effects are close to the same as those in the previous clocks, I expect that the systematic frequency shifts due to these effects can be controlled to be similar, or at least the same order of magnitude, to the values reported earlier [Chou 10a]. With all these ingredients, the accuracy of the current clock should be below 3.0×10^{-18}. The preliminary uncertainty budget is given in Table 5.1 when the clock is operating at $\Omega_T \simeq 2\pi \times 40$ MHz with 150 ms interrogation time. The uncertainty of the time dilation shift due to EMM is assumed to be 30 % of the shift.

Table 5.1: The preliminary uncertainty budget of the third-generation $^{27}Al^{+}$ clock at the rf drive frequency $\Omega_T \simeq 2\pi \times 40$ MHz with a 150 ms clock interrogation pulse.

Contributor	Fractional frequency $\times 10^{18}$	
	Shift	Uncertainty
Excess micromotion	-3.5	0.9(preliminary)
Secular motion	-1.7	0.3
Blackbody radiation shift	-2.7	0.3
Cooling laser Stark shift	0.0	0.0
Quadratic Zeeman shift	-890.7	0.6(projected)
Linear Doppler shift	0.0	0.3(projected)
Clock laser shift	0.0	0.2(projected)
Background gas collisions	under evaluation	under evaluation
AOM phase chirp	0.0	0.2(projected)

Even as the evaluation of the current $^{27}Al^{+}$ optical clock is being finished, a next generation clock is now being built in our group. It will use a new trap with rf electrodes that have been designed to balance the rf phase to further reduce the EMM. In combination with the protocol developed for sideband cooled clock operation in the current system, we should be able to cut the fractional frequency shift due to time dilation arising from the ion's motion down to the 10^{-19} range. Moreover, the new trap will be housed in a titanium vacuum can, which should reduce the H_2 outgassing rate significantly and minimize the uncertainty due to background gas collisions [Kurisu 08, Takeda 11]. In the next generation clock, it will be exciting to control all the systematic fractional frequency uncertainties near 10^{-19}!

Bibliography

[Allan 66] D. Allan. Statistics of Atomic Frequency Standards. Proc. iEEE, vol. 54, page 1966, 1966.

[Barrett 03] M. D. Barrett, B. DeMarco, T. Schaetz, V. Meyer, D. Leibfried, J. Britton, J. Chiaverini, W. M. Itano, B. Jelenković, J. D. Jost, C. Langer, T. Rosenband & D. J. Wineland. Sympathetic cooling of $^{9}Be^{+}$ and $^{24}Mg^{+}$ for quantum logic. Phys. Rev. A, vol. 68, page 042302, 2003.

[Barwood 14] G. P. Barwood, G. Huang, H. A. Klein, L. A. M. Johnson, S. A. King, H. S. Margolis, K. Szymaniec & P. Gill. Agreement between two $^{88}Sr^{+}$ optical clocks to 4 parts in 10^{17}. Phys. Rev. A, vol. 89, page 050501, 2014.

[Beloy 14] K. Beloy, N. Hinkley, N. B. Phillips, J. A. Sherman, M. Schioppo, J. Lehman, A. Feldman, L. M. Hanssen, C. W. Oates & A. D. Ludlow. Atomic Clock with 1×10^{-18} Room-Temperature Blackbody Stark Uncertainty. Phys. Rev. Lett., vol. 113, page 260801, 2014.

[Beloy 17] K Beloy, David R Leibrandt & Wayne M Itano. Hyperfine-mediated electric quadrupole shifts in Al+ and In+ ion clocks. Physical Review A, vol. 95, no. 4, page 043405, 2017.

[Bergquist 87] JC Bergquist, Wayne M Itano & DJ Wineland. Recoilless optical absorption and Doppler sidebands of a single trapped ion. Physical Review A, vol. 36, no. 1, page 428, 1987.

[Berkeland 98] D. J. Berkeland, J. D. Miller, J. C. Bergquist, W. M. Itano & D. J. Wineland. Minimization of Ion Micromotion in a Paul trap. J. Appl. Phys., vol. 83, page 5025, 1998.

[Bernard 98] J. E. Bernard, L. Marmet & A. A. Madej. A laser frequency lock referenced to a single trapped ion. Opt. Commun., vol. 150, page 170, 1998.

[Bloom 14] B. J. Bloom, T. L. Nicholson, J. R. Williams, S. L. Campbell, M. Bishof, X. Zhang, W. Zhang, S. L. Bromley & J. Ye. An optical lattice clock with accuracy and stability at the 10^{18} level. Nature, vol. 506, pages 71–75, 2014.

[Bondarescu 15] Ruxandra Bondarescu, Andreas Schärer, Andrew Lundgren, György Hetényi, Nicolas Houlié, Philippe Jetzer & Mihai Bondarescu. Atomic clocks as a tool to monitor vertical surface motion. Geophys. J. Int., vol. 202, page 1770, 2015.

[Boyd 68] G. D. Boyd & D. A. Kleinman. Parametric Interaction of Focused Gaussian Light Beams. J. Appl. Phys., vol. 39, page 3597, 1968.

[Boyd 07] Martin M. Boyd, Andrew D. Ludlow, Sebastian Blatt, Seth M. Foreman, Tetsuya Ido, Tanya Zelevinsky & Jun Ye. ^{87}Sr Lattice Clock with Inaccuracy below 10^{-15}. Phys. Rev. Lett., vol. 98, page 083002, 2007.

[Brownnutt 15] M Brownnutt, M Kumph, P Rabl & R Blatt. Ion-trap measurements of electric-field noise near surfaces. Reviews of Modern Physics, vol. 87, no. 4, page 1419, 2015.

[Chen 17] J.-S. Chen, S. M. Brewer, C. W. Chou, D. J. Wineland, D. R. Leibrandt & D. B. Hume. Sympathetic Ground State Cooling and Time-Dilation Shifts in an $^{27}Al^{+}$ Optical Clock. Phys. Rev. Lett., vol. 118, page 053002, Jan 2017.

[Chou 10a] C. W. Chou, D. B. Hume, J. C. J. Koelemeij, D. J. Wineland & T. Rosenband. Frequency Comparison of Two High-Accuracy Al^{+} Optical Clocks. Phys. Rev. Lett., vol. 104, page 070802, 2010.

[Chou 10b] C. W. Chou, D. B. Hume, T. Rosenband & D. J. Wineland. Optical Clocks and Relativity. Science, vol. 329, page 1630, 2010.

[Chou 11a] C. W. Chou et al. Measurement of the bbr shift on Al^{+} clock transition using a laser beam. private communication, 2011.

[Chou 11b] C. W. Chou, D. B. Hume, M. J. Thorpe, D. J. Wineland & T. Rosenband. Quantum Coherence between Two Atoms beyond Q = 10^{15}. Phys. Rev. Lett., vol. 106, page 160801, 2011.

[Chuah 13] Boon Leng Chuah, Nicholas C. Lewty, Radu Cazan & Murray D. Barrett. Minimization of Ion Micromotion in a Linear Paul Trap with a High Finesse Cavity. Opt. Express, vol. 21, page 10632, 2013.

[Colombe 14] Y. Colombe, D. H. Slichter, A. C. Wilson, D. Leibfried & D. J. Wineland. Single-Mode Optical Fiber for High-Power, Low-Loss UV Transmission. Opt. Express, vol. 22, pages 19783–19793, 2014.

[Daniilidis 11] D. Daniilidis, S. Narayanan, S. A. Möller, C. Clark, T. E. Lee, P.J. Leek, A. Wallraff, St. Schulz, F. Schmidt-Kaler & H. Häffner. Fabrication and heating rate study of microscopic surface electrode ion traps. New J. Phys., vol. 13, page 013032, 2011.

[de Mirandés 16] E. de Mirandés, P. Barat, M. Stock & M. J. T. Milton. Calibration campaign against the international prototype of the kilogram in anticipation of the redefinition of the kilogram, part II: evolution of the BIPM as-maintained mass unit from the 3rd periodic verification to 2014. Metrologia, vol. 53, page 1204, 2016.

[Degenhardt 05] Carsten Degenhardt, Hardo Stoehr, Christian Lisdat, Guido Wilpers, Harald Schnatz, Burghard Lipphardt, Tatiana Nazarova, Paul-Eric Pottie, Uwe Sterr, Jürgen Helmcke & Fritz Riehle. Calcium optical freqeuncy standard with ultracold atoms: Approaching 10^{-15} relative uncertainty. Phys. Rev. A, vol. 72, page 062111, 2005.

[Dehmelt 82] H. Dehmelt. Monoion oscillator as potential ultimate laser frequency standard. IEEE Trans. Instrum. Meas., vol. IM-31, pages 83–87, 1982.

[Delva 17] P. Delva, J. Lodewyck, S. Bilicki, E. Bookjans, G. Vallet et al. Test of special relativity using a fiber network of optical clocks. arXiv:1703.04426, 2017.

[Derevianko 14] A. Derevianko & M. Pospelov. Hunting for topological dark matter with atomic clocks. Nature Phys., vol. 10, page 933, 2014.

[DiCiccio 96] T. J. DiCiccio & B. Efron. Bootstrap Confidence Intervals. Statist. Sci., vol. 11, page 189, 1996.

[Dicke 53] R. H. Dicke. The effect of collisions upon the Doppler width of spectral lines. Phys. Rev., vol. 89, page 472, 1953.

[Diedrich 89] F. Diedrich, J. C. Bergquist, Wayne M. Itano & D. J. Wineland. Laser Cooling to the Zero-Point Energy of Motion. Phys. Rev. Lett., vol. 62, page 403, 1989.

[Dodonov 00] V. V. Dodonov, S. S. Mizrahi & A. L. de Souza Silva. Decoherence and Thermalization Dynamics of a Quantum Oscillator. J. Opt. B: Quantum Semiclass. Opt., vol. 2, page 271, 2000.

[Dolezăl 15] M. Dolezăl, P. Balliing, P. B. R. Nisbet-Jones, S. A. King, J. M. Jones, H. A. Klein, P. Gill, T. Lindvall, A. E. Wallin, M. Merimaa, C. Tamm, C. Sanner, N. Huntemann, N. Schanhorst, I. D. Leroux, P. O. Schmidt, T. Burgermeister, T. E. Mehlstäubler & E. Peik. Analysis of thermal radiation in ion traps for optical frequency standards. Metrologia, vol. 52, page 842, 2015.

[Donley 05] EA Donley, TP Heavner, F Levi, MO Tataw & SR Jefferts. Double-pass acousto-optic modulator system. Review of Scientific Instruments, vol. 76, no. 6, page 063112, 2005.

[Drever 83] R. W. P. Drever, J. L. Hall, F. V. Kowalski, J. Hough, G. M. Ford, Munley A. J. & H. Ward. Laser phase and frequenccy stabilization using an optical resonator. Appl. Phys. B, vol. 31, page 97, 1983.

[Drullinger 80] R. E. Drullinger, D. J. Wineland & J. C. Bergquist. High-Resolution Optical Spectra of Laser Cooled Ions. Appl. Phys., vol. 22, page 365, 1980.

[Dubé 15] Pierre Dubé, Alan A. Madej, Andrew Shiner & Bin Jian. $^{88}Sr^{+}$. Phys. Rev. A, vol. 92, page 042119, 2015.

[Dzuba 99] V. A. Dzuba, V. V. Flambaum & J. K. Webb. Calculations of the relativistic effects in many-electron atoms and space-time variation of fundamental constants. Phys. Rev. A, vol. 59, pages 230–237, 1999.

[Ejtemaee 16] S. Ejtemaee & P. C. Haljan. 3D Sisyphus Cooling of Trapped Ions. arXiv:1603.01248, 2016.

[Flambaum 16] V. V. Flambaum. Enhancing the Effect of Lorentz Invariance and Einstein's Equivalence Principle Violation in Nuclei and Atoms. Phys. Rev. Lett., vol. 117, page 072501, 2016.

[Fortier 11] T. M. Fortier, M. S. Kirchner, F. Quinlan, J. Taylor, J. C. Bergquist, T. Rosenband, N. Lemke, A. Ludlow, Y. Jiang, C. W. Oates & S. A. Diddams. Generation of ultrastable microwaves via optical frequency division. Nat. Photon., vol. 5, page 425, 2011.

[Fröhlich 07] B Fröhlich, T Lahaye, B Kaltenhäuser, H Kübler, S Müller, T Koch, M Fattori & T Pfau. Two-frequency acousto-optic modulator driver to improve the beam pointing stability during intensity ramps. Review of scientific instruments, vol. 78, no. 4, page 043101, 2007.

[Gaebler 16] J. P. Gaebler, T. R. Tan, Y. Lin, Y. Wan, R. Bowler, A. C. Keith, S. Glancy, K. Coakley, E. Knill, D. Leibfried & D. J. Wineland. High-Fidelity Universal Gate Set for $^{9}Be^{+}$ Ion Qubits. Phys. Rev. Lett, vol. 117, page 060505, 2016.

[Gallagher 79] T. F. Gallagher & W. E. Cooke. Interactions of Blackbody Radiation with Atoms. Phys. Rev. Lett., vol. 42, page 835, 1979.

[Gesley 85] M. A. Gesley & L. W. Swanson. Spectral analysis of adsorbate induced field-emission flicker noise. Phys. Rev. B, vol. 32, page 7703, 1985.

[Ghosh 95] P.K. Ghosh. Ion traps. International series of monographs on physics. Clarendon Press, 1995.

[Gill 11] Patrick Gill. When should we change the definition of the second? Phil. Trans. R. Soc. A, vol. 369, page 4109, 2011.

[Gioumousis 58] G. Gioumousis & D. P. Stevenson. Reactions of Gaseous Molecule Ions with Gaseous Molecules. V. Theory. J. Chem. Phys., vol. 29, page 294, 1958.

[Gloger 15] Timm F. Gloger, Peter Kaufmann, Delia Kaufmann, M. Tanveer Baig, Thomas Collath, Michael Johanning & Christof Wunderlich. Ion trajectory analysis for micromotion miimization and the measurement of small forces. Phys. Rev. A, vol. 92, page 043421, 2015.

[Godun 14] R. M. Godun, P. B. R. Nisbet-Jones, J. M. Jones, S. King, L. A. M. Johnson, H. S. Margolis, K. Szymaniec, , S. N. Lea, K. Bongs & P. Gill. Frequency ratio of two optical clok transitions in $^{171}Yb^{+}$ and constraints on the time-variation of fundamental constants. Phys. Rev. Lett., vol. 113, page 210801, 2014.

[Gürtler 04] A. Gürtler, F. Robicheaux, W. J. van der Zande & L. D. Noordam. Asymmetry in the Strong-Field Ionization of Rydberg Atoms by Few-Cycle Pulses. Phys. Rev. Lett., vol. 92, page 033002, 2004.

[Heavner 14] Thomas P Heavner, Elizabeth A Donley, Filippo Levi, Giovanni Costanzo, Thomas E Parker, Jon H Shirley, Neil Ashby, Stephan Barlow & S R Jefferts. First accuracy evaluation of NIST-F2. Metrologia, vol. 51, no. 3, page 174, 2014.

[Hendricks 07] R. J. Hendricks, D. M. Grant, P. F. Herskind, A. Dantan & M. Drewsen. An all-optical ion-loading technique for scalable microtrap architectures. Appl. Phys. B, vol. 88, pages 507–513, 2007.

[Hinkley 13] N. Hinkley, J. A. Sherman, N. B. Phillips, M. Schipoppo, N. D. Lemke, K. Beloy, M. Pizzocaro, C. W. Oates & A. D. Ludlow. An atomic clock with 10^{-18} instability. Science, vol. 341, page 1215, 2013.

[Hite 12] D. A. Hite, Y. Colombe, A. C. Wilson, K. R. Brown, U. Warring, R. Jördens, J. D. Jost, K. S. McKay, D. P. Pappas, D. Leibfried & D. Wineland. 100-Fold Reduction of Electric-Field Noise in an Ion Trap Cleaned with *In Situ* Argon-Ion-Beam Bombardment. Phys. Rev. Lett., vol. 109, page 103001, 2012.

[Hume 07] D. B. Hume, T. Rosenband & D. Wineland. High-fidelity adaptive qubit detection through repetitive quantum nondemotion measurement. Phys. Rev. Lett., vol. 99, page 120502, 2007.

[Hume 10] D. B. Hume. Two-Species Ion Arrays for Quantum Logic Spectroscopy and Entanglement Generation. PhD thesis, University of Colorado, Boulder, 2010.

[Hume 16] D. B. Hume & D. R. Leibrandt. Probing beyond the Laser Coherence Time in Optical Clock Comparisons. Phys. Rev. A, vol. 93, page 032138, 2016.

[Huntemann 14] N. Huntemann, B. Lipphardt, Chr. Tamm, V. Gerginov, S. Weyers & E. Peik. Improved Limit on a Temporal Variation of m_p/m_e from Comparisons of Yb^+ and Cs Atomic Clocks. Phys. Rev. Lett., vol. 113, page 210802, 2014.

[Huntemann 16] N. Huntemann, C. Sanner, B. Lipphardt, Chr. Tamm & E. Peik. Single-Ion Atomic Clock with 3×10^{-18} Systematic Uncertainty. Phys. Rev. Lett., vol. 116, page 063001, 2016.

[Itano 81a] W. M. Itano, L. L. Lewis & D. J. Wineland. Shift of $^2S_{1/2}$ hyperfine splittings due to blackbody radiation and its influence on frequency standards. J. de Phys., vol. Colloque C8, page 283, 1981.

[Itano 81b] Wayne M. Itano & D. J. Wineland. Precision measurement of the ground-state hyperfine constant of $^{25}Mg^+$. Phys. Rev. A, vol. 24, page 1364, 1981.

[Itano 82] W. M Itano & D. J. Wineland. Laser Cooling of Ions Stored in Harmonic and Penning Traps. Phys. Rev. A, vol. 25, page 35, 1982.

[Itano 93] W. M. Itano, J. C. Bergquist, J. J. Bollinger, J. M. Gilligan, D. J. Heinzen, F. L. Moore, M. G. Raizen & D. J. Wineland. Quantum Projection noise: Pupulation fluctuation in two-level systems. Phys. Rev. A, vol. 47, page 3554, 1993.

[James 98] D. F. James. Theory of Heating of the Quantum Ground State of Trapped Ions. Phys. Rev. Lett., vol. 81, page 317, 1998.

[Jefferts 95] S. R. Jefferts, C. Monroe, E. W. Bell & D. J. Wineland. Coaxial-resonator-driven rf (Paul) trap for strong confinement. Phys. Rev. A, vol. 51, page 3112, 1995.

[Jefferts 07] S. R. Jefferts, T. P. Heavner, T. E. Parker & J. H. Shirley. NIST Cesium Fountains Current Status and Future Prospects. Proc. SPIE, vol. 6673, page 667309, 2007.

[Johansson 12] J. R. Johansson, P. D. Nation & F. Nori. QuTiP: An open-source Python framework for the dynamics of open quantum systems. Comp. Phys. Comm., vol. 183, page 1760, 2012.

[Johansson 13] J. R. Johansson, P. D. Nation & F. Nori. QuTiP 2: A Python framework for the dynamics of open quantum systems. Comp. Phys. Comm., vol. 184, page 1234, 2013.

[Keller 15] J. Keller, H. L. Partner, T. Burgermeister & T. E. Mehlstäubler. Precise Determination of Micromotion for Trapped-Ion Optical Clocks. J. Appl. Phys., vol. 118, page 104501, 2015.

[Kim 17] E. Kim, A. Safavi-Naini, D. A. Hite, K. S. McKay, D. P. Pappas, P. F. Weck & H. R. Sadeghpour. Electric-field noise from carbon-adatom diffusion on a Au(110) surface: First-rpinciples calculations and experiments. Phys. Rev. A, vol. 95, page 033407, 2017.

[Klein 82] R. Klein, P. Rosmus & H. J. Werner. Ab initio calculations of low lying states of the BH^+ and AlH^+ ions. J. Chem. Phys., vol. 77, page 3559, 1982.

[Kobayashi 06] J Kobayashi, Y Izumi, M Kumakura & Y Takahashi. Stable all-optical formation of Bose–Einstein condensate using pointing-stabilized optical trapping beams. Applied Physics B: Lasers and Optics, vol. 83, no. 1, pages 21–25, 2006.

[Kurisu 08] H. Kurisu, K. Ishizawa, S. Yamamoto, M. Hesaka & Y. Saito. Application of titanium materials to vacuum chambers and components. J. Phys.: Conf. Ser., vol. 100, page 092002, 2008.

[Le Targat 13] R Le Targat, L Lorini, Y Le Coq, M Zawada, J Guéna, M Abgrall, M Gurov, P Rosenbusch, DG Rovera, B Nagórny et al. Experimental realization of an optical second with strontium lattice clocks. Nature communications, vol. 4, 2013.

[Lechner 16] Regina Lechner, Christine Maier, Cornelius Hempel, Peter Jurcevic, Ben P. Lanyon, Thomas Monz, Michael Brownnutt, Rainer Blatt & Christian F. Roos. Electromagnetically-induced-transparency ground-state cooling of long ion strings. Phys. Rev. A, vol. 93, page 053401, 2016.

[Leibrandt 15] D. R. Leibrandt & J. Heidecker. An open source digital servo for atomic, molecular, and optical physics experiments. Rev. Sci. Instrum., vol. 86, page 123115, 2015.

[Lemke 09] N. D. Lemke, A. D. Ludlow, Z. W. Barber, T. M. Fortier, S. A. Diddams, Y. Jiang, S. R. Jefferts, T. P. Heavner, T. E. Parker & C. W. Oates. Spin-1/2 Optical Lattice Clock. Phys. Rev. Lett., vol. 103, page 063001, 2009.

[Li 00] Ying Ze Li, C. V. Madhusudana & Eddie Leonardi. Enhancement of Thermal Contact Conductance: Effect of Metallic Coating. J. Thermophys. Heat Transfer, vol. 14, page 540, 2000.

[Lin 13] Y. Lin, J. P. Gaebler, T. R. Tan, R. Bowler, J. D. Jost, D. Leibfried & D. J. Wineland. Sympathetic Electromagnetically-Induced-Transparency Laser Cooling of Motional Modes in an Ion Chain. Phys. Rev. Lett., vol. 110, page 153002, 2013.

[Lombardi 07] M. A. Lombardi, T. P. Heavner & S. R. Jefferts. NIST Primary Frequency Standards and the Realization of the SI Seconde. NCSLI Measure, vol. 2, pages 74–89, 2007.

[Ludlow 08] A. D. Ludlow, T. Zelevinsky, G. K. Campbell, S. Blatt, M. M. Boyd, M. H. G. de Miranda, M. J. Martin, J. W. Thomsen, S. M. Foreman, Jun Ye, T. M. Fortier, J. E. Stalnaker, S. A. Diddams, Y. Le Coq, Z. W. Barber, N. Poli, N. D. Lemke, K. M. Beck & C. W. Oates. Sr Lattice Clock at 1 x 10–16 Fractional Uncertainty by Remote Optical Evaluation with a Ca Clock. Science, vol. 319, page 1805, 2008.

[Ludlow 15] A. D. Ludlow, M. M. Boyd, J. Ye, E. Peik & P. O. Schmidt. Optical Atomic Clocks. Rev. Mod. Phys., vol. 87, page 637, 2015.

[Ma 94] L. S. Ma, P. Jungner, J. Ye & J. L. Hall. Delivering the same optical frequency at two places: acccurate cancellation of phase noise introduced by an optical fiber or other time-varying path. Opt. Lett., vol. 19, pages 1777–1779, 1994.

[Major 07] F. G. Major. The quantum beat: principles and applicationos of atomic clocks. Springer, 2007.

[Maleki 05] Lute Maleki & John Prestage. Applications of clocks and frequency standards: from the routine to tests of fundamental models. Metrologia, vol. 42, page S145, 2005.

[Manfredi 12] G. Manfredi & P.-A Hervieux. Adiabatic Cooling of Trapped Non-Neutral Plasmas. Phys. Rev. Lett., vol. 109, page 255005, 2012.

[Margolis 04] H. S. Margolis, G. P. Barwood, G. Huang, H. A. Klein, S. N. Lea, K. Szymaniec & P. Gill. Hertz-Level Measurement of the Optical Clock Frequency in a Single 88Sr+ Ion. Science, vol. 306, no. 5700, pages 1355–1358, 2004.

[Marquet 03] C. Marquet, F. Schmidt-Kaler & D. F. V. James. Phonon-phonon interactions due to non-linear effects in a linear ion trap. Appl. Phys. B, vol. 76, pages 199–208, 2003.

[Mitroy 09] J. Mitroy, J. Y. Zhang, M. W. J. Bromley & K. G. Rollin. Blackbody radiation shift of the Al^+ clock transition. Eur. Phys. J. D, vol. 53, page 15, 2009.

[Monroe 95] C. Monroe, D. M. Meekhof, B. E. King, S. R. Jefferts, W. M. Itano, D. J. Wineland & P Gould. Resolved-Sideband Raman Cooling of a Bound Atom to the 3D Zero-Point Energy. Phys. Rev. Lett., vol. 75, page 4011, 1995.

[Müller 86] B. Müller & Ch. Ottinger. Chemiluminescent reactions of second-row atomic ions.I. $Al^+ + H_2 \rightarrow AlH^+(A^2\Pi, B^2\Sigma^+) + H$. J. Chem. Phys., vol. 85, page 232, 1986.

[Nemitz 16] Nils Nemitz, Takuya Ohkubo, Masao Takamoto, Ichiro Ushijima, Manoj Das, Noriaki Ohmae & Hidetoshi katori. Frequency ratio of Yb and Sr clocks with 5×10^{17} uncertainty at 150seconds averaging time. Nat. Photon., vol. 10, page 258, 2016.

[Nicholson 15] T. L. Nicholson, S. L. Campbell, R. B. Hutson, G. E. Marti, B. J. Bloom, R. L. McNally, W. Zhang, M. D. Barrett, M. S. Safronova, G. F. Strouse, W. L. Tew & J. Ye. Systematic Evaluation of an Atomic Clock at 2×10^{-18} Total Uncertainty. Nat. Commun., vol. 6, page 6896, 2015.

[Niering 00] M. Niering, R. Holzwarth, J. Reichert, P. Pokasov, Th. Udem, M. Weitz, T. W. Hänsch, P. Lemonde, G. Santarelli, M. Abgrall, P. Laurent, C. Salomon & A. Clairon. Measurement of the Hydrogen $1S$- $2S$ Transition Frequency by Phase Coherent

Comparison with a Microwave Cesium Fountain Clock. Phys. Rev. Lett., vol. 84, pages 5496–5499, 2000.

[Nisbet-Jones 16] P. B. R. Nisbet-Jones, S. A. King, J. M. Jones, R. M. Godun, C. F. A. Baynham, K. Bongs, Doležal M., P. Balling & P. Gill. A Single-Ion Trap with Minimized Ion-Environment Interactions. Appl. Phys. B, vol. 122, page 57, 2016.

[Oskay 06] W. H. Oskay, S. A. Diddams, E. A. Donley, T. M. Fortier, T. P. Heavner, L. Hollberg, W. M. Itano, S. R. Jefferts, M. J. Delaney, K. Kim, F. Levi, T. E. Parker & J. C. Bergquist. Single-Atom Optical Clock with High Accuracy. Phys. Rev. Lett., vol. 97, page 020801, 2006.

[Ozeri 07] R. Ozeri, W. M. Itano, R. B. Blakestad, J. Britton, J. Chiaverini, J. D. Jost, C. Langer, D. Leibfried, R. Reichle, S. Seidelin, J. H. Wesenberg & D. J. Wineland. Errors in Trapped-Ion Quantum Gates due to Spontaneous Photon Scattering. Phys. Rev. A, vol. 75, page 042329, 2007.

[Park 08] C. D. Park, S. M. Chung, Xianghong Liu & Yulin Li. Reduction in hydrogen outgassing from stainless steels by a medium-temperature heat treatment. J. Vac. Sci. Technol. A, vol. 26, page 1166, 2008.

[Poitzsch 96] M. E. Poitzsch, J. C. Bergquist, W. M. Itano & D. J. Wineland. Cryogenic linear ion trap fro accurate spectroscopy. Rev. Sci. Instrum., vol. 67, page 129, 1996.

[Porsev 06] Sergey G. Porsev & Andrei Dereviando. Multipolar theory of blackbody radiation shift of atomic energy levels and its implications for optical lattice clock. Phys. Rev. A, vol. 74, page 020502(R), 2006.

[Poulsen 12a] G. Poulsen, Y. Miroshnychenko & M. Drewsen. Efficient Ground-State Cooling of an Ion in a Large Room-Temperature Linear Paul Trap with a sub-Hertz Heating Rate. Phys. Rev. A, vol. 86, page 051402(R), 2012.

[Poulsen 12b] Gregers Poulsen & Michael Drewsen. Adiabatic cooling of a single trapped ion. arXiv:1210.4309, 2012.

[Prestage 09] J. Prestage, S. Chung, R. Thompson & P. MacNeal. Progress on small mercury ion clock for space applications. In Proc. IFCS wiht 22nd EFTF, page 54, 2009.

[Pyka 13] K. Pyka, N. Herschbach, J. Keller & T. E. Mehlstäubler. A High-Precision SegmentedPaul Trap with Minimized Micromotioin for an Optical Multiple-Ion Clock. Appl. Phys. B, vol. 114, pages 231–241, 2013.

[Quessada 03] Audrey Quessada, Richard P. Kovacich, Irène Courtillot, André Clairon, Giorgio Santarelli & Pierre Lemonde. The Dick effect for an optical frequency standard. J. Opt. B: Quantum Semiclass. Opt., vol. 5, page S150, 2003.

[Quinn 84] TJ Quinn. Documents concerning the definition of the metre. Metrologia, vol. 19, no. 4, pages 163–177, 1984.

[Raizen 92] M. G. Raizen, J. M. Gilligan, J. C. Bergquist, W. M. Itano & D. J. Wineland. Ionic Crytal in a Linear Paul Trap. Phys. Rev. A, vol. 45, page 6493, 1992.

[Ramsey 85] N. F. Ramsey. Molecular beams. Oxford University Press, 1985.

[Richard 16] P. Richard, H. Fang & R. David. Foundation for the redefinition of the kilogram. Metrologia, vol. 53, page A6, 2016.

[Riehle 17] Fritz Riehle. Optical clock networks. Nat. Photon., vol. 11, page 25, 2017.

[Riley 08] W. J. Riley. Handbook of frequency stabillity analysis. NIST Special Publication 1065, 2008.

[Roos 00] C. F. Roos, D. Leibfried, A. Mundt, F. Schmidt-Kaler, J. Eschner & R. Blatt. Experimental Demonstration of Ground State Laser Cooling with Electromagnetically Induced Transparency. Phys. Rev. Lett., vol. 85, page 5547, 2000.

[Rosenband 06] T. Rosenband, W. M. Itano, P. O. Schmidt, D. B. Hume, J. C. J. Koelemeij, J. C. Bergquist & D. J. Wineland. Blackbody radiation shift of the $^{27}Al^{+}$ $^{1}S_0$-$^{3}P_0$ transition. In Proc. EFTF Conf., page 289, 2006.

[Rosenband 07] T. Rosenband, P. O. Schmidt, D. B. Hume, T. M. Itano W. M. an Fortier, J. E. Stalnaker, K. Kim, S. A. Diddams, J. C. J. Koelemeij, J. C. Bergquist & D. J. Wineland. Observation of the $^{1}S_0 \rightarrow^{3} P_0$ Clock Transition in $^{2}7Al^{+}$. Phys. Rev. Lett., vol. 98, page 220801, 2007.

[Rosenband 08] T. Rosenband, D. B. Hume, P. O. Schmidt, C. W. Chou, A. Brusch, L. Lorini, W. H. Oskay, R. E. Drullinger, T. M. Fortier, J. E. Stalnaker, S. A. Diddams, W. C. Swann, N. R. Newbury, W. M. Itano, D. J. Wineland & J. C. Bergquist. Frequency Ratio of Al^{+} and Hg^{+} Single-Ion Optical Clocks; Metrology at the 17th Decimal Place. Science, vol. 319, page 1808, 2008.

[Rowe 02] M. A. Rowe, A. Ben-Kish, B. DeMarco, D. Leibfried, V. Meyer, J. Beall, J. Britton, J. Hughes, W. M. Itano, B. Jelenkovic, C. Langer, T. Rosenband & D. J. Wineland. Transport of quantum states and separation of ions in a dual rf ion trap. Quantum Information and Computation, vol. 2, pages 257–271, 2002.

[Safavi-Naini 11] A. Safavi-Naini, P. Rabi, P. F. Weck & H. R. Sadeghpour. Microscopic model of electric-field-noise heating in ion traps. Phys. Rev. A, vol. 84, page 023412, 2011.

[Safronova 11] M. S. Safronova, M. G. Kozlov & Charles W. Clar. Precision Calculation of Blackbody Radiation Shifts for Optical Frequency Metrology. Phys. Rev. Lett., vol. 107, page 143006, 2011.

[Schioppo 17] M. Schioppo, R. C. Brown, W. F. McGrew, N. Hinkley, R. J. Fasano et al. Ultrastable optical clock with two cold-atom ensembles. Nat. Photon., vol. 11, page 48, 2017.

[Schmidt 05] P. O. Schmidt, T. Rosenband, C. Langer, W. M. Itano, J. C. Bergquist & D. J. Wineland. Spectroscopy Using Quantum Logic. Science, vol. 309, pages 749–752, 2005.

[Seck 14] C. S. Seck, E. G. Hohenstein, C.-Y. Lien & B. C. Stollenwerk P. R. adn Odom. Rotational State analysis of AlH^+ by Two-Photon Dissociation. J. Mol. Spectrosc., vol. 300, page 108, 2014.

[Sheridan 11] K. Sheridan, W. Lange & M. Keller. All-optical ion generation for ion trap loading. Appl. Phys. B, vol. 104, pages 755–761, 2011.

[Sherman 12] J. A. Sherman, N. D. Lemke, N. Hinkley, M. Pizzocaro, R. W. Fox, A. D. Ludlow & C. W. Oates. High-Accuracy Measurement of Atomic Poloarizability in an Optical Lattice Clock. Phys. Rev. Lett., vol. 108, page 153002, 2012.

[Simon 98] E. Simon, P. Laurent & A. Clairon. Measurement of the Stark shift of the Cs hyperfine splitting in an atomic fountain. Phys. Rev. A, vol. 57, page 436, 1998.

[Skuja 01] L. Skuja, H. Hosona & M. Hirano. Laser-induced color centers in silica. Proc. SPIE, vol. 4347, pages 155–168, 2001.

[Snyder 75] JJ Snyder. Paraxial ray analysis of a cat's-eye retroreflector. Applied optics, vol. 14, no. 8, pages 1825–1828, 1975.

[Stenger 01] Jörn Stenger, Christian Tamm, Nils Haverkamp, Stefan Weyers & Harald R. Telle. Absolute frequency measurement of the 435.5-nm $^{171}Yb^+$-clock transition with a Kerr-lens mode-locked femtosecond laser. Opt. Lett., vol. 26, no. 20, pages 1589–1591, 2001.

[Sterr 04] U. Sterr, C. Degenhardt, H. Stoehr, Ch. Lisdat, H. Schnatz, J. Helmcke, F. Riehle, G. Wilpers, Ch. Oates & L. Hollberg. The optical calcium frequency standards of PTB and NIST. C. R. Physique, vol. 5, page 8, 2004.

[Takano 16] Tetsushi Takano, Masao Takamoto, Ichiro Ushijima, Noriaki Ohmae, Tomoya Akatsuka et al. Geopotential measurements with synchronously linked optical lattice clocks. Nat. Photon., vol. 10, page 662, 2016.

[Takeda 11] Masatoshi Takeda, Hiroki Kurisu, Setsuo Yamamoto, Hamazo Nakagawa & Katsunobu Ishizawa. Hydrogen outgassing mechanism in titanium materials. Appl. Surf. Sci., vol. 258, page 1405, 2011.

[Taylor 08] Barry N. Taylor & Ambler Thompson, editeurs. The international system of units (si). National Institute of Standards and Technology, 2008. This is the English translation of the BIPM SI Brochure in French, entitled "*Le Système Internatioinal d' Unités*".

[Turchette 00a] Q. A. Turchette, D. Kielpinski, B. E. King, D. Leibfried, D. M. Meekhof, C. J. Myatt, M. A. Rowe, W. M. Itano, C. Monroe & D. J. Wineland. Heating of trapped ions from the quantum ground state. Phys. Rev. A, vol. 61, page 063418, 2000.

[Turchette 00b] Q. A. Turchette, C. J. Myatt, B. E. King, C. A. Sackett, D. Kielpinski, W. M. Itano, C. Monroe & D. J. Wineland. Decoherence and Decay of Motional Quantum States of a Trapped Atom Coupled to Engineered Reservoirs. Phys. Rev. A, vol. 62, page 053807, 2000.

[Udem 01] Th. Udem, S. A. Diddams, K. R. Vogel, C. W. Oates, E. A. Curtis, W. D. Lee, W. M. Itano, R. E. Drullinger, J. C. Bergquist & L. Hollberg. Absolute Frequency Measurements of the Hg^+ and Ca Optical Clock Transitions with a Femtosecond Laser. Phys. Rev. Lett., vol. 86, pages 4996–4999, May 2001.

[Ushijima 15] Ichiro Ushijima, Masao Takamoto, Manoj Das, Takuya Ohkubo & Hidetoshi Katori. Cryogenic optical lattice clocks. Nat. Photon., vol. 9, page 185, 2015.

[van Ingen 96] R. P. van Ingen. Detection of electricfieldionized Rydberg atoms originating from laser ablation of Si. J. Appl. Phys., vol. 79, page 467, 1996.

[Wan 15] Yong Wan, Florian Gebert, Fabian Wolf & Piet O. Schmidt. Efficient Sympathetic Motional Ground-State Cooling of a Molecular Ion. Phys. Rev. A, vol. 91, page 043425, 2015.

[Weiss 10] Marc Weiss, Pradipta Shome & Ron Beard. On-Board GPS Clock Monitoring for Signal Integrity. In Proc. 42nd Annual PRRI Meeting, page 465, 2010.

[Wilson 11] A. Wilson, C. Ospelkaus, A. P. VanDevender, J. A. Mlynet, K. R. Brown, D. Leibfried & D. J. Wineland. A 750-mW continuous-wave, solid-state laser source at 313 nm for cooling and manipulating trapped $^9Be^+$ ions. Appl. Phys. B, vol. 105, page 741, 2011.

[Wineland 87] D. J. Wineland, W. Itano, J. Bergquist & R. Hulet. Laser-Cooling Limits and Single-Ion Spectroscopy. Phys. Rev. A, vol. 36, page 2220, 1987.

[Wineland 98] D. J. Wineland, C. Monroe, W. M. Itano, D. Leibfried, B. E. King & D. M. Meekhof. Experiment Issues in Coherent Quantum-State Manipulation of Trapped Atomic Ions. J. Res. Natl. Inst. Stand. Technol., vol. 103, page 259, 1998.

[Wineland 02] D. J. Wineland, J. C. Bergquist, J. J. Bollinger, R. E. Drullinger & W. M. Itano. Quantum computers and atomic clocks. In P. Gill, editeur, Proc. 6th Symp. on frequency Standards and Metrology, page 361, 2002.

[Wolf 09] P. Wolf et al. Quantum Physics Exploring Gravity in the Outer Solar System: The Sagas Project. Exp. Astron., vol. 23, page 651, 2009.

[Wübbena 12] Jannes B. Wübbena, Sana Amairi, Olaf Mandel & Piet O. Schmidt. Sympathetic cooling of mixed-species two-ion crystals for precision spectroscopy. Phys. Rev. A, vol. 85, page 043412, 2012.

[Yamanaka 15] Kazuhiro Yamanaka, Noriaki Ohmae, Ishiro Ushijima, Masao Takamoto & Hidetoshi Katori. Frequency Ratio of ^{199}Hg and ^{87}Sr Optical Clocks beyond the SI Limit. Phys. Rev. Lett., vol. 114, page 230801, 2015.

[Ye 05] Jun Ye & Cundiff T. Steven, editeurs. Femtosecond optical frequency comb: Principle, operation and applications. Springer, 2005.

[Young 99] B. C. Young, F. C. Cruz, W. M. Itano & J. C. Bergquist. Visible lasers with subhertz linewidths. Phys. Rev. Lett., vol. 82, page 3799, 1999.

[Zhang 17] Ping Zhang, Jian Cao, Hua-lin Shu, Jin-bo Yuan, Jun-juan Shang, Kai-feng Cui, Si-jia Chau, Shao-mao Wang, Dao-xin Liu & Xue-ren Huang. Evaluation of blackbody radiation shift with temperature-associated fractional uncertainty at 10^{-18} level for $^{40}Ca^{+}$ ion optical clock. J. Phys. B: At. Mol. Opt. Phys., vol. 50, page 015002, 2017.